ABSTRACT

FAN, XIANG. Adaptive Control of Hysteretic Smart Material Systems. (Under the direction of Dr. Ralph C. Smith).

Smart materials exhibit nonlinear behaviors and hysteresis when driven at field levels necessary to meet stringent performance criteria in high performance applications. This requires models and control designs that effectively compensate for the nonlinear, hysteretic field-coupled material behavior. In this dissertation, we investigate model identification using the homogenized energy model and adaptive control of hysteresis in smart hysteretic system, while the approaches are applicable to control of a wide class of ferroelectric, ferromagnetic and ferroelastic materials, we illustrate the ideas through the example of controlling a ferroelectric actuator.

We pursue the problem of hysteresis control through two complimentary approaches: linear adaptive control using an inverse compensator and nonlinear adaptive control.

Inverse control is a fundamental approach to accommodate hysteresis effect by constructing a right inverse of the hysteresis. Due to the open-loop nature of inverse control, the performance of the inverse compensation is susceptible to model uncertainties and to error introduced by inexact inverse algorithms. The objective of adaptive control is to design a controller that can adjust its behavior to tolerate uncertainties or time-varying parameters. We employ the homogenized energy model to quantify the hysteresis. On the basis of the hysteresis model, we propose an adaptive control framework by combining inverse compensation with adaptive control techniques, and investigate the parameter identification methods for the hysteresis model. We prove the asymptotic tracking property of the proposed adaptive inverse control algorithm, discuss the issue of parameters convergence and illustrate the performance of the proposed control method through simulations.

Adaptive nonlinear control is a more challenging task and has received increasing attention in recent years. The challenge addressed here is how to fuse hysteresis models with available adaptive control techniques to have the basic requirement of stability of the system. In this dissertation, an adaptive variable structure control approach, serving as an illustration, is fused with the homogenized energy model without constructing a hysteresis inverse. The global stability of the system and tracking a desire trajectory to a certain precision are achieved under certain conditions. Simulations are performed on an unstable

nonlinear system. The purpose of exploring new avenues to fuse the model of hysteresis nonlinearities with the available adaptive controller designs without constructing a hysteresis inverse is achieved and illustrated with the promising simulation results. This provides a step toward the development of a general nonlinear adaptive control framework for hysteretic systems.

Adaptive Control of Hysteretic Smart Material Systems

by

Xiang Fan

A dissertation submitted to the Graduate Faculty of
North Carolina State University
in partial fullfillment of the
requirements for the Degree of
Doctor of Philosophy

Applied Mathematics

Raleigh, North Carolina

2009

APPROVED BY:

Dr. Hien Tran	Dr. Mansoor Haider
Dr. Ralph Smith Chair of Advisory Committee	Dr. Kazufumi Ito

DEDICATION

To my adorable Mom and Dad for their unfailing love and support.

BIOGRAPHY

Xiang Fan graduated from Wuhan University, China with bachelor of Computer Science in 2003. Then she attended North Carolina State University and received a master of science degree in applied mathematics in 2006 and a doctorate degree in 2009.

"What then shall we choose? Weight or lightness?" – Milan Kundera

ACKNOWLEDGMENTS

This dissertation is a report of the research work that has been done since I started my studies at the North Carolina State University in 2004. During this time I have worked with a number of people whose contribution made this work possible. It is a great pleasure to convey my gratitude at the beginning of this report.

It has been my great privilege and experience to have Professor Ralph Smith as my advisor. I am grateful to him for his instructions, guidance, and support. He led me into the area of hysteresis modeling and control and inspired me with his vision and expertise during the course of my PhD study. Apart from providing technical directions, he has also offered me with invaluable advices on how to improve myself as a researcher and suggestions on my job search.

I would like to thank Professor Kazufumi Ito, Professor Hien Tran, Professor Mansoor Haider for kindly joining the advisory committee and providing constructive advice, guidance and comments.

I also want to thank the graduate administrative staff of Math Department for their assistance during my study and life here, special thanks are due to Denise Seabrooks, Lesa Denning and Carolyn Gunton.

I gratefully acknowledge the Air Force Office of Scientific Research for providing the financial support of my studies and research through the Grant No. AFOSR-FA9550-04-1-0203 and AFOSR-FA9550-08-1-0348.

Last, but certainly not the least, I gratefully acknowledge my dearly-loved family for all they have done for me and thank them for supporting me in my studies in US.

TABLE OF CONTENTS

LIST OF TABLES

LIST OF FIGURES

Chapter 1

Introduction

A growing emphasis in advanced control systems design focuses on the use of multi-functional materials, such as piezoceramics, magnetostrictives, and shape memory alloys, in integrated transducers to improve control authority and performance, reduce weight, and minimize power requirements. For example, piezoceramic compounds have both actuator and sensor capabilities due to the direct and converse piezoelectric effects, microscale set point accuracy, and high frequency (kHz) operating capabilities. This has led to their use in applications ranging from nano-positioning mechanisms in an atomic force microscope (AFM) [37] to inertial sensors in an accelerometer. Magnetostrictive materials also offer both actuator and sensor capabilities as well as broadband transduction and large output forces. Recent applications and products exploiting these properties include high accuracy, high speed milling devices [40] and torque sensing for steering systems [39]. Shape memory alloys operate at lower frequencies ($<$ 100 Hz for bulk materials) but offer the largest power densities of the three compounds. Hence they are being considered for applications ranging from vibration dissipation in buildings and flexible aerospace structures to active shape configuration of an airfoil to optimize flight characteristics while minimizing drag [39, 44].

Although smart materials have been successfully implemented in a number of applications, limitations associated with nonlinear and hysteretic behavior have presented challenges in developing high performance actuation responses over a broad frequency range. In ferroelectric and ferromagnetic materials, the nonlinear and hysteretic behavior is primarily due to the reorientation of local electric or magnetic variants that align with the applied electric or magnetic fields. Moderate to large field levels can induce 0.1% strain

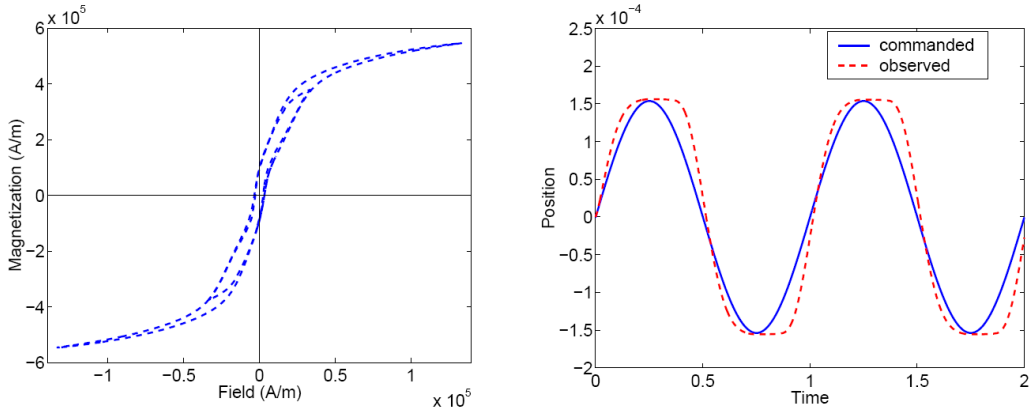

(a) (b)

Figure 1.1: (a) Inherent hysteresis behavior, and (b) phase delay caused by hysteresis in Terfenol-D.

in PZT and up to 6% strain in shape memory alloys. At these fields levels, if hysteresis is not accommodated, it can induce a phase delay in the response of the actuator, which significantly complicates control design. This phenomena is illustrated in Figure 1.1(b) for an open-loop simulation of a Terfenol-D transducer.

This has motivated research in developing new control designs that can effectively compensate for nonlinearities and hysteresis induced by ferroelectric or ferromagnetic switching while still providing accurate forces or displacement over a broad frequency range.

Two general strategies are typically considered when designing control laws for hysteretic actuators. One strategy is to employ the models to construct inverse representations or compensators that can be employed as filters before the hysteretic actuator, as illustrated in Figure 1.2. The other one is to employ nonlinear constitutive models to construct nonlinear control designs that accommodate the hysteresis and constitutive nonlinearities.

Both of the approaches are discussed in this dissertation. We focus first on the incorporation of a model-based inverse compensator directly into the control design, as shown in Figure 1.2(a). The key to constructing an inverse compensator that accommodates hysteretic behavior is the development of material models that can be efficiently inverted. We note that model-based control designs for hysteretic systems have received considerable attention in areas relating to adaptive, classical and optimal control. These models typi-

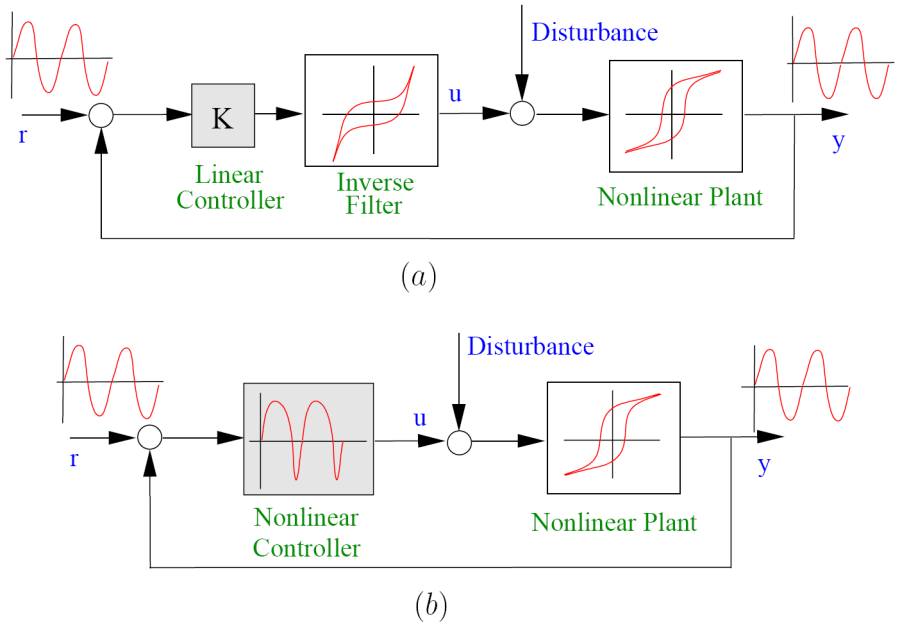

Figure 1.2: (a) Linear control design employing an inverse filter, and (b) nonlinear control design.

cally accommodate hysteretic material behavior by implementing Preisach operators [53] or domain wall models [18]. Although Preisach models can reasonably predict nonlinear, hysteretic material behavior observed in smart materials such as piezoelectric, magnetostrictive and shape memory alloys, a significant number of non-physical parameters are necessary to model minor loop hysteresis. Domain wall models avoid this issue by incorporating energy principles at the domain length scale to predict macroscopic material behavior, but extensive modifications are required to guarantee closure of minor loops. Our work employs the homogenized energy model due to its energy basis and flexibility with regard to numerous operating conditions. As detailed in [3], it has been demonstrated that its corresponding inversion can be achieved at reasonable accuracy and speed. For the nonlinear adaptive control approach depicted in Figure 1.2(b), the challenge is how to fuse the hysteresis model with the available control techniques to achieve at least the basic stability requirement for the concerned system. As an illustration, we propose an adaptive variable structure [51, 61] to mitigate the effects of the hysteresis without using the inverse of homogenized energy model.

1.1 Contributions of the Dissertation

1.1.1 Control of hysteresis based on the homogenized energy model

The emphasis in this dissertation focuses on the incorporation of physics through energy-based techniques to provide control designs capable of achieving stringent tracking and speed criteria.

- Model-based linear control designs

  We focus on the development of model-based control designs having the capability for real-time implementation at the speeds dictated by eventual applications. We rely on the model reference adaptive control (MRAC) technique [10, 23] and $\mathcal{L}_1$ control theory [7, 8] to provide starting points from which to initiate adaptive control designs that incorporate the physical mechanisms which produce hysteresis through inverse compensators.

- Nonlinear adaptive control design

  We introduce a new nonlinear adaptive control structure to mitigate the effect of hysteresis behavior. The related results presented in this dissertation can serve as an initial step to the further investigation.

1.1.2 Adaptive Identification of material parameters in the inversion of homogenized energy model

The model, which describe the nonlinearities and hysteresis for the smart materials, contains several material-dependent parameters that must be identified in order to effectively utilize resulting inverse compensators. Additionally, material parameters in the models may slowly vary as a result of changes in the operating conditions such as temperature or creep. It is desired to identify or update the material parameters during the operation of the transducer as opposed to applying off-line parameter estimation algorithms such as least square fits to data. We propose a method capable of adaptively estimating nonlinearly occurring parameters in the hysteresis inverse model. This method ensures that the inverse compensators based on the hysteresis model continue to provide adequate attenuation of the hysteresis behaviors in the smart systems.

1.2 Organization of the Dissertation

In Chapter 2, we provide an introduction to the homogenized energy model, and summarize inversion schemes for the homogenized energy operator. The dynamic hysteresis model is studied in Chapter 3. In Chapter 4 and 5, we discuss two adaptive inverse control frameworks for smart hysteretic systems: modified MRAC and $\mathcal{L}_1$ adaptive control. Simulation results are summarized. Chapter 6 describes an adaptive parameter estimation algorithm capable of identifying nonlinearly occurring material parameters in the inversion of the homogenized energy model. In Chapter 7 we propose an adaptive nonlinear control structure, which is an initial step to a more general nonlinear control framework using the homogenized energy model. Conclusions are provided in Chapter 8.

Chapter 2

Identification and Approximate Inversion of the Homogenized Energy Model

In this chapter, we summarize aspects of the homogenized energy model and we discuss the identification of the hysteresis parameters. Finally we summarize the inversion of the homogenized energy model.

2.1 Homogenized Energy Model

In this section, we introduce the homogenized energy operator and some of its properties [4, 39, 40, 41, 42, 45, 47]. The homogenized energy model is based on an energy description at the mesoscopic length scale. This local energy formulation is used to predict macroscopic behavior using a stochastic representation of material inhomogeneities. Our work in this dissertation employs the homogenized energy model due to its energy basis and flexibility with regard to numerous operating conditions. Compared with Preisach model [53] and domain wall model [18], a major benefit of the homogenized energy model is the incorporation of various rate and temperature-dependences. The Preisach models and the domain wall models are derived under the assumptions that thermal relaxation mechanisms are negligible and hysteresis properties are rate-independent. For many operating regimes, these assumptions are reasonable and the models provide reasonable accuracy. In other

cases, the after-effect and accommodation (reptation) phenomena cause nonclosure of minor loops thus negating the deletion properties. Another benefit of this model is its ability to predict biased minor loops efficiently and accurately. Although Preisach models can also reasonably achieve minor loop, a significant number of non-physical parameters can be necessary to achieve material characterizations. Domain wall models avoid this issue by incorporating energy principles at the domain length scale to predict macroscopic material behavior, but modifications are required to guarantee closure of minor loops.

Since we will be applying feedback control methods to the smart transducers, we often have no a *priori* knowledge of the signal to be input into the transducers. Therefore, it is advantageous to be able to model biased inner loops accurately. While the domain wall model can predict symmetric inner loops, it does not guarantee minor loop closure without a *priori* knowledge of input field. While Preisach model provide the capability for accurately quantifying minor loop behavior, this accuracy typically comes at the price of increased computational complexity.

As mentioned previously, the homogenized energy model is based on the quantification of energy required to reorient dipoles or moments in combination with stochastic homogenization techniques to accommodate variations in coercive and interaction fields. While analogous models exist for ferroelastic and ferromagnetic materials, the model will be summarized in the context of ferroelectric materials.

2.1.1 Local Constitutive Relations

We consider s Helmholtz relation that incorporates the internal energy due to the interaction of electric dipoles. The model assumes that dipoles have two preferred orientations, namely in the direction of the stress-induced easy axis and against it. Therefore, a double well potential can be employed to approximate the Helmholtz free energy. Statistical mechanics analysis [39, 45] indicates that a first-order approximation to the potential behaves quadratically in the neighborhood of the three equilibria. Therefore, we can formulate

the Helmholtz energy as

$$\psi(P) = \begin{cases} \eta(P + P_R)^2/2, & P \leq -P_I \\ \dfrac{\eta}{2}(P_I - P_R)\left(\dfrac{P^2}{P_I} - P_R\right), & |P| < P_I \\ \eta(P - P_R)^2/2, & P \geq P_I. \end{cases} \tag{2.1}$$

As depicted in Figure 2.1, P_R and P_I respectively denote the point at which the minimum of ϕ occurs and the inflection point.

For an applied electric field E, the Landau energy is given by

$$G(E, P) = \psi(P) - EP. \tag{2.2}$$

The Landau free energy balances the internal Helmholtz energy with the electrostatic energy; i.e., work performed by the applied external field E. As detailed in [39], where the Legendre transform properties of the Landau energy are discussed, G is a function the independent variable E and the dependent variable P.

For regimes in which thermal relaxation is negligible, direct minimization of (2.1) via the relation $\frac{\partial G}{\partial P} = 0$ yields the kernel

$$\overline{P}(E; x_+) = \frac{1}{\eta}(E) + 2P_R x_+ - P_R \tag{2.3}$$

where $x_+ = 1$ for positively oriented dipoles and $x_+ = 0$ for negatively oriented dipoles.

Thermal activation is manifested by dipoles having sufficient thermal energy to switch states before a minima of the Landau energy is eliminated. To quantify this, the Landau energy is balanced with the relative thermal energy through Boltzmann's relation

$$\mu(G) = C \exp\left(-\frac{GV}{kT}\right) \tag{2.4}$$

where V is the mesoscopic volume being modeled, k is Boltzmann's constant, T is the material temperature in degree Kelvin, and C is a constant chosen to ensure integration to unity. The local average polarization [39, 41, 47] is then given by

$$\overline{P} = x_+ \langle P_+ \rangle + x_- \langle P_- \rangle \tag{2.5}$$

where $\langle P_+ \rangle$ and $\langle P_- \rangle$ denote the expected values of the polarization for dipoles having positive and negative orientations, respectively. We can quantify $\langle P_+ \rangle$ and $\langle P_- \rangle$ by

$$\langle P_+ \rangle = \frac{\int_{P_0}^{\infty} P \exp\left(\frac{-G(E,P)V}{kT}\right) dP}{\int_{P_0}^{\infty} \exp\left(\frac{-G(E,P)V}{kT}\right) dP}, \qquad \langle P_- \rangle = \frac{\int_{-P_0}^{-\infty} P \exp\left(\frac{-G(E,P)V}{kT}\right) dP}{\int_{-P_0}^{-\infty} \exp\left(\frac{-G(E,P)V}{kT}\right) dP}. \tag{2.6}$$

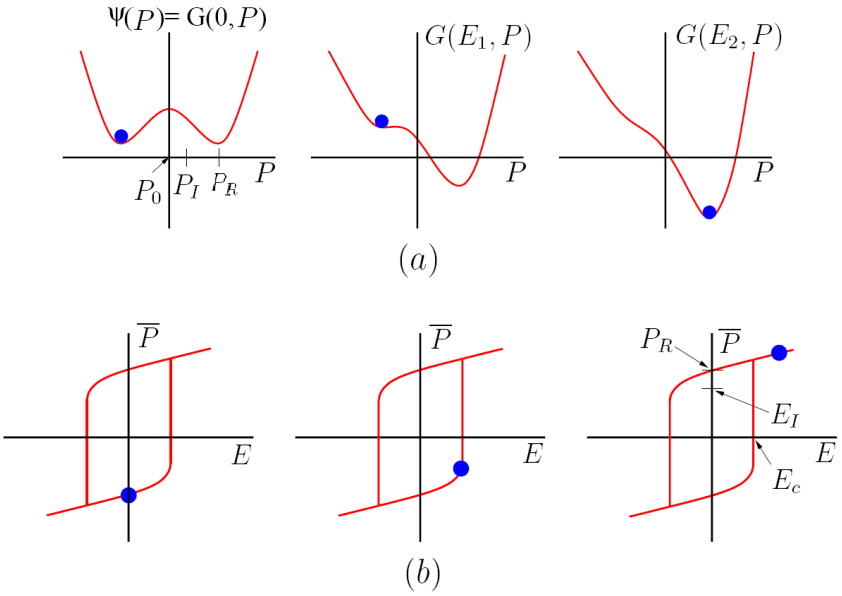

Figure 2.1: (a) Landau energy G, and (b) the corresponding local polarization $\overline{P}$ for increasing field E.

Here, P_0 denotes the unstable equilibrium (see Figure 2.1). For implementation, P_I can replace P_0. This simplifies the approximation of the integrals and is reasonable since the maximum restoring force occurs at P_I and $-P_I$. And also if the thermal activation is reduced to zero, the interaction points and unstable equilibria coincide (see [45]).

The dipole fractions satisfy the evolution equations

$$\dot{x}_+ = -p_{+-}x_+ + p_{-+}x_-, \qquad x_- = 1 - x_+ \tag{2.7}$$

where p_{+-} and p_{-+} are the likelihoods of switching from positive to negative orientation and switching from negative to positive orientation, respectively. They are given by

$$p_{+-} = \sqrt{\frac{kT}{2\pi m}} \frac{\exp\left(\frac{-G(E,P_0)V}{kT}\right)}{\int_{P_0}^{\infty} \exp\left(\frac{-G(E,P)}{kT}\right) dP}, \qquad p_{-+} = \sqrt{\frac{kT}{2\pi m}} \frac{\exp\left(\frac{-G(E,-P_0)V}{kT}\right)}{\int_{P_0}^{\infty} \exp\left(\frac{-G(E,P)}{kT}\right) dP} \tag{2.8}$$

where m is the mass of the lattice volume V. The relation between the applied field E and the polarization P exhibits both hysteresis and nonlinear transition because the local polarization (2.5) is probabilistic. The steepness of the transition depends on the ratio of GV to kT. It is also shown in [39] and [47] that the kernel $\overline{P}$ given by (2.5) converges to (2.3) in the limit $kT/V \to 0$ of negligible thermal activation.

2.1.2 Global Constitutive Relations

To incorporate the effects of material inhomogeneities, microcrystallinity, and variable effective field $E_e = E + E_I$, we assume that the interaction field E_I, due to neighboring dipoles and certain electromechanical interactions [2], and local coercive field E_c are manifestations of underlying distributions rather than constants. If we designate the associated densities by $\nu_c(E_c)$ and $\nu_I(E_I)$, the macroscopic polarization is quantified by the relation

$$[P(E)](t) = \int_0^\infty \int_{-\infty}^\infty \nu_c(E_c)\nu_I(E_I)\overline{P}\left(E(t) + E_I; E_c, x_+\right) dE_I dE_c \tag{2.9}$$

where $\nu_c(E_c)$, $\nu_I(E_I)$ respectively denote the densities of coercive field E_c and interaction field E_I. The densities are constrained by the physical relations:

1. both ν_c and ν_I are bounded by decaying exponentials,
2. ν_c is strictly positive,
3. ν_I is symmetric about 0, and
4. $\int_0^\infty \nu_c(E_c)dE_c = 1,\ \int_{-\infty}^\infty \nu_I(E_I)dE_c = 1.$

The model is sufficiently simple to allow the possibility of real time implementation and has a relatively low number of material dependent parameters. The parameters for the PZT sample are given in Table 2.1.

For computational purposes, the integrals in (2.9) are solved numerically with quadrature relations; i.e.,

$$[P(E)](t) \approx \sum_{i=1}^{N_c}\sum_{j=1}^{N_I} \nu_c(E_{c_i})\nu_I(E_{I_j})\overline{P}\left(E(t) + E_{I_j}; E_{c_i}; x_+^{ij}\right) w_{c_i} w_{I_j} \tag{2.10}$$

where w_c and w_I give the quadrature weights. The model for ferromagnetic compounds is equivalent [39].

Table 2.1: Parameters for PZT4.

$E = 1800V$			
P_R	$0.045\,C/m^2$	c	$0.3018\,V^2/m^2$
$\overline{E}_c$	$1.05 \times 10^5\,V/m$	b	$2.1924 \times 10^{11}\,V^2/m^2$
η	4.0×10^8	C	6.8287×10^{-12}

2.2 Parameter Estimation

2.2.1 Lognormal and Normal Densities

One choice for the coercive and interaction field densities are the lognormal or normal relations

$$\begin{aligned} \nu_c(E_c) &= c_1 e^{-\left[\ln(E_c/\overline{E}_c)/2c\right]^2}, \\ \nu_I(E_I) &= c_2 e^{-E_I^2/2b^2}. \end{aligned} \tag{2.11}$$

In this case, the parameters to be estimated are

$$\mathbf{q} = [P_R,\, \eta,\, \overline{E}_c,\, c,\, b,\, C]^T, \quad \text{where } C = c_1 \cdot c_2\,. \tag{2.12}$$

The material parameters (2.12) for PZT4 are given in Table 2.1. These parameters were estimated through a least squares fit to high drive level data in [47].

2.2.2 General Densities

Performing parameter estimation with lognormal coercive and normal interaction field densities is fast and the fits to data are smooth. However, when more accurate model predictions are critical, a general density can be fit to data. Some techniques for identifying the densities ν_c and ν_I are illustrated in [14, 15, 43]. If we use a general density approximation in which we estimate all of the quadrature values in Equation (2.10), then

$$\mathbf{q} = [P_R,\, \eta,\, \{\nu_c(E_{c_i})\},\, \{\nu_I(E_{I_j})\}]^T. \tag{2.13}$$

In this case, the parameter algorithms perform better (lower least-square residual), as shown in Figure 2.2 [14], but may take significantly longer runtimes. For example, in the case of

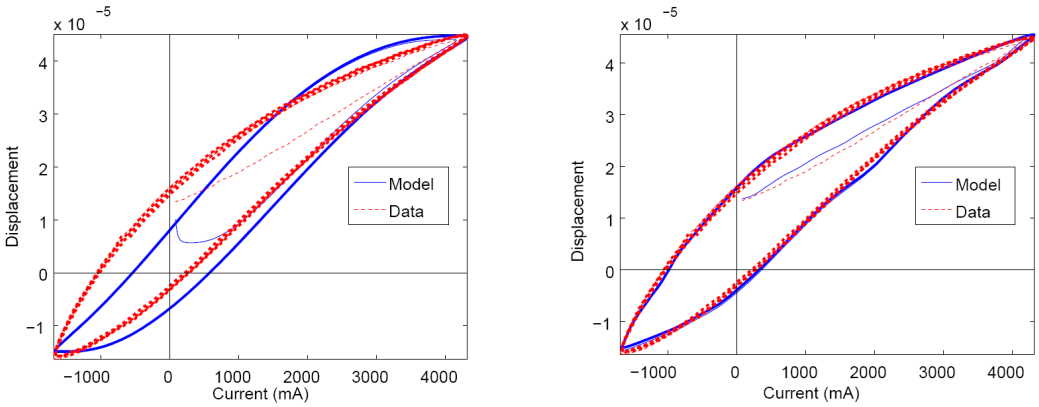

Figure 2.2: Fit to data with 100 Hz current input using (a) lognormally distributed coercive and normally distributed interaction field densities (b) generally distributed densities [14].

4-point Gaussian quadrature, the dimension of $\mathbf{q}$ is $2+6N$ for N quadrature intervals. For large N, the dimension of the parameter space is quite large resulting in long estimation runtime. Moreover, the general densities are often not smooth and may be multi-modal or even non-decaying which are both non-physical attributes.

Galerkin Expansion Density Representations

In comparison to general density formulation [43], the Galerkin expansion formulations of densities shown in [14] and [15] exhibits decreased parameter estimation runtime and increased smoothness in the fit of the data.

We employ Galerkin expansions of the form

$$\nu_c(E_c) = \sum_{i=0}^{n} \alpha_i \phi_i(E_c) \quad \text{and} \quad \nu_I(E_I) = \sum_{j=0}^{m} \beta_j \phi_j(E_I) \tag{2.14}$$

where ϕ_i and ϕ_j are basis functions and α_i, β_j are the coefficients to be identified.

One basis choice is the piecewise continuous cubic B-spline functions, as defined in [39]. The result of the use of cubic spline is increased smoothness of the densities which translates directly to a smoother fit [14], but the resultant densities can be nonphysical and corresponding constraint were incorporated into the numerical optimization to generate expected density behavior.

Another choice is the lognormal basis elements

$$\phi_i(E_c) = \frac{1}{\sqrt{2\pi} E_c \, \sigma_c^i} e^{-[\ln(E_c)-\mu_c^i]^2/2(\sigma_c^i)^2} \quad \text{and} \quad \phi_j(E_I) = \frac{1}{\sqrt{2\pi}\sigma_I^j} e^{-E_I^2/2(\sigma_I^j)^2} \tag{2.15}$$

as defined in [15]. Here the standard deviation of each coercive density basis ϕ_i is varied according to

$$\sigma_c^i = \sigma_c - v\sigma_c + \left(\frac{2\sigma_c\, v}{N_i}\right) i \qquad \text{for } i = 0 \cdots N_\sigma \tag{2.16}$$

for N_σ standard deviations. The mean values μ_c^i may also be altered in a similar fashion to that of the σ_c^i. Standard deviations of each interaction density basis are created in a manner similar to (2.16). These basis elements have physical interpretations and do not require constraints on the densities for decay. The only requirement imposed is the positivity of the expansion coefficients α_i and β_j.

In this case, the parameter estimation problem can be formulated as a bounded optimization problem [15], and the parameters to be estimated are

$$\mathbf{q} = [P_R,\, \eta,\, \{\alpha_i\},\, \{\beta_j\}]^T \tag{2.17}$$

for the negligible relaxation model and

$$\mathbf{q} = \left[P_R,\, \eta,\, \tau(T),\, \{\alpha_i\},\, \{\beta_j\}\right]^T, \quad \tau(T) = \sqrt{\frac{2\pi m}{kT}} \tag{2.18}$$

when thermal relaxation is included. This reduces the size of $\mathbf{q}$ to approximately $2{+}3N/2$ for N composite quadrature intervals. The optimized thermal relaxation homogenized energy model fits are shown with physical data collected from a PZT sample in Figure 2.3 [15].

2.3 Inverse Hysteresis Model

The general structure of models for smart actuators that quantify both hysteresis and dynamic behavior is shown in Figure 2.4 [57]. In the figure, $P(s)$ represents the transfer function of the linear part in the actuator, while $\mathcal{H}(s)$ denotes a hysteretic nonlinearity.

As mentioned in the Introduction, a basic idea for controller synthesis for such systems is to design a right inverse compensator $\widehat{\mathcal{H}}^{-1}$ for $\mathcal{H}$ as shown in Figure 2.5. The controller design problem is then reduced to designing a linear controller $K(s)$ for the system $P(s)$.

In the context of this dissertation, we consider $\mathcal{H}$ to be the homogenized energy operator. A definition of the inverse homogenized energy model is the following: given any valid state x_+ and any specified $\widehat{P}$ within the operating range of the material, determine

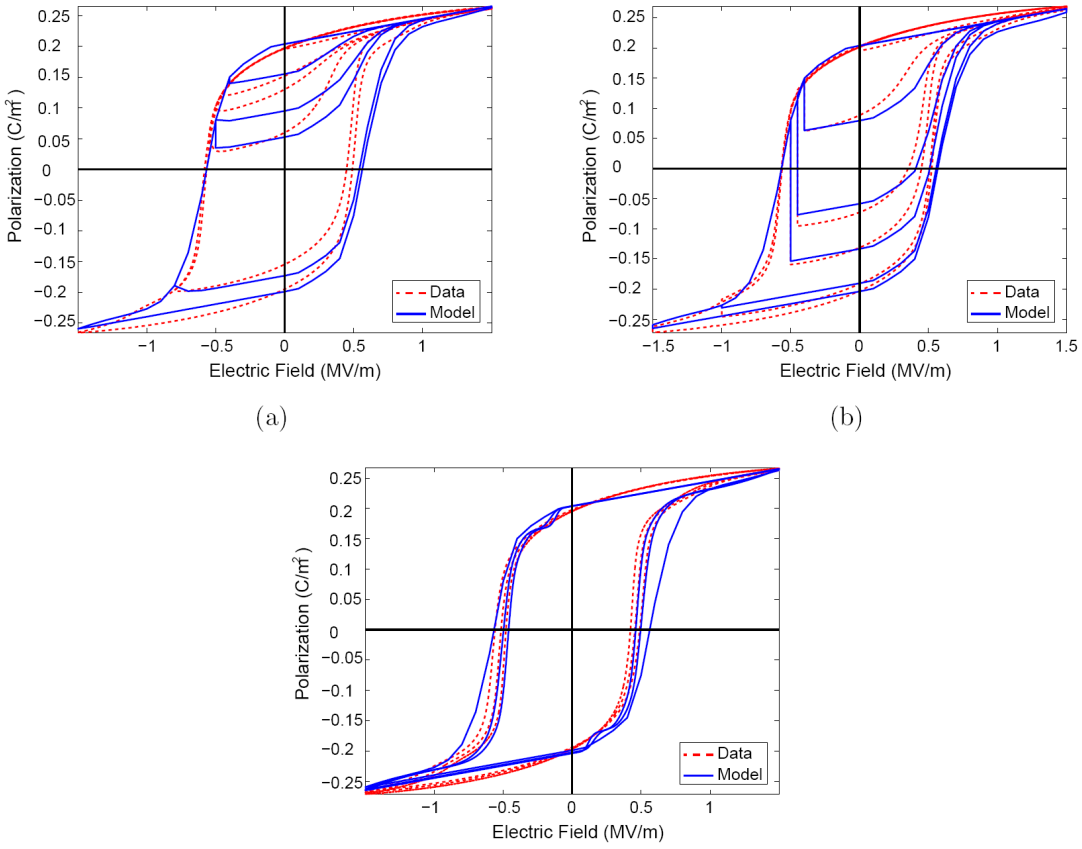

Figure 2.3: Homogenized energy model fits to PZT (a) minor loop, (b) creep, and (c) major loop data from [36].

the field level E such that $P = \widehat{P}$. The homogenized energy operator is highly nonlinear, and, in general, we cannot find a closed-form formula for the inverse compensator unless the density functions are of some special form. Thus to construct the inverse compensator, the problem is reformulated as a numerical root finding problem, namely determining the value E such that for a given x_+ and $\widehat{P}$,

$$P(E; x_+) - \widehat{P} = 0. \tag{2.19}$$

To determine the electric field E required to achieve a desired polarization $\widehat{P}$, the monotonicity of the hysteresis model is exploited and the hysteresis model is advanced until the desired polarization is surpassed. Then the electric field is computed by a linear interpolation between the last two points. The computational speed of the inverse compensator

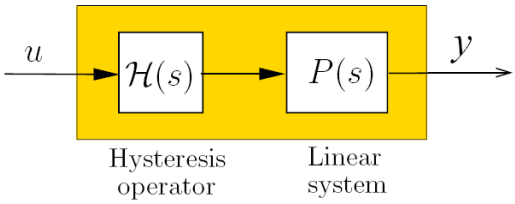

Figure 2.4: Structure of models for smart actuators

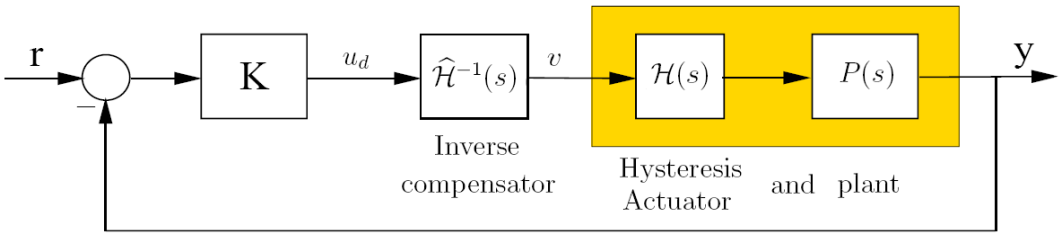

Figure 2.5: A generic approach to controlling a system with hysteresis. First, an inverse operator is constructed to approximately cancel the hysteresis nonlinearity. The feedback controller K is then designed to accommodate the linear dynamics P(s) and the inversion error.

depends on the size of the step taken in advancing the hysteresis model. Larger steps will increase the speed while decreasing the accuracy of the inverse compensator. To facilitate real time control, a larger step size is desired, therefore the control method must be designed to reject significant amount of error in linearization of the hysteresis [52, 53].

2.4 Concluding Remarks

This chapter summarized the homogenized energy model used to quantify the hysteretic behavior exhibited by ferroelectric materials as well as the inverse compensator for the model. This model quantifies the energy required to reorient the electric dipoles in ferroelectric materials and then utilizes stochastic homogenization techniques to accommodate variation in coercive and effective fields. Employing quadrature approximations, the model can be implemented algebraically and from this implementation algorithm an inverse compensator can be developed. Although the model summarized here quantifies the inherent hysteresis in ferroelectric compounds, all of the modeling techniques can be applied to several smart material including ferromagnetic and, under certain conditions, shape memory alloys.

Chapter 3

A Dynamic Model For Ferroelectric Actuators

To provide a motivating example, we consider a piezoelectric nanopositioning stage as illustrated in Figure 3.1.

The side view illustrates the nanopositioning stage and piezoelectric actuator that controls the sample height relative to the cantilever. In this mode of operation, the cantilever position is defined by using a photodiode to measure changes in a reflected laser beam and a feedback law is used to reposition the sample to maintain constant stresses. A 2-D scan in this manner yields the surface topography of the sample. A top view of the positioning stage is illustrated in Figure 3.1(b) where two additional piezoelectric stack actuators are used to control in-plane displacement. In this design, in-plane actuator coupling is typically negligible which allows development of the control design for a single z-direction actuator. Nanopositioning stages may also utilize piezoelectric tube actuators to control in-plane and out-of-plane displacement. This design uses segmented electrodes where the application of an electric field forces the tube to bend thus creating lateral displacement. This design has been shown to provide improved linear behavior but the non-negligible coupling between in-plane displacements further complicates the control design [46]. The decoupled stack actuator nanopositioner design is considered here to focus on control development.

In the previous chapter, a model for the relationship between the applied field E and the polarization P in a ferroelectric material was described. However, the displacements generated by the stack actuator must be quantified for implementation within the control

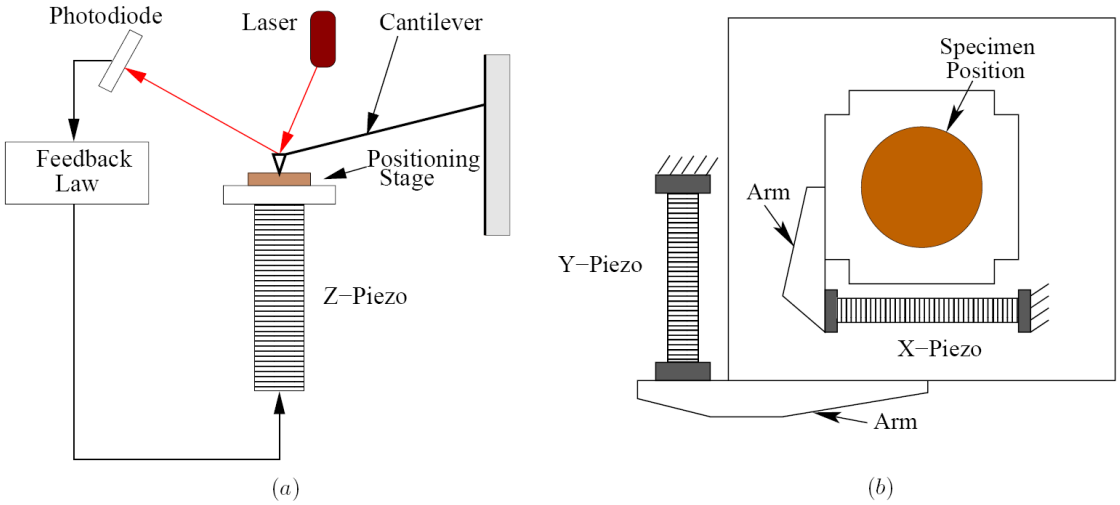

Figure 3.1: Schematic of an atomic force microscope: (a) side view of the AFM set-up with z-control piezoelectric actuator; (b) top view of the positioning stage illustrating the configuration of the x-y control piezoelectric actuators.

design. As detailed in [39], this is provided by the incorporation of the electroelastic coupling in the Helmholtz energy relation

$$\psi(P,\epsilon) = \psi(P) + \frac{1}{2}Y^P\epsilon^2 - h_1\epsilon(P - P^\tau) - h_2\epsilon(P - P^\tau)^2$$

and the corresponding Landau energy relation

$$G(E,P,\epsilon) = \psi(P,\epsilon) - EP - \sigma\epsilon \tag{3.1}$$

where Y^P is the elastic modulus at constant polarization, ϵ is the linear strain component in the direction of loading, h_1 is the piezoelectric coefficient and h_2 is the electrostrictive coefficient. The polarization P is computed using equation (2.9) where P^τ is the initial macroscopic remanent state of the material. In all simulations presented here, the actuator is initially poled with a field equal to $2\overline{E}_c$ which results in $P^\tau = 0.206C/m^2$.

To obtain an elastic constitutive relation, the equilibrium condition $\frac{\partial G}{\partial \epsilon} = 0$ is invoked to obtain the stress relation

$$\sigma = Y^P\epsilon - h_1(P(E) - P^\tau) - h_2(P(E) - P^\tau)^2. \tag{3.2}$$

It is assumed that stress fields are limited to the linear elastic regime, which means that relationship (3.2) quantifies the linear relationship between stresses σ and strains ϵ of the

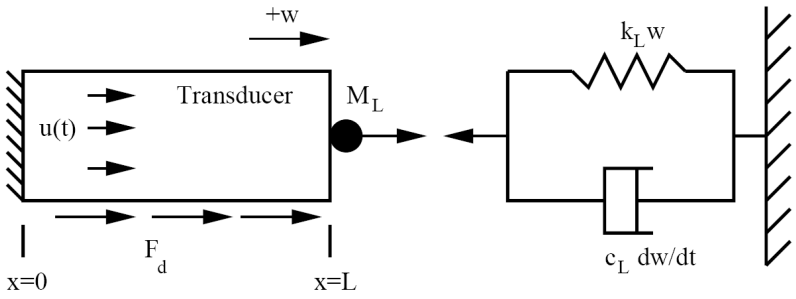

Figure 3.2: Piezoelectric stack actuator with damped oscillator used to quantify loads during scanning operations of an AFM nanopositioning stage. Disturbance forces along the actuator are denoted by F_d and the control input is $u(t)$.

piezoelectric actuator as well as the nonlinear hysteretic dependence of the stress on applied fields E through the polarization P.

The direct use of the constitutive relation (3.2) will yield an undamped model for the piezoelectric stacked actuator. We assume that stress is proportional to strain and strain rate to incorporate Kelvin-Voigt damping. Thus, the stress at any point of the stacked actuator is given by

$$\sigma = Y^P \epsilon + c_D \dot{\epsilon} - h_1(P(E) - P^\tau) - h_2(P(E) - P^\tau)^2 \tag{3.3}$$

where c_D is the Kevin-Voigt damping coefficient.

3.1 Rod Model for the Stacked Actuator

The constitutive relation (3.3) quantifies the electromechanical behavior of piezoceramic material operating below the coercive stress σ_c where ferroelectric switching commences. To facilitate the control design, the constitutive relations given by (2.9) and (3.3) are used to develop a system model that quantifies forces and displacements when a electric field or stress is applied to the piezoelectric stack actuator used in the nanopositioning stage. The partial differential equation model is first given and then formulated as set of ordinary differential equations through a finite element discretization in space. The structural coupling of the nanopositioning stage is modeled as a damped oscillator to account for boundary conditions at the end of the piezoelectric actuator. The geometry used in constructing the structural model is illustrated in Figure 3.2.

One end of the piezoelectric actuator ($x = 0$) is assumed to be fixed while the other end ($x = L$) is constrained by a damped oscillator and has a point mass attached, as depicted in Figure 3.2. The Kelvin-Voigt damping coefficient, density and point mass are respectively denoted by c_D, ρ and M_L.

The damping spring has stiffness k_L and damping coefficient c_L. A balance of forces for the structural model is given by the relation [39, 43]

$$\rho A \frac{\partial^2 w}{\partial t^2} = \frac{\partial N_{tot}}{\partial x} \tag{3.4}$$

where A is the cross-section area of the piezoelectric actuator and the w is the displacement. The total force N_{tot} acting on the actuator is

$$N_{tot}(t,x) = Y^P A \frac{\partial w}{\partial x} + c_D A \frac{\partial^2 w}{\partial x \partial t} + F_p(E) + F_d \tag{3.5}$$

the elastic force is given by the first term on the right hand side of (3.5) and Kelvin-Voigt damping is incorporated in the second term. The linear elastic strain component in the direction of loading is defined by $\epsilon = \frac{\partial w}{\partial x}$. The term F_d incorporates external disturbance loads and the coupling force F_p represents forces generated by an applied electric field where

$$F_p(E) = A\left[h_1(P(E) - P^\tau) + h_2(P(E) - P^\tau)^2\right] \tag{3.6}$$

and the hysteretic and nonlinear $E - P$ relation is specified by Equation (2.9).

As illustrated in Figure 3.2, the boundary condition are defined by a zero displacement at $x = 0$ and the balance of forces at $x = L$ yields

$$N_{tot}(t,L) = -k_L w(t,L) - c_L \frac{\partial w}{\partial t}(t,L) - m_L \frac{\partial^2 w}{\partial t^2}(t,L). \tag{3.7}$$

The initial boundary conditions are $w(t,0) = 0$ and $\frac{\partial w}{\partial x}(0,x) = 0$. Model parameters associated with the stack actuator and damped oscillator used in the control design are given in Table (3.1) [45].

The strong form of the PDE model given by Equation (3.1) can be written in a variational form for finite element implementation. Multiplication by weight functions and integration by parts yields

$$\begin{aligned} \int_0^L \rho A \frac{\partial^2 w}{\partial t^2}\phi \, dx &= -\int_0^L \left[Y^P A \frac{\partial w}{\partial x} + c_D A \frac{\partial^2 w}{\partial x \partial t} + F_p(E) + F_d \right] \frac{\partial \phi}{\partial x} dx \\ &\quad - \left[k_L w(t,L) + c_L \frac{\partial w}{\partial t}(t,L) + m_L \frac{\partial^2 w}{\partial t^2(t,L)} \right] \phi(L) \end{aligned} \tag{3.8}$$

Table 3.1: Model parameters associated with the piezoelectric stacked actuator [45].

$Y^P = 60 \times 10^9\, N/m^2$	$\rho = 7.5 \times 10^3\, kg/m^3$	$k_L = 3.04 \times 10^6\, N/m$
$h_1 = 1.0 \times 10^6\, N/C$	$A = 5.07 \times 10^{-}4\, m^2$	$c_L = 3.04 \times 10^2\, Ns/m$
$h_2 = 1.0 \times 10^3\, Nm^2/C^2$	$c_D = 3.7 \times 10^6\, Ns/m$	$m_L = 40\, g$
$P_R = 0.3\, C/m^2$	$L = 0.1\, m$	

where the space of test functions is $H_0^1(0, L) = \{\phi \in H^1(0, L) \,|\, \phi(0) = 0\}$. For simulation and control implementation, it is necessary to discretize the infinite dimension model (3.8) in a manner similar to that described in [9, 39].

3.1.1 Finite Element Method

The piezoelectric stack actuator model given by Equation (3.8) is discretized in space followed by a finite-difference approximation. The transducer is divided into N equal segments over the length [0, L] with points $x_i = ih$, $i = 0, 1, \cdots, N$ and step size $h = L/N$. The spatial basis $\phi_{i=1}^N$ is comprised of the linear basis functions

$$\phi_i(x) = \frac{1}{h} \begin{cases} (x - x_{i-1}), & x_{i-1} \le x < x_i \\ (x_{i+1} - x), & x_i \le x < x_{i+1} \\ 0, & \text{otherwise} \end{cases} \tag{3.9}$$

for $i = 1, \cdots, N-1$. For $i = N$, the basis function is defined to be

$$\phi_N(x) = \frac{1}{h} \begin{cases} (x - x_{N-1}), & x_{N-1} \le x < x_N \\ 0, & \text{otherwise.} \end{cases} \tag{3.10}$$

Figure 3.3 depicts the basis elements (see [32, 39] for details).

The approximate solution to Equation (3.8) is given by a linear superposition of the basis functions

$$w^N(t, x) = \sum_{i=1}^{N} w_i(t)\phi_i(x) \tag{3.11}$$

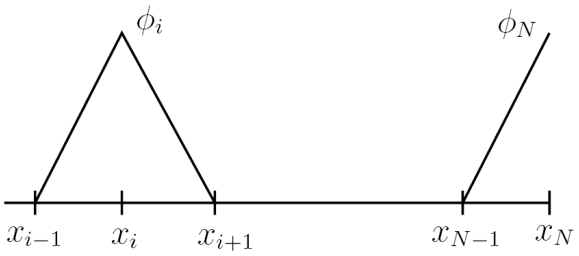

Figure 3.3: Basis functions.

where $w_i(t)$ are the nodal displacement solutions along the length of the transducer. Note that (3.11) satisfies $w^N(t,0) = 0$ and, since $H^N = \text{span}\ \phi_{i=1}^N \in H_0^1(0,L)$, then arbitrary displacements at $x = L$ can be attained.

By substituting $w^N(t,x)$ into Equation (3.9), with the basis functions employed as the weight functions, a second order matrix equation

$$\mathbf{M}\ddot{\mathbf{w}} + \mathbf{C}_D\dot{\mathbf{w}} + \mathbf{K}\ \mathbf{w} = F_p(E)\mathbf{b} + \mathbf{f}_d \tag{3.12}$$

is obtained. Here $\mathbf{w}(t) = [w_1(t), \cdots, w_N(t)]$, and $\mathbf{M} \in \mathbb{R}^{N\times N}$, $\mathbf{C}_D \in \mathbb{R}^{N\times N}$ and $\mathbf{K} \in \mathbb{R}^{N\times N}$ denote the mass, damping and stiffness matrices. The vectors $\mathbf{b} \in \mathbb{R}^N$ and $\mathbf{f}_d \in \mathbb{R}^N$ include the integrated basis functions related to the control input and the disturbance loads, respectively. Components of the system matrices and vectors can be found in [39] and in the Appendix A.

3.1.2 Lumped Rod Model

The assumption that electric fields and stresses are uniform along the PZT rod length motivates the conclusion that strains also exhibit negligible $x-$dependence [46]. Since the position of the sample is dictated by the position of the PZT rod tip at $x = L$, this motivates the development of a lumped model which quantifies $w_L(t) = w(t,L)$.

From the assumption of uniform strains along the rod length, we take $\epsilon = w(t,L)/L$ in (3.3). Balancing the force σA for the rod with those of the restoring mechanism yields the lumped model

$$m\frac{d^2w_L}{dt^2}(t) + c\frac{dw_L}{dt} + kw_L(t) = F_p(E) + F_d(t) \tag{3.13}$$

where

$$m = \rho AL + m_L, \qquad c = \frac{c_D A}{L} + c_L, \qquad k = \frac{Y^P A}{L} + k_L. \tag{3.14}$$

The term $F_p(E)$ on the right hand side of (3.14) is specified by (3.6).

The model (3.13) can also be written as the first-order ODE system

$$\begin{aligned} \dot{\mathbf{x}}(t) &= \mathbf{A}\mathbf{x}(t) + [\mathbf{B}(v)](t) + \mathbf{F}_d(t), \qquad \mathbf{x}(0) = \mathbf{x}_0 \\ y(t) &= \mathbf{c}^T\mathbf{x}(t) \end{aligned} \tag{3.15}$$

where $\mathbf{x}(t) = [w_L(t), \dot{w}_L(t),]$. The matrix $\mathbf{A}$ incorporates the mass, damping and stiffness terms given in (3.14). The mass and stiffness terms could slightly vary in time due to the internal damping and heating that depends on the strain rate. Here $[\mathbf{B}(v)](t)$ includes the nonlinear input where $v(t)$ is defined as the electric field. The initial conditions are defined by $\mathbf{x}_0$. The output of the system $y(t)$ is a function of the system states according to the vector $\mathbf{c}$. In the nanopositioning stage, it is assumed that only the displacement at $x = L$ is observed which yields $\mathbf{c} = \begin{bmatrix} 1 & 0 \end{bmatrix}^T$. External disturbances are incorporated in $\mathbf{F}_d(t)$. The system matrix $\mathbf{A}$, input vector $\mathbf{B}(v)$ and disturbance load $\mathbf{F}_d(t)$ are

$$\mathbf{A} = \begin{bmatrix} 0 & 1 \\ -k/m & -c/m \end{bmatrix}, \quad \mathbf{B}(v) = m^{-1}F_p(v) \begin{bmatrix} 0 \\ 1 \end{bmatrix}, \quad \mathbf{F}_d(t) = \begin{bmatrix} 0 \\ m^{-1}f_d(t) \end{bmatrix}. \tag{3.16}$$

To further simplify the dynamics of the PZT stacked actuator, we shall linearize the electrostrictive relationship about a biasing polarization level. This is motivated by the physical observation that transducers operating about a biased electric filed exhibit a nearly linear relation between polarization and strains for moderate drive level regimes. This yields the approximate relation $B(v)$ as $B(v) = P(v) \begin{bmatrix} 0 \\ m^{-1}b \end{bmatrix}$.

Two temporal discretization methods of the system (3.15) are used to numerically analyze the dynamic performance. First, the implicit Euler rule is adopted since it is A-stable and requires minimum computer storage capability. The implicit Euler discretization yields the relations for each iteration

$$\begin{aligned} \mathbf{x}_{k+1} &= (\mathbf{I} - \Delta t\mathbf{A})^{-1}\Big(\mathbf{x}_k + [\mathbf{B}(v_k)] + \mathbf{F}_d(t_{k+1})\Big) \\ x(0) &= x_0 \end{aligned}$$

where a temporal step-size Δt is employed giving a discretization in time defined by $t_k = k\Delta t$. The values x_k approximate $x(t_k)$. The matrix $\mathbf{I} - \Delta t\mathbf{A}$ is created once for numerical implementation yielding approximate solutions with $O(h^2, (\Delta t))$ accuracy. In the discretized relation, only values for the control input as the present time t_k are included in the temporal

discretization since the control input can only be dependent on the current and previous states.

Secondly, the trapezoid rule is used to numerically analyze the performance. The trapezoidal discretization yields the relation for each iteration

$$\begin{aligned} \mathbf{x}_{k+1} &= \mathbf{U}_{\mathbf{x}_k} + \mathbf{V}[\mathbf{B}(v_k)] + \frac{1}{2}\mathbf{V}[\mathbf{F}_d(t_k) + \mathbf{F}_d(t_{k+1})] \\ \mathbf{x}(0) &= \mathbf{x}_0. \end{aligned}$$

Similar to the implicit Euler, a temporal step size Δt generates a discretization $t_k = k\Delta t$. The matrices

$$\begin{aligned} \mathbf{U} &= \left[\mathbf{I} - \frac{\Delta t}{2}\mathbf{A}\right]^{-1}\left[\mathbf{I} + \frac{\Delta t}{2}\mathbf{A}\right] \\ \mathbf{V} &= \Delta t\left[\mathbf{I} - \frac{\Delta t}{2}\mathbf{A}\right]^{-1} \end{aligned}$$

are created once for numerical implementation yielding approximate solution with $O(h^2, (\Delta t))$.

3.2 Control Design

Here we outline the general tracking problem to provide relations used when developing the adaptive control tracking law.

To simplify the control design, we will just consider a lumped parameter model (3.15) with the linear forcing term $B(u)$ for the control designs. The lumped parameter model assumes the σ - ϵ and E - P are uniform along the rod which has been shown be a reasonable approximation for many architectures [46]. It was also determined that this lumped parameter model was sufficient to accurately model the piezoelectric actuator dynamics for a 100 Hz scan rate; thus the state space system reduces to scalar coefficients. Then the dynamical system takes the form

$$\begin{aligned} \dot{\mathbf{x}}(t) &= \mathbf{A}\mathbf{x}(t) + \mathbf{b}u(t), \quad u(t) = [P(v)](t) \\ y(t) &= \mathbf{c}^T\mathbf{x}(t) \end{aligned} \tag{3.17}$$

with the system state $\mathbf{x}(t) \in \mathbb{R}^2$ and the system output $y(t) = x_1(t) \in \mathbb{R}$. Term $u(t) = [P(v)](t) \in \mathbb{R}$ is the driving force generated by the hysteretic actuator $\mathcal{P}$ where $v(t)$ is the input electric field to the actuator. The system matrix $\mathbf{A}$ is specified in (3.16).

Next we incorporate the approximate of the inverse of homogenized energy model as the compensator and use it before the actuator $\mathcal{P}$ as depicted in Figure 1.2. The driving force can be then formulated as

$$u(t) = [P(v)](t) = [P\widehat{P}^{-1}(u_d)](t) \tag{3.18}$$

where the signal $u_d(t)$ is used as the input of the inverse compensator $\widehat{P}^{-1}(\cdot)$ to generate the control field $v(t)$ which is then applied to the hysteretic device.

While such model-based inverse compensation is never exact due to the discretization or modeling errors, the mismatch between inverse and hysteretic actuator can be designed to be small and thus be assumed bounded in magnitude; i.e.,

$$u(t) = u_d(t) + \sigma(t) \tag{3.19}$$

where $\sigma(t)$ is the inversion error and satisfies $|\sigma(t)| \leq \Delta_0 \in \mathbb{R}$. We can thus model the inversion error as an external time-varying disturbance. Then the dynamic system can be rewritten as

$$\begin{aligned} \dot{\mathbf{x}}(t) &= \mathbf{A}\mathbf{x}(t) + \mathbf{b}\big(u_d(t) + \sigma(t)\big) \\ y(t) &= \mathbf{c}^T\mathbf{x}(t). \end{aligned} \tag{3.20}$$

However, in general this approximation is not necessarily valid for all rod structures and operating regimes. In these cases, implementation of the discretized PDE is necessary.

3.3 Concluding Remarks

This chapter summarized techniques for modeling the forces, strains and displacements in a prototypical AFM nanopositioning stage driven by the piezoelectric actuators. Under certain conditions, the transducers can be accurately modeled as a second-order-ODE. While the transducer model in this chapter is developed in the context of an ferroelectric material, the techniques can be applied to model transducers incorporating other smart materials including including magnetostrictives and under certain conditions, shape memory alloys.

Chapter 4

Model Reference Adaptive Control

Adaptive control often focuses on systems where some of the parameters are unknown or slowly time-varying. In this case, the basic idea is to estimate the unknown parameters online using parameter estimation methods, and then to use the estimated parameters, in place of the unknown ones, in the feedback control law. Progress in nonlinear systems theory in the mid 1970's to 1980's led to the development of fundamental theory for stable adaptive control architectures, see [13, 21, 25, 28] and references therein. Two of the important branches of adaptive control are: model reference control and pole placement. In model reference control, the objective is asymptotic tracking of a large class of signals as it is restricted to minimum phase plants. In pole placement, the objective is stability and possibly asymptotic tracking of a small class of signals such as steps, and the minimum phase property is not required. One of the most important schemes in the first branch of adaptive control is model reference adaptive control (MRAC). Figure 4.1 shows the block diagram of a classical MRAC architecture. In this approach, there is a stable reference model which describes the desired input-output properties of the closed-loop system. The control system consists of a control signal $K(\theta)$ with modifiable parameters θ along with a modification mechanism, which estimates the controller parameters $\theta(t)$ online. Here r is an exogenous signal and $e = y - y_m$ is the tracking error between the reference model output and the physical system output.

The goal is to design the control law so that signals in the closed-loop system are bounded and, for every bounded reference signal $r(t)$, the tracking error e converges asymptotically to zero with time. The classical assumptions [25, 28] are

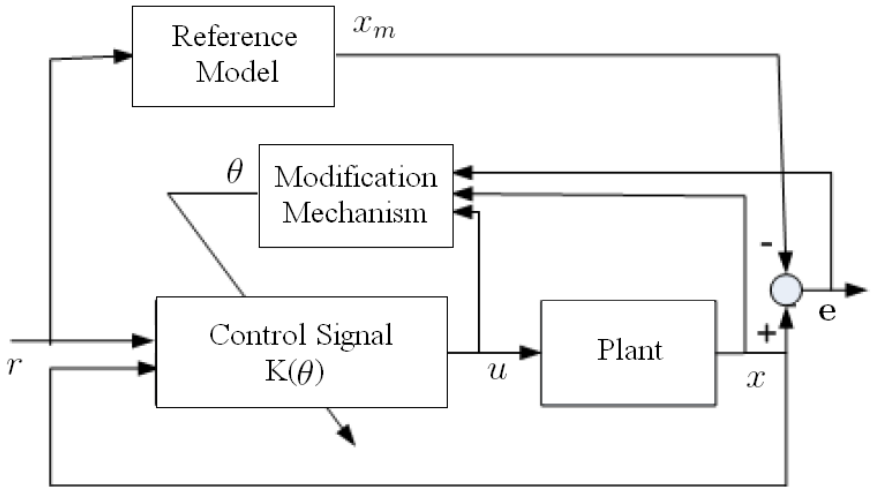

Figure 4.1: Block diagram of a MRAC system.

- the physical system is minimum phase,
- an upper bound on the physical system order is known,
- the physical system's relative degree is known, and
- the sign of the system's high frequency gain is known.

In the following sections, we develop a modified MRAC law for the placement of the stage of the AFM illustrated in Figure 3.1. The control designs will employ inverse compensation based on the hysteresis model described in Chapter 2 to attenuate the nonlinearities and hysteretic behavior in the piezoelectric stack actuator.

4.1 Problem Formulation

In this section, the structure of the uncertain physical system, reference model and the controller are presented. The SISO linear, time-varying system is described by (3.17) and (3.20).

A stable SISO reference model is given by

$$\begin{aligned} \dot{\mathbf{x}}_m(t) &= \mathbf{A}_m \mathbf{x}_m(t) + b_m r(t) \\ y_m(t) &= \mathbf{c}_m^T \mathbf{x}_m(t). \end{aligned} \tag{4.2}$$

where $\mathbf{x}_m(t) = \begin{bmatrix} x_m & \dot{x}_m \end{bmatrix} \in \mathbb{R}^2$ is the reference model state and $r(t) \in \mathbb{R}$ is the bounded, piecewise continuous reference input. We set $\mathbf{c}_m^T = \begin{bmatrix} 1 & 0 \end{bmatrix}$, which implies that we are just

tracking the position variable; i.e., $y_m = x_m$. The reference model describes the desired behavior of the closed-loop system and is chosen to be stable. The goal is to design a control $u(t)$ that provides stability and ensures that the physical system state tracks the model reference state asymptotically. To this end, we define the state tracking error as

$$\mathbf{e}(t) = \mathbf{x}(t) - \mathbf{x}_m(t). \tag{4.3}$$

We then have that the output tracking error is $e = y - y_m = \mathbf{e}(1)$.

4.2 Adaptive Control Designs

In MRAC, the dynamic system can be regulated so that the pole of the plant can coincide with the pole of the reference model by using the parameter vector $[\hat{a}_x,\, \hat{a}_{\dot{x}}]$, and the DC gain of the physical plant can coincide with the DC gain of the reference model by using the parameter $\hat{a}_r$. This has been widely analyzed in the literature of adaptive control; e.g., see [16, 26] To balance the hysteresis inversion error $\sigma(t)$ in (3.19) and also other possible external disturbances $\mathbf{f}_d$, we introduce an additional term d in the control signal design. It turns out that it is sufficient that there be bounds on the derivatives of these parameters, although jumps are also tolerated. To proceed, we collect all the parameters of the system (3.20) into a single vector $\Theta = \begin{bmatrix} a_r, & a_x, & a_{\dot{x}} \end{bmatrix}$. As detailed in [23], assumptions on the vector Θ are the following:

Assumption 4.1: (Compact set) There exists a compact set Ω such that

$$\Theta(t) \in \Omega \quad \text{for all} \quad t \geq 0.$$

Assumption 4.2: (Bounded derivative) There exists a constant M_Θ such that

$$\|\dot{\Theta}\| \leq M_\Theta.$$

Then the control signal is given by

$$u_d = \hat{a}_r\, r + \begin{bmatrix} \hat{a}_x & \hat{a}_{\dot{x}} \end{bmatrix} \begin{bmatrix} x \\ \dot{x} \end{bmatrix} - \widehat{d} = \widehat{\Theta}^T \Phi \tag{4.4}$$

with

$$\begin{aligned} \widehat{\Theta} &= \begin{bmatrix} \widehat{a}_r, & \widehat{\mathbf{a}}_x, & \widehat{d} \end{bmatrix}^T, \quad \widehat{\mathbf{a}}_x = \begin{bmatrix} \widehat{a}_x, & \widehat{a}_{\dot{x}} \end{bmatrix}^T \\ \Phi &= \begin{bmatrix} r, & \mathbf{x}, & -1 \end{bmatrix}^T \end{aligned} \tag{4.5}$$

denoting the estimated parameter vectors.

4.2.1 Design of Adaptation Algorithms

Substitution of the control signal $u_d(t)$ from Equation (4.4) into the physical system (3.20) and rewriting it as a second-order ODE form yields

$$\ddot{x} = -\frac{c_p - \hat{a}_{\dot{x}}}{m_p}\,\dot{x} - \frac{k_p - \hat{a}_x}{m_p}\,x + \frac{\hat{a}_r}{m_p}\,r - \frac{1}{m_p}(\widehat{d} - \sigma). \tag{4.6}$$

Also reformulating the reference model (4.2) into a second-order ODE form yields

$$\ddot{x}_m = -\frac{c}{m}\,\dot{x}_m - \frac{k}{m}\,x_m + \frac{1}{m}\,r. \tag{4.7}$$

Comparison of (4.6) and (4.7) gives the values

$$a_r^* = \frac{m_p}{m}\,, \qquad \mathbf{a}_x^* = \begin{bmatrix} a_x^*, & a_{\dot{x}}^* \end{bmatrix}^T = \begin{bmatrix} k_p - k\,\dfrac{m_p}{m}, & c_p - c\,\dfrac{m_p}{m} \end{bmatrix} \tag{4.8}$$

of the control parameter, which would lead the system output to the desired reference output (4.7) and yields bounded tracking errors.

Next, we derive the error dynamics.

4.2.2 Error Equation

Denote the parameter errors as

$$\widetilde{\Theta} = \widehat{\Theta} - \Theta^*, \quad \text{with} \quad \Theta^* = \begin{bmatrix} a_r^* & \mathbf{a}_x^* & d \end{bmatrix}. \tag{4.9}$$

Then the tracking error dynamic takes the form

$$\dot{\mathbf{e}} = \mathbf{A}_m\mathbf{e} + \frac{\mathbf{b}}{m_p}\widetilde{\Theta}^T\Phi \tag{4.10}$$

where

$$\mathbf{e} = \begin{bmatrix} e \\ \dot{e} \end{bmatrix}, \qquad \mathbf{A} = \begin{bmatrix} 0 & 1 \\ -\dfrac{k}{m} & -\dfrac{c}{m} \end{bmatrix}, \qquad \mathbf{b} = \begin{bmatrix} 0 \\ 1 \end{bmatrix}.$$

We then choose the adaptation law as

$$\dot{\widehat{\Theta}} \;=\; -\Gamma\,\mathbf{b}^T\mathbf{e}\,\Phi + F(t), \quad \Phi = \begin{bmatrix} r & \mathbf{x} & -1 \end{bmatrix} \tag{4.11}$$

with $F(t)$ a modification term

$$F(t) = -\Gamma\,\zeta\widehat{\Theta}(t). \tag{4.12}$$

Here

$$\zeta = \begin{cases} 0, & \text{if } \|\widehat{\Theta}\|_2 \le \|\Theta^*\|_{max} \\ \zeta_0, & \text{else} \end{cases}$$

with $\zeta_0 > 0$ and $\|\Theta^*\|_{max}$ is a known upper bound on the norm of the (unknown) matching controller parameter vector Θ^*.

4.3 Stability Analysis

We begin our stability analysis by showing that there exists a compact set Ω such that a solution to the error dynamics exists for $t \ge 0$ and certain components of the solution are uniformly bounded for any initial states in Ω.

Define the Lyapunov function candidate

$$V = \frac{1}{2}\,\frac{k}{m}\,e^2 + \frac{1}{2}\,\dot{e}^2 + \frac{1}{2}\,\frac{1}{\Gamma m_p}\widetilde{\Theta}^T\widetilde{\Theta}. \tag{4.13}$$

Denote $\Theta_r = \begin{bmatrix} a_r, & \mathbf{a}_x \end{bmatrix}^T$ and $\Phi_r = \begin{bmatrix} r, & \mathbf{x} \end{bmatrix}^T$; i.e., $\Theta = \begin{bmatrix} \Theta_r, & d \end{bmatrix}^T$ and $\Phi = \begin{bmatrix} \Phi_r, & -1 \end{bmatrix}^T$. We then can get the time derivative of V along the trajectories of (4.10) and (4.11)

$$\begin{aligned} \dot{V} &= \frac{k}{m}e\dot{e} + \dot{e}\ddot{e} - \frac{1}{m_p}\widetilde{\Theta}^T\big(\mathbf{b}^T\mathbf{e}\,\Phi + \zeta\widehat{\Theta}\big) \\ &= -\frac{c}{m}\|\mathbf{b}^T\mathbf{e}\|^2 + \frac{\zeta\mathbf{b}^T\mathbf{e}}{m_p} - \frac{\zeta}{m_p}\widetilde{\Theta}_r^T\widehat{\Theta}_r \\ &\le -\frac{c}{m}\|\mathbf{e}\|^2 + \frac{2\Delta_0\,\|\mathbf{e}\|}{m_p} - \frac{\zeta}{m_p}\widetilde{\Theta}_r^T\widehat{\Theta}_r \\ &= -\frac{c}{m}\left(\|\mathbf{e}\| - \frac{m\,\Delta_0}{c\,m_p}\right)^2 + \frac{m\Delta_0^2}{c\,m_p^2} - \frac{\zeta}{m_p}\widetilde{\Theta}_r^T\widehat{\Theta}_r. \end{aligned}$$

Note that

$$\|\Theta_r^*\|^2 = \|\widehat{\Theta}_r - \widetilde{\Theta}_r\|^2 = \|\widehat{\Theta}_r\|^2 + \|\widetilde{\Theta}_r\|^2 - 2\widetilde{\Theta}_r^T\widehat{\Theta}_r$$

$$\implies\; -\zeta\widetilde{\Theta}_r^T\widehat{\Theta}_r \le -\frac{\zeta}{2}\|\widetilde{\Theta}_r\|^2 + \frac{\zeta}{2}\|\Theta_r^*\|^2.$$

Substituting the above inequality into (4.13) yields

$$\dot{V} \leq -\frac{c}{m}\left(\|\mathbf{e}\| - \frac{m\,\Delta_0}{c\,m_p}\right)^2 + \frac{m\Delta_0^2}{c\,m_p^2} - \frac{\zeta}{2m_p}\|\widetilde{\Theta}_r\|^2 + \frac{\zeta}{2m_p}\|\Theta_r^*\|^2.$$

Define the constants c_1 and c_2 by

$$\begin{aligned} c_1 &= \frac{m\,\Delta_0}{c\,m_p} \\ c_2 &= \frac{m\Delta_0^2}{c\,m_p^2} + \frac{\zeta}{2m_p}\|\Theta_r^*\|^2. \end{aligned}$$

Then $\dot{V} < 0$ as long as one of the following conditions holds:

$$\|\mathbf{e}\| > c_1 + \sqrt{\frac{m\,c_2}{c}}, \tag{4.14}$$

$$\|\widetilde{\Theta}_r\| > \min\left\{M_\Theta,\, \sqrt{\frac{2\,m_p\,c_2}{\zeta_0}}\right\}. \tag{4.15}$$

Define a compact set

$$\Omega = \left\{(\mathbf{e},\, \widetilde{\Theta}_r)\,|\,\|\mathbf{e}\| \leq c_1 + \sqrt{\frac{m\,c_2}{c}}\,,\quad \|\widetilde{\Theta}_r\| \leq \min\left\{M_\Theta,\, \sqrt{\frac{2\,m_p\,c_2}{\zeta_0}}\right\}\right\}. \tag{4.16}$$

Using Theorem 7.1 and Corollary 7.1 in [48], we see that $V_{max} = \max_\Omega(V)$ exists, so we can conclude that $V(t)$ is bounded from above by V_{max} and $(e,\, \widetilde{\Theta}_r)^T$ converges to the bounded compact set Ω for all any initial $(e(0),\, \widetilde{\Theta}_r(0)) \in \Omega = \{(e,\, \widetilde{\Theta}_r)\,|\,V \leq V_{max}\}$.

4.4 Numerical Results

In this section, we conduct a simulation to examine the effectiveness of the proposed controller design.

Consider the system

$$\begin{aligned} &1.5\,\ddot{x}(t) + 1.8\,\dot{x}(t) + 8.1\,x(t) = u(t)\,, \\ &u = [\mathcal{H}(v)](t) \end{aligned} \tag{4.17}$$

or alternatively,

$$\begin{aligned} &\dot{\mathbf{x}}(t) = \mathbf{A}\mathbf{x}(t) + \mathbf{b}u(t), \quad u(t) = [P(v)](t) \\ &y(t) = \mathbf{c}^T\mathbf{x}(t) \end{aligned}$$

with

$$\mathbf{A} = \begin{bmatrix} 0 & 1 \\ -\frac{1.8}{1.5} & -\frac{8.1}{1.8} \end{bmatrix}, \quad \mathbf{b} = \begin{bmatrix} 0 \\ \frac{1}{1.5} \end{bmatrix}, \quad \text{and } \mathbf{c} = \begin{bmatrix} 1 \\ 0 \end{bmatrix}$$

in the ODE system form of (3.17).

The plant parameters $m_p = 1.5$, $c_p = 1.8$ and $k_p = 8.1$ are assumed to be unknown to the adaptive controllers. The reference model is chosen to be

$$\ddot{x}_m(t) + 1.4\,\dot{x}_m(t) + 10\,x_m(t) = r(t). \tag{4.18}$$

or alternatively,

$$\begin{aligned} \dot{\mathbf{x}}_m(t) &= \mathbf{A}_m \mathbf{x}_m(t) + b_m r(t) \\ y_m(t) &= \mathbf{c}_m^T \mathbf{x}_m(t). \end{aligned} \tag{4.2}$$

with

$$\mathbf{A}_m = \begin{bmatrix} 0 & 1 \\ -1.4 & -10 \end{bmatrix}, \quad \mathbf{b}_m = \begin{bmatrix} 0 \\ 1 \end{bmatrix}, \quad \text{and } \mathbf{c}_m = \begin{bmatrix} 1 \\ 0 \end{bmatrix}$$

in the ODE system form of (4.2).

The control law is taken to be

$$\begin{aligned} u_d(t) &= \widehat{a}_r\, r(t) + \widehat{a}_{\dot{x}}\, \dot{x}(t) + \widehat{a}_x\, x(t) - \widehat{d}(t) \\ v(t) &= [\mathcal{H}^{-1}(u_d)](t). \end{aligned} \tag{4.19}$$

The adaptation law is

$$\begin{aligned} \dot{\widehat{a}}_r(t) &= -\Gamma\, \mathbf{b}^T \mathbf{e}\, r(t) + F(t), \qquad a_r^* = 1.5 \\ \dot{\widehat{\mathbf{a}}}_x(t) &= -\Gamma\, \mathbf{b}^T \mathbf{e}\, \mathbf{x}(t) + F(t), \qquad \mathbf{a}_x^* = [-6.9,\, -0.3\,]^T \end{aligned} \tag{4.20}$$

and the disturbance parameter yields

$$\dot{\widehat{d}} = \Gamma \mathbf{b}^T \mathbf{e} + F(t). \tag{4.21}$$

We choose a conservative upper bound on the norm of the unknown parameter vector Θ; i.e., we set $\|\Theta^*\|_{max} = 15$ in the definition (4.12) of $F(t)$.

The initial values of all parameters of the controller and plant are chosen to be 0, indicating that no a *priori* knowledge is given. The initial conditions of the plant and the model are both zero. System performance will be studied with different choices of reference input $r(t)$.

The simulation results of the modified MRAC are shown in Figure 4.2 for the reference input $r(t) = 4\sin(3t)$ and in Figure 4.3 for the same reference input $r(t) = 4\sin(3t)$ but with an external disturbance $f_d(t) = 0.4\sin(30\,t)$. Figure 4.4 and Figure 4.5 illustrate the reference inputs $r(t) = 4\,t$ and $r = 4$, respectively. The control signals and hysteresis inversion errors generated for each reference input are plotted in Figure 4.6 and Figure 4.7.

We observe from Figure 4.2(a) that the position tracking error $e(t) = y(t) - y_m(t)$ decays to zero and the control signal is bounded (see Figure 4.6(a)), but it takes more than 10 seconds for adaptation and the tracking error at the first 5 seconds is about 40%. In Figure 4.2(b), we also notice that although the parameter vector $\hat{\Theta}$ doesn't converge to the exact value Θ^*, the errors are still bounded and satisfy the inequality given in (2.14). Figure 4.3 shows the performance of the modified MRAC for the same reference input but adding a disturbance to the $r(t) = 4\sin(3t)$, and we see that the tracking error is almost zero and the estimated parameters are close the actual ones, which means that the modified MRAC can effectively eliminate the disturbance but the transient behavior is as poor as the first example. In the next simulation (see Figure 4.4) we are tracking a linear reference signal. Figure 4.4 shows that although the tracking error converges to a small value and the transient behavior is guaranteed , but because the initial conditions are poor, the parameters estimated errors are large and the control signal is unbounded.

4.5 Concluding Remarks

In this chapter, we introduced a modified MRAC method and demonstrated its strengths and weaknesses. In this method, a modification mechanism is used to estimate unknown plant parameters, and these are used to update control parameters accordingly. The approach can tolerate parameter uncertainty. While the asymptotical behavior is always guaranteed, the transient behavior may be poor if the initial estimate is poor or the parameters uncertainty is too large. In response to this, another approach of adaptive control is discussed in the next chapter that has the following features:

- it provides smooth transient behavior (immediate tracking rather than asymptotic),
- it allows for rapidly time-varying parameters,
- the effect of initial conditions decays exponentially to zero, and
- the control signal is modest in size.

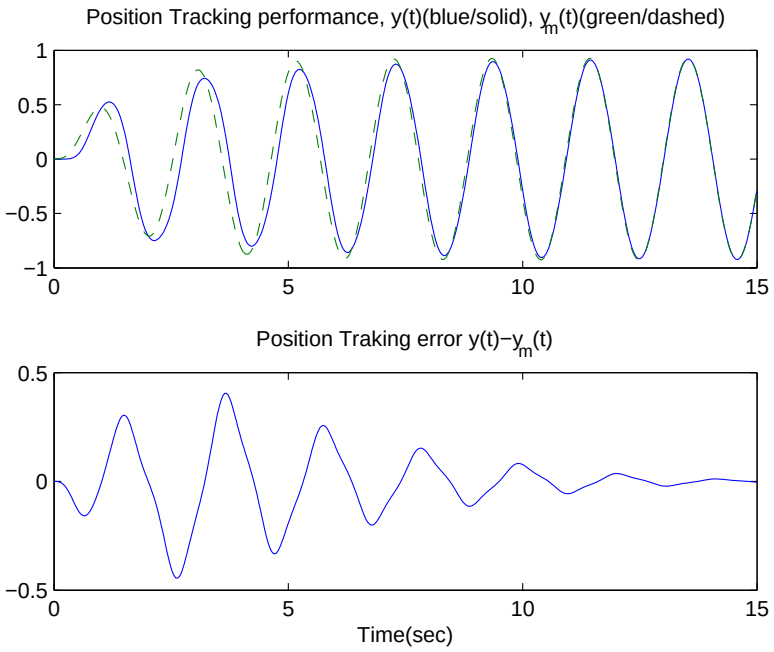

(a)

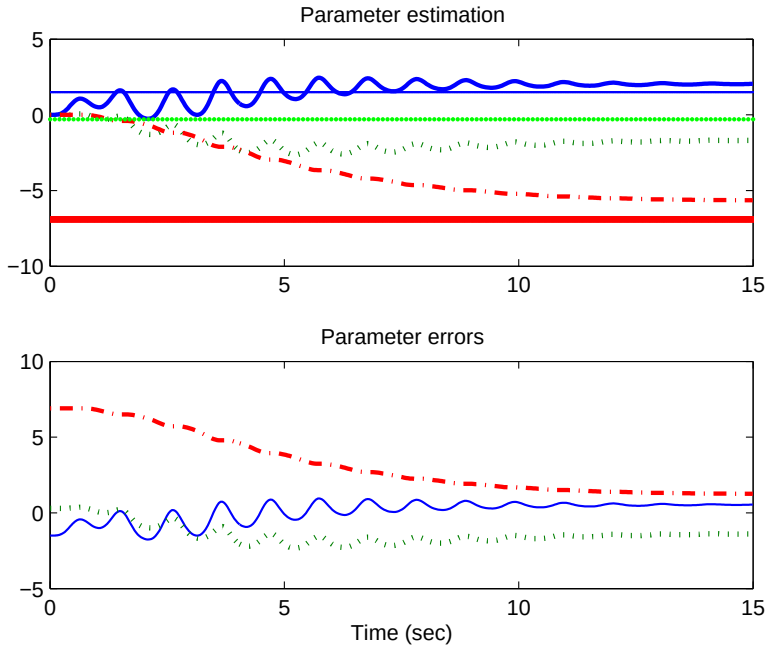

(b)

Figure 4.2: Performance of modified MRAC for reference input $r(t) = 4\sin(3t)$: (a) position tracking performance and error; (b) estimated parameters with their true values and parameter tracking errors: a_r (solid), $a_{\dot{x}}$ (dotted), a_x (dashed).

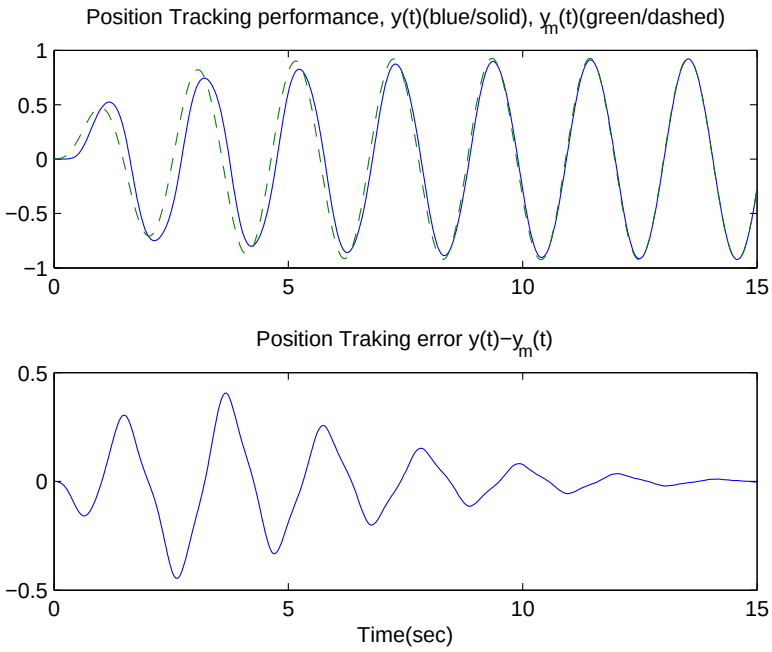

(a)

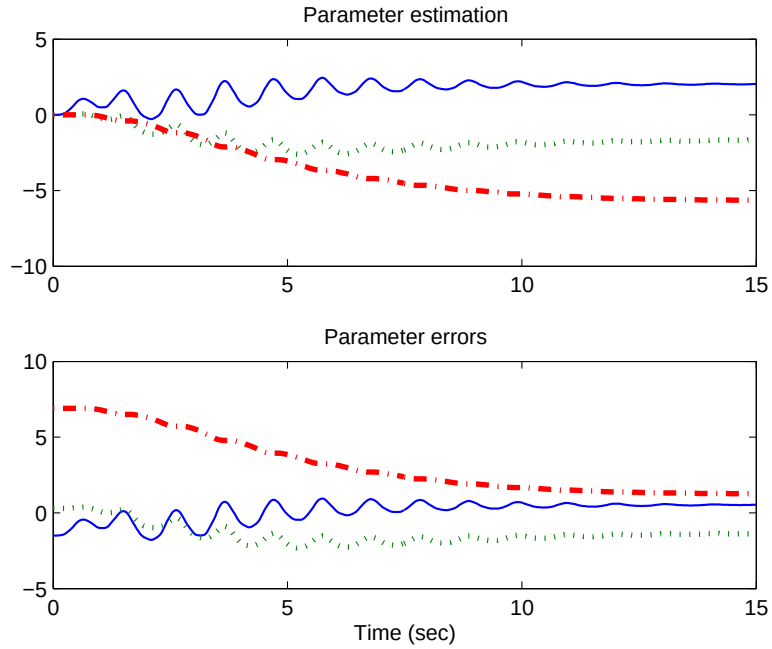

(b)

Figure 4.3: Performance of modified MRAC for reference input $r(t) = 4\sin(3t)$ with an external disturbance $f_d = 0.4\sin(30\,t)$: (a) position tracking performance and error; (b) estimated parameters and errors: a_r (solid), $a_{\dot{x}}$ (dotted), a_x (dashed).

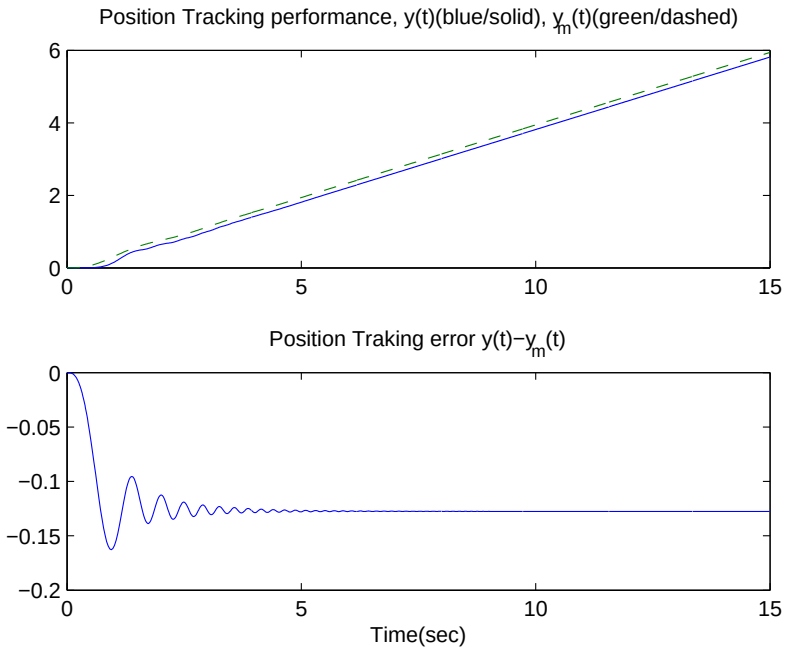

(a)

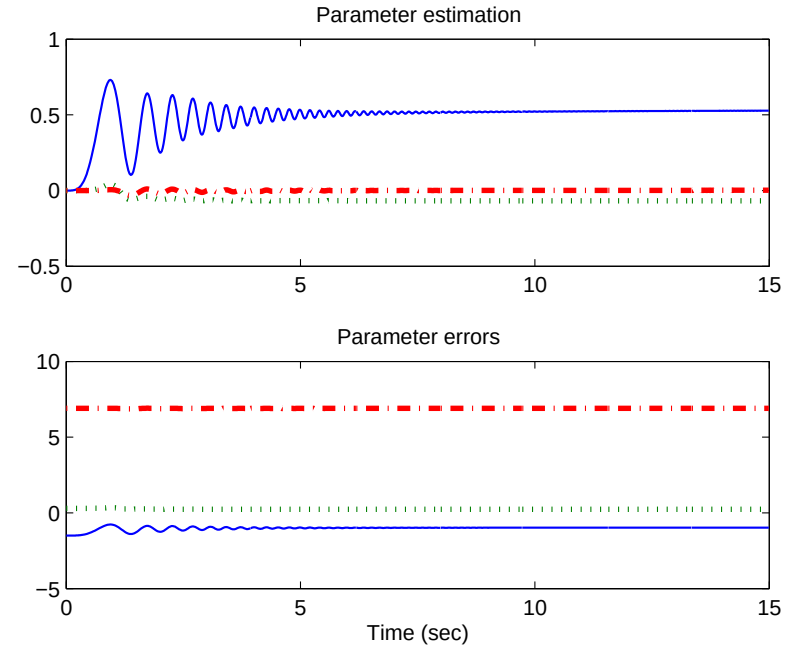

(b)

Figure 4.4: Performance of modified MRAC for reference input $r(t) = 4\,t$: (a) position tracking performance and error; (b) estimated parameters and errors: a_r (solid), $a_{\dot{x}}$ (dotted), a_x (dashed).

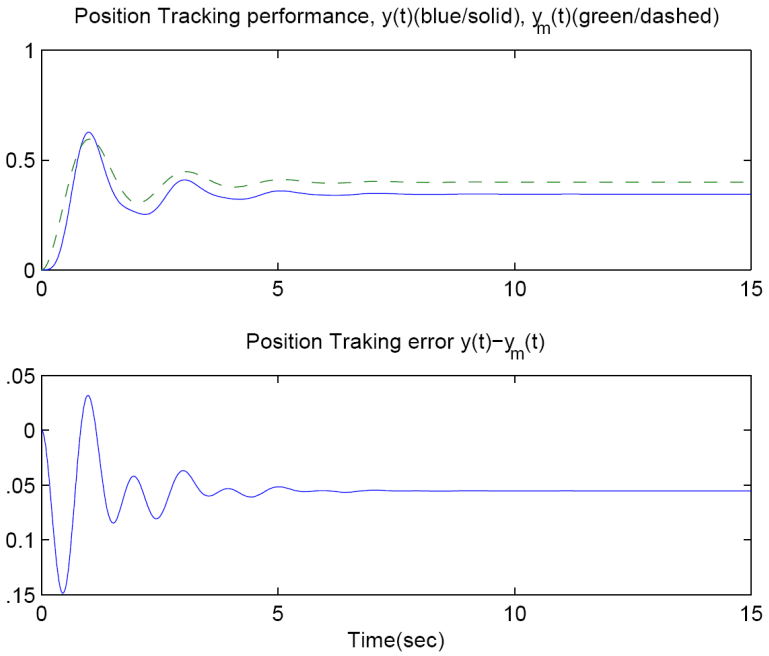

(a)

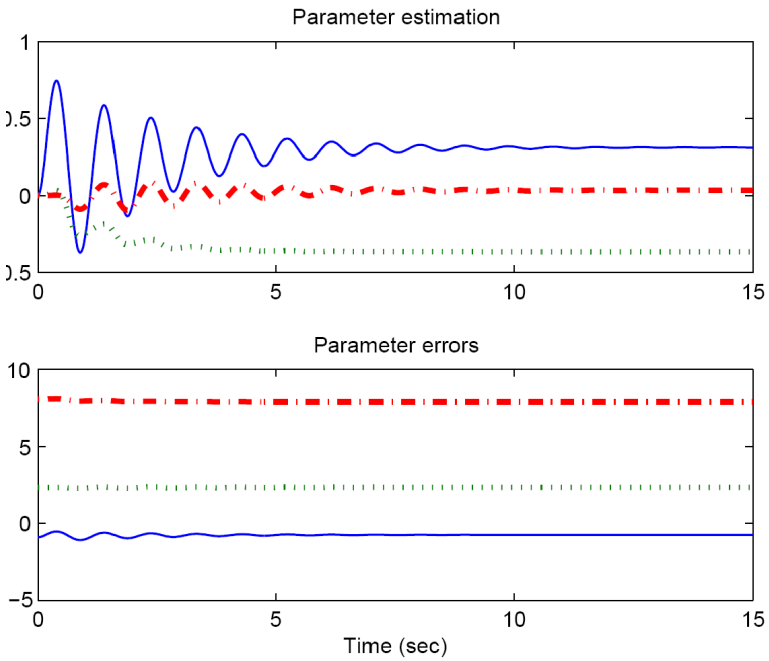

(b)

Figure 4.5: Performance of modified MRAC for reference input $r(t) = 4$: (a) position tracking performance and error; (b) estimated parameters and errors: a_r (solid), $a_{\dot{x}}$ (dotted), a_x (dashed).

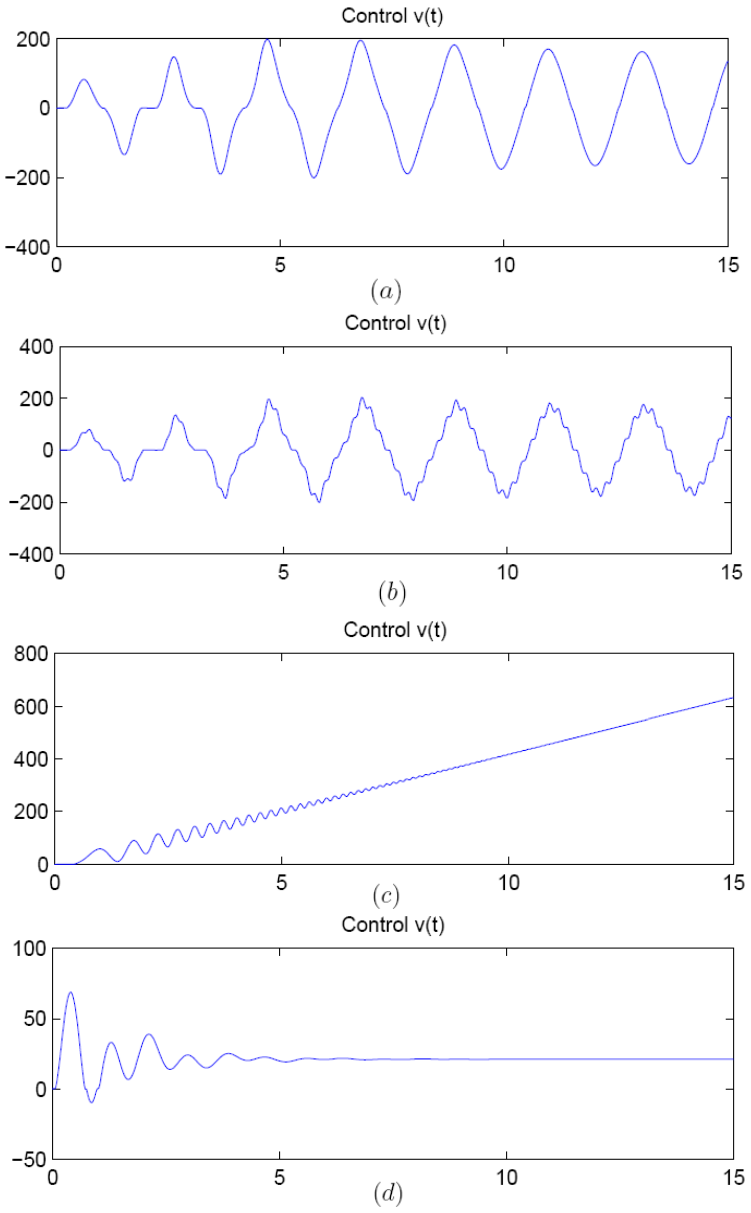

Figure 4.6: Control signals for reference inputs: (a) $r(t) = 4\sin(3t)$; (b) $r(t) = 4\sin(3t) + 0.3\sin(30t)$; (c) $r(t) = 4\,t$; (d) $r = 4$.

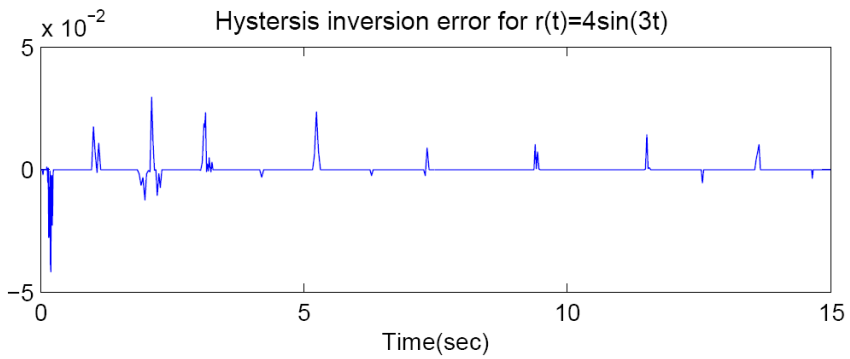

(a)

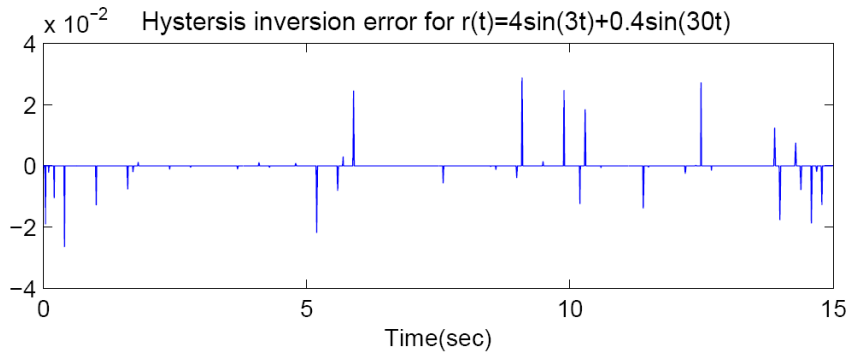

(b)

Figure 4.7: Hysteresis inversion error generated in the tracking process for the reference input (a) $r(t) = 4\sin(3t)$, and (b) $r(t) = 4\sin(3t) + 0.4\sin(30t)$.

Chapter 5

$\mathcal{L}_1$ Adaptive Control

Model Reference Adaptive Control (MRAC) was originally developed to control linear systems with unknown coefficients [26, 38]. That architecture is facilitated by the Lyapunov stability theory which gives sufficient conditions for stable performance without characterizing the frequency properties of the resulting controller. Application of adaptive controllers was therefore largely restricted due to the fact that the system uncertainties during the transient response have led to unpredictable situations, involving control signals of high-frequency or large amplitudes, large transient errors or slow convergence rate of tracking errors, to name a few.

Improvement of the transient performance of adaptive controller has been addressed from various perspectives in numerous efforts [10, 16, 27, 38, 49, 59], etc. An example presented in [59] demonstrated that the system output can have overly poor transient tracking behavior before ideal asymptotic convergence can take place. On the other hand, in [58] the author proved that it may not be possible to optimize $\mathcal{L}_2$ and $\mathcal{L}_\infty$ performance simultaneously by using a constant adaptation rate. Following these results, modifications of adaptive controllers were proposed in [11, 49] that render the tracking error arbitrarily small in terms of both mean-square and $\mathcal{L}_\infty$ bounds. Further, it was shown in [11] that the modifications proposed in [11, 49] could be derived as a linear feedback of the tracking error, and the improved performance was obtained only due to a nonadaptive high-gain feedback in that scheme. In [38], a composite adaptive controller was proposed, which suggests a new adaptation law using both tracking error and prediction error that leads to less oscillatory behavior in the presence of high adaptation gains as compared to MRAC. In [1], it is shown

that an arbitrarily close transient bound can be achieved by enforcing parameter-dependent persistence excitation condition.

However, some important aspects of the transient performance analysis are missing in these papers. First, since the purpose of adaptive control is to ensure stable performance in the presence of modeling uncertainties, one needs to ensure that the changes in reference input and unknown parameters due to possible faults or unexpected uncertainties do not lead to unacceptable transient deviations or oscillatory control signals. This implies that a re-tuning of adaptation parameters is required. Second, one needs to ensure that whatever modifications or solutions are suggested for performance improvement of adaptive controllers, they are not achieved only via high-gain feedback. As compared to prior results in adaptive control, the architectures of $\mathcal{L}_1$ adaptive control theory proposed in [7, 8] have guaranteed robustness in the presence of fast adaptation. This is possible to achieve by appropriate modification of the control objective with the understanding that uncertainties in any feedback loop can be compensated for only within the bandwidth of the control channel. By explicitly incorporating the robustness specification into the problem formulation, it is possible to decouple adaptation from robustness via continuous feedback and increase the speed of adaptation, subject only to hardware limitations. With $\mathcal{L}_1$ adaptive control architectures, fast adaptation appears to be beneficial both for performance and robustness, while the trade-off between the two is resolved via the selection of the underlying filtering structure.

5.1 Mathematical Preliminaries

In this section we summarize basic definitions and facts from linear systems theory [19, 60].

5.1.1 Norm

Definition 5.1. For a signal $\xi(t), t \geq 0, \xi \in \mathbb{R}^n$, its truncated $\mathcal{L}_\infty$ norm and $\mathcal{L}_\infty$ norm are

$$\|\xi_t\|_{\mathcal{L}_\infty} = \max_{i=1,\cdots,n} \left(\sup_{0\leq\tau\leq t} |\xi_i(t)| \right)$$

$$\|\xi\|_{\mathcal{L}_\infty} = \max_{i=1,\cdots,n} \left(\sup_{t\geq 0} |\xi_i(t)| \right)$$

where ξ_i is the i^{th} component of ξ.

Definition 5.2. The $\|\cdot\|_\infty$ of an $m \times n$ matrix A is defined as

$$\|A\|_\infty = \max_i \sum_{j=1}^{n} |a_{ij}|.$$

5.1.2 Lyapunov Stability

Theorem 5.3. [*La-Salle's invariance principle*] Let $\Omega \subset \mathcal{D} \subset \mathbb{R}^n$ be a compact (i.e., closed and bounded) set that is positively invariant with respect to the dynamics

$$\dot{x} = f(x), \qquad x(0) = x_0, \qquad x \in \mathbb{R}^n,$$

where f is locally Lipschitz in x. let $V : \mathbb{R}^n \to \mathbb{R}$ be a continuously differentiable function on $\mathcal{D}$ such that $\dot{V}(x(t)) \leq 0$ in Ω. Let E be the set of all points in Ω where $\dot{V}(x(t)) = 0$ and let M be the largest invariant set contained in E. Then every solution starting in Ω converges to M as $t \to \infty$. If $\mathcal{D} = \mathbb{R}^n$, $V : \mathbb{R}^n \to \mathbb{R}$ is radially unbounded and $\dot{V}(x(t)) \leq 0$ for all $x \in \mathbb{R}^n$, then every solution starting in $\mathbb{R}^n$ converges to M; i.e., the statement holds globally.

A proof can be found in [19].

Lemma 5.4. (*[33], Theorem 8.7*) Suppose that for the linear state equation

$$\dot{x}(t) = A(t)x(t), \quad x(t_0) = x_0,$$

with $A(t)$ continuously differentiable, there exist positive constants μ_A, μ_λ such that for all $t \geq 0, \|A(t)\|_\infty \leq \mu_A$, and at each time t the eigenvalue of $A(t)$ (point-wise eigenvalue) satisfy $\mathrm{Re}[\lambda(t)] \leq -\mu_\lambda$. Then there exists a positive constant ξ such that if the time-derivative of $A(t)$ satisfies $\|\dot{A}(t)\| \leq \xi$ for all $t \geq 0$, then the state equation is uniformly exponentially stable.

The proof of this lemma reveals an important property needed for stability analysis of the adaptive controller shown later, For details of this proof, refer to Theorem 8.7 of [33]. Notice that one important implication of this lemma is that if $\|\dot{A}(t)\|_\infty \leq \xi$ for all t and the point-wise eigenvalue condition holds, we have

$$\|\dot{P}(t)\|_\infty < 1$$

where $P(t)$ is the unique positive definite solution of

$$A^T(t)P(t) + P(t)A(t) = -I.$$

This result is crucial for the stability of adaptive controller, as shown later.

5.1.3 $\mathcal{L}_1$ Stability

Definition 5.5. The $\mathcal{L}_1$ norm of a bounded-input bounded-output (BIBO) stable proper single-input single-output (SISO) system is defined by

$$\|H(s)\|_{\mathcal{L}_1} = \int_0^\infty |h(t)|dt$$

where $h(t)$ is the impulse response of the transfer function $H(s)$.

Definition 5.6. The $\mathcal{L}_1$ norm of a BIBO stable proper SISO linear-time-varying (LTV) system is defined by

$$\|H\|_{\mathcal{L}_1} = \sup_{\forall t,\tau \geq 0} \int_\tau^t |g(t,\sigma)|d\sigma$$

where $g(t,\sigma)$ is the impulse response of the SISO system H.

Definition 5.7. The $\mathcal{L}_1$ norm of a BIBO stable proper m-input n-output (MIMO) system is defined by

$$\|H(s)\|_{\mathcal{L}_1} = \max_{i=1,\cdots,n} (\sum_{j=1}^{m}) \|h_{ij}(s)\|_{\mathcal{L}_1}$$

where $h_{ij}(s)$ is the corresponding entry of $H(s)$.

Definition 5.8. The $\mathcal{L}_1$ norm of a BIBO stable proper MIMO LTV system is defined by

$$\|H\|_{\mathcal{L}_1} = \max_{i=1,\cdots,n} (\sum_{j=1}^{m}) \|H_{ij}\|_{\mathcal{L}_1}$$

where $\|H_{ij}\|_{\mathcal{L}_1} = \sup_{\forall t,\tau,t\geq\tau} \int_\tau^t |g_{ij}(t,\sigma)|d\sigma$.

Lemma 5.9. For a BIBO stable proper MIMO system $H(s)$ with input $r(t) \in \mathbb{R}^m$ and output $x(t) \in \mathbb{R}^n$, we have

$$\|x_t\|_{\mathcal{L}_\infty} \leq \|H(s)\|_{\mathcal{L}_1} \|r_t\|_{\mathcal{L}_\infty}, \quad \forall t > 0.$$

Corollary 5.10. For a stable proper MIMO system $H(s)$, if the input $r(t) \in \mathbb{R}^m$ is bounded, then the output $x(t) \in \mathbb{R}^n$ is also bounded, and $\|x\|_{\mathcal{L}_\infty} \leq \|H(s)\|_{\mathcal{L}_1} \|r\|_{\mathcal{L}_\infty}$.

Lemma 5.11. (*[33], Lemma 12.4*) Consider the LTI system

$$\begin{aligned} \dot{x}(t) &= Ax(t) + Bu(t) \\ y(t) &= Cx(t), \quad x(t_0) = 0. \end{aligned}$$

Suppose the system is uniformly exponentially stable; i.e., there exist finite constant μ_B and μ_C such that for all $t \geq t_0$

$$\|B(t)\|_\infty \leq \mu_B, \quad \|C(t)\|_\infty \leq \mu_C.$$

Then the state equation is uniformly BIBO stable

$$\|x_t\|_{\mathcal{L}_\infty} \leq \|H\|_{\mathcal{L}_1}\|u_t\|_{\mathcal{L}_\infty}.$$

Further, if the input $u(t)$ is bounded, then $\|x\|_{\mathcal{L}_\infty} \leq \|H(s)\|_{\mathcal{L}_1}\|u\|_{\mathcal{L}_\infty}$.

Lemma 5.12. For a cascaded system $H(s) = H_2(s)H_1(s)$, where $H_1(s)$ and $H_2(s)$ are stable proper systems, we have $\|H(s)\|_{\mathcal{L}_1} \leq \|H_2(s)\|_{\mathcal{L}_1}\|H_1(s)\|_{\mathcal{L}_1}$.

Lemma 5.13.(*[19], Theorem 5.7*) For a cascaded LTV system $H = H_2H_1$, where $H_1(s)$ and $H_2(s)$ are stable proper LTV systems, we have $\|H(s)\|_{\mathcal{L}_1} \leq \|H_2(s)\|_{\mathcal{L}_1}\|H_1(s)\|_{\mathcal{L}_1}$.

This is the main statement we use in the control design to attain the $\mathcal{L}_1$ stability requirement for the tracking. Hence we analyze the proof of it. For detail of this proof refer to Theorem 5.7 of [19].

Proof: Let $(u_1(t), y_1(t))$ and $(u_2(t), y_2(t))$ be the input-output pairs of the system H_1 and H_2 respectively, and $u_2(t) = y_1(t)$. Further, let $u_1(t)$ be bounded. From Lemma (5.11) we have

$$\|y_1\|_{\mathcal{L}_\infty} \leq \|H_1\|_{\mathcal{L}_1}\|u_1\|_{\mathcal{L}_\infty},$$
$$\|y_2\|_{\mathcal{L}_\infty} \leq \|H_2\|_{\mathcal{L}_1}\|u_2\|_{\mathcal{L}_\infty}.$$

Since $H = H_2H_1$, it follows that

$$y_2(t) = Hu_1(t) = H_2\big(H_1u_1(t)\big) = H_2y_1(t).$$

Hence we have

$$\|y_2\|_{\mathcal{L}_\infty} \leq \|H_2\|_{\mathcal{L}_1}\|y_1\|_{\mathcal{L}_\infty} \leq \|H_2\|_{\mathcal{L}_1}\|H_1\|_{\mathcal{L}_1}\|u_1\|_{\mathcal{L}_\infty}, \tag{5.1}$$

Recalling the input-output relationship of LTV system, we can write

$$\begin{aligned}
\|y_2(t)\|_\infty &= \left\| \int_{t_0}^{t} C(t)\Phi(t,\sigma)B(\sigma)u_1(\sigma)d\sigma \right\|_\infty \\
&= \left\| \left[\textstyle\sum_{j=1}^{m} \int_{t_0}^{t} g_{1j}(t,\sigma)(u_1)_j(\sigma)d\sigma, \cdots, \sum_{j=1}^{m} \int_{t_0}^{t} g_{nj}(t,\sigma)(u_1)_j(\sigma)d\sigma \right]^T \right\|_\infty \\
&= \max_{i=1,\cdots,n} \left(\left| \textstyle\sum_{j=1}^{m} \int_{t_0}^{t} g_{ij}(t,\sigma)(u_1)_j(\sigma)d\sigma \right| \right) \\
&\leq \max_{i=1,\cdots,n} \left(\textstyle\sum_{j=1}^{m} \int_{t_0}^{t} |g_{ij}(t,\sigma)|\,|(u_1)_j(\sigma)| \right) \\
&\leq \max_{i=1,\cdots,n} \left(\textstyle\sum_{j=1}^{m} \sup_{\forall t,t_0,t\geq t_0} \int_{t_0}^{t} |g_{ij}(t,\sigma)|\,d\sigma \right) \sup_{\forall \sigma \geq t_0} |u_1(\sigma)|_\infty
\end{aligned}$$

where $g(t,\sigma)$ is the impulse response of H. Then we can get

$$\sup_{t\geq 0}\|y_2(t)\|_\infty \leq \|H\|_{\mathcal{L}_1}\sup_{\sigma\geq 0}\|u_1(\sigma)\|_\infty.$$

Thus, when $\|u_1\|_{\mathcal{L}_\infty}\leq 1$, we have $\sup_{\tau\geq 0}\|y_2(\tau)\|_\infty \leq \|H\|_{\mathcal{L}_1}$, or $\|y_2\|_{\mathcal{L}_\infty}\leq \|H\|_{\mathcal{L}_1}$.

Next we show that $\|H\|_{\mathcal{L}_1}$ is the least upper bound of $\|y_2\|_{\mathcal{L}_\infty}$ when $\|u_1\|_{\mathcal{L}_\infty}\leq 1$. This can be obtained by contradiction. Let $\|u_1\|_{\mathcal{L}_\infty}\leq 1$ and let $\|y_2\|_{\mathcal{L}_\infty}\leq \eta_y < \|H\|_{\mathcal{L}_1}$. This implies that

$$\sup_{t\geq 0}\|y_2(t)\|_\infty \leq \eta_y \leq \|H\|_{\mathcal{L}_1}.$$

Then there exist t_1 and t_2, $t_1 > t_2$, and index k such that

$$\sum_{j=1}^{m}\int_{t_2}^{t_1}|g_{kj}(t_1,\sigma)|\,d\sigma > \eta_y.$$

We can choose the control signal as

$$u_1(\sigma) = \left[\text{sign}\left(g_{k1}(t_1,\sigma)\right),\cdots,\text{sign}\left(g_{km}(t_1,\sigma)\right)\right]^T,\quad \sigma\in\left[t_2,\,t_1\right]^T,$$

and

$$u_1(\sigma) = 0 \text{ for } \sigma > t_1.$$

Notice that for this control signal $\|(u_1)_t\|_{\mathcal{L}_\infty}\leq 1$. Then we have

$$\begin{aligned}(y_2)_k(t_1) &= \sum_{j=1}^{m}\int_{t_2}^{t_1} g_{kj}(t_1,\sigma)(u_1)_j(\sigma)d\sigma\\ &= \textstyle\sum_{j=1}^{m}\int_{t_2}^{t_1}\left|g_{kj}(t_1,\sigma)\right|d\sigma > \eta_y.\end{aligned}$$

This implies $\sup_{t\geq 0}\|y_2(t)\|_\infty \geq \eta_y$, which contradicts the fact that η_y is an upper bound for $\|y_2\|_{\mathcal{L}_\infty}$ is the least upper bound for $\|y_2\|_{\mathcal{L}_\infty}$ for $\|u_1\|_{\mathcal{L}_\infty}\leq 1$. To complete the proof, in Equation (5.1) we consider $\|u_1\|_{\mathcal{L}_\infty}\leq 1$, which gives

$$\|y_2\|_{\mathcal{L}_\infty}\leq \|H_2\|_{\mathcal{L}_1}\|H_1\|_{\mathcal{L}_1}.$$

Since $\|H\|_{\mathcal{L}_1}$ is the least upper bound, the proof is complete. □

Theorem 5.14. (*[19], Theorem 5.6*) ($\mathcal{L}_1$ Small Gain Theorem) The interconnected system $w_2(t) = \Delta\big(w_1(t) - Mw_2(t)\big)$ with input $w_1(t)$ and output $w_2(t)$ is stable if $\|M\|_{\mathcal{L}_1}\|\Delta\|_{\mathcal{L}_1} < 1$.

For LTI systems, the result is similar.

The proof follows from the small gain Theorem 5.6 in [19].

5.1.4 Parameter Estimation

Definition 5.15. (*Projection Operator* [31]) Consider a convex compact set with a smooth boundary given by

$$\Omega_c \triangleq \{\theta \in \mathbb{R}^n | f(\theta) \leq c\}, \quad 0 \leq c \leq 1,$$

where $f : \mathbb{R}^n \to \mathbb{R}$ is the following smooth convex function

$$f(\theta) = \frac{\theta^T\theta - \theta_{max}^2}{\epsilon_\theta \theta_{max}^2}.$$

Here θ_{max} is the norm bound imposed on the parameter vector θ and ϵ_θ denotes the convergence tolerance of our choice. Let the true value of the parameter θ, denoted by θ^*, belong to Ω_0; i.e., $\theta^* \in \Omega_0$. The projection operator is defined as illustrated in Figure 5.1 and

$$\text{Proj}(\theta, y) \triangleq \begin{cases} y, & f(\theta) < 0, \\ y, & f(\theta) > 0 \text{ and } \nabla f^T y \leq 0, \\ y - \underbrace{\frac{\nabla f}{\|\nabla f\|}}_{\text{unit vector}} \underbrace{\left\langle \frac{\nabla f^T}{\|\nabla f\|}, y \right\rangle}_{\text{projection}} \underbrace{f(\theta)}_{\text{scaling}}, & f(\theta) > 0 \text{ and } \nabla f^T y > 0. \end{cases}$$

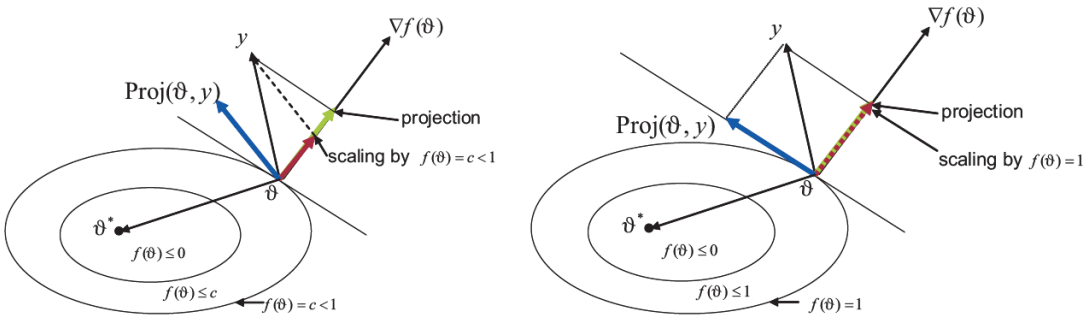

Figure 5.1: Illustration of the projection operator [31].

5.2 Problem Formulation

Consider the dynamic system (3.17)

$$\dot{\mathbf{x}}(t) = \mathbf{A}\mathbf{x}(t) + \mathbf{b}u(t), \quad u(t) = [\mathcal{H}(v)](t)$$
$$y(t) = \mathbf{C}^T\mathbf{x}(t)$$

where $\mathbf{x}$ is the system state vector. The matrix $\mathbf{A} = \begin{bmatrix} 0 & 1 \\ -k/m & -c/m \end{bmatrix}$ may be unknown or unstable. Moreover, the mass and stiffness terms could be slightly time-varying due to internal damping and heating that depends on the strain rate. Further we assume that there exists a known and stable matrix $\mathbf{A}_m = \begin{bmatrix} 0 & 1 \\ -a_1 & -a_2 \end{bmatrix} \in \mathbb{R}^{2\times 2}$ and a vector of ideal parameters $\theta \in \mathbb{R}^2$ such that $(\mathbf{A}_m, \mathbf{b})$ is controllable and $\mathbf{A} - \mathbf{A}_m = \mathbf{b}\,\theta^T$; i.e., $\theta = \begin{bmatrix} a_1 - k/m, & a_2 - c/m \end{bmatrix}^T$. We further assume that the (time-varying unknown) parameter vector θ belongs to a given compact convex set Θ. The signal $u(t) = [\mathcal{H}(v)](t)$ is the driving force generated by the hysteretic actuator $\mathcal{H}$ where $v(t)$ is the input field to the actuator $\mathcal{H}$.

Next we incorporate the approximate inverse of the homogenized energy model as the inverse compensator and use it before the actuator $\mathcal{H}$; as illustrated in Figure 2.5. The input $u(t)$ can be rewritten as

$$u(t) = [\mathcal{H}(v)](t) = [\mathcal{H}\widehat{\mathcal{H}}^{-1}(u_d)](t) \tag{5.2}$$

where the signal $u_d(t)$ is used as the input of the inverse compensator $\widehat{\mathcal{H}}^{-1}(\cdot)$ to generate the control field $v(t)$ which is then applied to the hysteretic device.

Substituting Equation (5.2) and the relation $\mathbf{A} - \mathbf{A}_m = \mathbf{b}\theta^T$ into Equation (5.1) yields

$$\begin{aligned} &\dot{\mathbf{x}}(t) = \mathbf{A}_m\mathbf{x}(t) + \mathbf{b}\big(u(t) + \theta^T\mathbf{x}(t)\big), \quad u(t) = [\mathcal{H}\widehat{\mathcal{H}}^{-1}(u_d)](t) \\ &y(t) = \mathbf{c}^T\mathbf{x}(t). \end{aligned} \tag{5.3}$$

Our objective is to design a low-frequency adaptive controller $u_d(t)$ such that $y(t)$ tracks a given bounded reference signal $r(t)$ while all other error signals remain bounded.

Note that such model-based inverse compensation is never exact due to the discretization or modeling errors, but the mismatch between inverse and hysteretic actuator can be designed to be small and thus be assumed bounded in magnitude; i.e.,

$$u(t) = u_d(t) + \sigma(t) \tag{5.4}$$

where $\sigma(t)$ is the inversion error which satisfies $|\sigma(t)| \le \Delta_0 \in \mathbb{R}$. Then we can model the inversion error as an external time-varying disturbance and attenuate its impact by $\mathcal{L}_1$ control techniques [7].

Assumption 5.1: We assume that parameter vector $\theta(t)$ and inversion error $\sigma(t)$ are continuously differentiable and their derivatives are uniformly bounded:

$$\|\dot{\theta}(t)\|_2 \leq d_\theta < \infty, \quad \|\dot{\sigma}(t)\|_2 \leq d_\sigma < \infty, \quad \forall t > 0$$

where the numbers d_θ, d_σ can be arbitrarily large.

The control objective is to design a full-state feedback controller such that $y(t)$ tracks a given bounded reference signal $r(t)$ both in transient and steady state, while all other error signals remain bounded.

5.3 $\mathcal{L}_1$ Adaptive Control Architecture

In this section, the elements of the $\mathcal{L}_1$ adaptive control architecture are summarized. This control architecture permits complete transient characterization for system state $x(t)$.

State Predictor: Consider the state predictor

$$\begin{aligned} \dot{\hat{\mathbf{x}}}(t) &= \mathbf{A}_m \hat{\mathbf{x}}(t) + \mathbf{b}(u_d(t) + \hat{\theta}^T \mathbf{x}(t) + \hat{\sigma}(t)), \\ \hat{y}(t) &= \mathbf{c}^T \hat{\mathbf{x}}(t) \end{aligned} \tag{5.5}$$

which has a similar structure as the system in Equation (5.3). The differences are: the unknown parameter vector $\theta(t)$ in Equation (5.3) is replaced by its adaptive estimate $\hat{\theta}(t)$; the driving force $u(t)$ is replaced by the Equation (5.4) with inversion error estimate $\hat{\sigma}(t)$, and parameters $\hat{\theta}^T$, $\hat{\sigma}(t)$ are governed by the following adaptation laws.

Adaptation Laws: Adaptive estimates

$$\begin{aligned} \dot{\hat{\theta}}(t) &= \Gamma_c \text{Proj}\left(\hat{\theta}(t), -\mathbf{x}(t)\tilde{\mathbf{x}}^T(t)Pb\right), & \hat{\theta}(0) &= 0 \\ \dot{\hat{\sigma}}(t) &= \Gamma_c \text{Proj}\left(\hat{\sigma}(t), -\tilde{\mathbf{x}}^T(t)Pb\right), & \hat{\sigma}(0) &= 0 \end{aligned} \tag{5.6}$$

are defined via the projection operator (Definition 5.15). Here $\tilde{\mathbf{x}}(t) = \hat{\mathbf{x}}(t) - \mathbf{x}(t)$ is the error between the states of the system and the predictor and P is the solution of the algebraic Lyapunov equation $\mathbf{A}_m^T P + P\mathbf{A}_m = -\mathbb{I}$. The existence of $P(t)$ follows from the proof of Lemma 5.4. In the implementation of the projection operator, we use the compact set Θ.

One advantage of the $\mathcal{L}_1$ control over the conventional MRAC is that $\mathcal{L}_1$ control allows for the incorporation of a low-pass filter into the feedback loop to generate control signal. A low-pass filter, by definition, is a filter that offers easy passage to low-frequency

signals and attenuates (reduces the amplitude of) high-frequency signals, more specifically, the frequencies higher than the cutoff frequency. The actual amount of attenuation for each frequency varies from filter to filter. These properties of low-pass filters offer a possibility to eliminate the inversion error and other external or internal disturbances faster and more efficiently. Then the $\mathcal{L}_1$ control signal is generated via a low-pass filter $C(s)$.

Control Law: The control signal $u_d(t)$ is generated through gain feedback of the system

$$\mathcal{X}(s) = D(s)\bar{r}(s), \quad u_d(s) = -k\mathcal{X}(s), \tag{5.7}$$

where $k \in \mathbb{R}^+$ is a feedback gain, $\bar{r}(s)$ is the Laplace transformation of

$$\bar{r}(t) = u_d(t) + \hat{\theta}^T\mathbf{x}(t) + \hat{\sigma}(t) - k_g r(t), \qquad k_g = -\frac{1}{\mathbf{c}^T\mathbf{A}_m^{-1}\mathbf{b}} \tag{5.8}$$

and $D(s)$ is a transfer function that leads to strictly proper stable system

$$C(s) = \frac{kD(s)}{1 + kD(s)} \tag{5.9}$$

with low-pass gain $C(0) = 1$.

Theorem 5.16. (*[8], $\mathcal{L}_1$-gain stability requirement*): Design $D(s)$ and k to satisfy

$$\|\overline{G}(s)\|_{\mathcal{L}_1} L < 1, \qquad L = \max_{\theta\in\Theta} \sum_{i=1}^{n} |\theta_i(t)| \tag{5.10}$$

where $\overline{G}(s) = H(s)\overline{C}(s) = (s\mathbb{I} - \mathbf{A}_m)^{-1}b(1 - C(s))$, with $H : \mathbb{R} \to \mathbb{R}^n$ being the input-output map of the dynamic system $\dot{x}(t) = A_m x(t) + bu(t)$ and $\overline{C}$ being the input-output map of the $\overline{C}(s) = 1 - C(s)$. Thus, $G : \mathbb{R} \to \mathbb{R}^n$.

The proof is similar to the stability requirement proof given in [7] and it follows from the small gain Theorem 5.14 ([19], Theorem 5.6), written for the $\mathcal{L}_1$ gain.

Proof: To establish the stability requirement in Equation (5.10), consider the reference companion system with its control signal

$$\begin{aligned} \dot{\mathbf{x}}_m(t) &= \mathbf{A}_m\mathbf{x}_m(t) + \mathbf{b}\left(u_d(t) + \theta^T\mathbf{x}_m(t) + \sigma(t)\right), \quad \mathbf{x}_m(0) = \mathbf{x}_0 \\ u_d(s) &= C(s)\left(k_g r(s) - \theta^T\mathbf{x}(s) - \sigma(s)\right). \end{aligned} \tag{5.11}$$

Letting $H(s) = (s\mathbb{I} - A_m)^{-1}b$, it follows from Equation (5.11) that

$$\begin{aligned} \mathbf{x}_m(s) &= H(s)\big(C(s)(k_g r(s) - r_1(s)) + r_1(s)\big) + (s\mathbb{I} - \mathbf{A}_m)^{-1}\mathbf{x}_0 \\ &= H(s)C(s)k_g r(s) + H(s)(1 - C(s))r_1(s) + (s\mathbb{I} - \mathbf{A}_m)^{-1}\mathbf{x}_0 \end{aligned} \tag{5.12}$$

where $r_1(s)$ is the Laplace transformation of $r_1(t) = \theta^T \mathbf{x}_m(t) + \sigma(t)$.

Letting $\overline{G}(s) = H(s)\big(1 - C(s)\big)$ and using Corollary 5.10, we arrive at the upper bound

$$\|\mathbf{x}_m\|_{\mathcal{L}_\infty} \leq \|k_g C(s)H(s)\|_{\mathcal{L}_1}\|r\|_{\mathcal{L}_\infty} + \|\overline{G}(s)\|_{\mathcal{L}_1}\|r_1\|_{\mathcal{L}_\infty} + \|(s\mathbb{I} - \mathbf{A}_m)^{-1}\mathbf{x}_0\|_{\mathcal{L}_\infty}. \tag{5.13}$$

Since $\|\mathbf{x}_m(0)\|_\infty = \|\mathbf{x}_0\|_\infty < \rho_0$ and $r_1(s)$ is subject to the following $\mathcal{L}_\infty$ bound

$$\|r_1\|_{\mathcal{L}_\infty} \leq \|\theta\|_{\mathcal{L}_1}\|\mathbf{x}_m\|_{\mathcal{L}_\infty} + \|\sigma\|_{\mathcal{L}_\infty} = L\|\mathbf{x}_m\|_{\mathcal{L}_\infty} + \|\sigma\|_{\mathcal{L}_\infty} \tag{5.14}$$

where $L = \max_{\theta\in\Theta} \sum_{i=1}^{n} |\theta_i(t)|$, we then have

$$\begin{aligned} \|\ \mathbf{x}_m\|_{\mathcal{L}_\infty} \leq\ & \|\overline{G}(s)\|_{\mathcal{L}_1} L\|\mathbf{x}_m\|_{\mathcal{L}_\infty} + \|\overline{G}(s)\|_{\mathcal{L}_1}\|\sigma\|_{\mathcal{L}_\infty} \\ & + \|k_g C(s)H(s)\|_{\mathcal{L}_1}\|r\|_{\mathcal{L}_\infty} + \|(s\mathbb{I} - \mathbf{A}_m)^{-1}\mathbf{x}_0\|_{\mathcal{L}_\infty}. \end{aligned}$$

Theorem 5.14 then ensures that the closed-loop system in Equation (5.11) is stable if Equation (5.10) is satisfied; i.e.,

$$\|\overline{G}(s)\|_{\mathcal{L}_1} L < 1, \qquad G(s) = (s\mathbb{I} - \mathbf{A}_m)^{-1} b(1 - C(s)). \qquad \square$$

In the case of constant $\theta(t)$ and a first order low-pass filter $C(s) = \dfrac{k}{s+k}$, the stability requirement can be simplified to stabilize the companion system

$$\begin{aligned} \dot{\hat{x}}(t) &= \mathbf{A}_m \hat{x}(t) + b\left(u_d(t) + \hat{\sigma}(t) + \hat{\theta}^T(t)x\right) \\ \dot{u}_d(t) &= -k u_d(t) + k\Big(k_g r(t) - \hat{\theta}^T(t)x(t) - \hat{\sigma}(t)\Big) \end{aligned}$$

which is reduced to the stability requirement that

$$A_g = \begin{bmatrix} \mathbf{A}_m + \mathbf{b}\,\theta^T & \mathbf{b} \\ -k\theta^T & -k \end{bmatrix}$$

is Hurwitz for all $\theta \in \Theta$.

The close-loop system with it is illustrated in Figure 5.2.

5.4 Analysis of the $\mathcal{L}_1$ Adaptive Control Architecture

5.4.1 Stability of Closed-loop Reference System

Consider the following ideal version of the adaptive controller in Equation (5.7)-(5.9)

$$u_{ref}(s) = C(s)(k_g r(s) - \theta^T x_{ref}(s) - \sigma(s)). \tag{5.15}$$

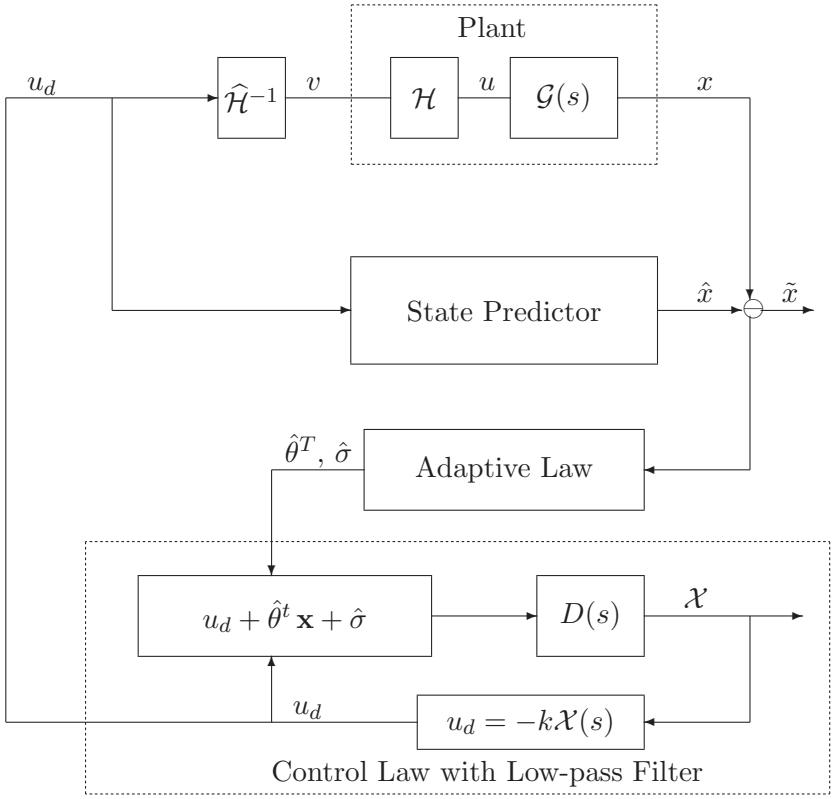

Figure 5.2: Closed-loop system with the $\mathcal{L}_1$ adaptive control architecture.

The control law in Equation (5.15) yields the closed-loop dynamics

$$\dot{x}_{ref(s)} = A_m x_{ref}(t) + b(u_{ref}(t) + \theta^T(t)x_{ref}(t) + \sigma(t)), \quad x_{ref}(0) = 0. \tag{5.16}$$

Lemma 5.17. *([7], Lemma 5)* If the $D(s)$ satisfies the condition in Theorem 5.16, the reference system in (5.15)-(5.16) is stable.

The proof is similar to the proof of Lemma 5 given in [7].

Proof: Let $C : \mathbb{R} \to \mathbb{R}$ be the input-output map of the transfer function $C(s)$, and let the map $H_{in} : \mathbb{R}^n \to \mathbb{R}^n$ represent the zero-input response of the linear system $\dot{x}(t) = A_m x(t)$. It follows from (5.15)-(5.16) that $x_{ref} = \overline{G}r_1 + HCk_g r + H_{in}x_0$, where $r_1(t) = \theta^T(t)x_{ref}(t) + \sigma(t)$ is subject to the bound $\|r_1\|_{\mathcal{L}_\infty} \leq L\|x_{ref}\|_{\mathcal{L}_\infty} + \|\sigma\|_{\mathcal{L}_\infty}$. We can consider $\overline{G}$ and θ^T as the two interconnected systems defined in Theorem 5.14. The block diagram is shown in Figure 5.3. Since $D(s)$ satisfies the condition in Theorem 5.16 and the

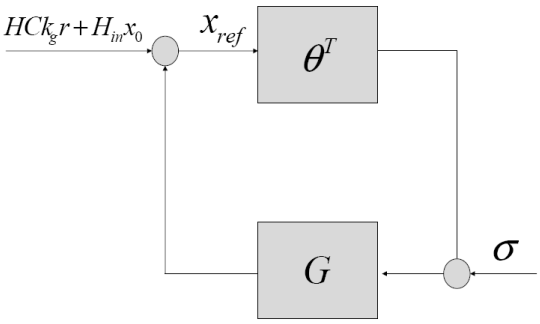

Figure 5.3: Block diagram of the closed-loop reference system.

inversion error $\sigma(t)$ and signals $HCk_g r$ and $H_{in}x_0$ are bounded, Theorem 5.14 guarantees that the closed-loop system in (5.15)-(5.16) is stable. □

Note that when $C(s) = 1$, u_{ref} reduces to the ideal control signal

$$u_{id}(t) = k_g r(t) - \theta^T \mathbf{x}_{id} - \sigma(t) \tag{5.17}$$

and u_{id} leads the closed-loop reference system (5.16) to the reference model of MRAC

$$\dot{\mathbf{x}}_{id}(t) = \mathbf{A}_m \mathbf{x}_{id}(t) + \mathbf{b} k_g r(t) \tag{5.18}$$

by canceling the uncertainties exactly. In the closed-loop predictor system defined by Equations $(5.5) - (5.7)$, $u_{id}(t)$ is further low-pass filtered by $C(s)$ in Equation (5.9) to guarantee low-frequency range. Thus, the system defined by Equations $(5.5) - (5.7)$ has a different response as compared to ideal reference system (5.18) achieved with (5.17). It has been proven in [7] that the response of the state predictor Equation (5.6) can be made as close as possible to the response of the ideal system Equation (5.18) by reducing $\|\overline{G}(s)\|_{\mathcal{L}_1}$ arbitrarily small, and $\|\overline{G}(s)\|_{\mathcal{L}_1}$ can be made arbitrarily small by appropriately choosing the design constants, further details may be found in [7] and [8].

5.4.2 Steady State Performance

Theorem 5.18. *([7], Lemma 6)* Given the system in Equation (5.1) and the $\mathcal{L}_1$ adaptive controller defined via Equations (5.5)-(5.7) subject to Equation (5.10), the prediction error between the system state and the predicor is bounded.

The proof is similar to the proof of Lemma 6 given in [7].

Proof: Consider the candidate Lyapunov function

$$V\big(\tilde{x}(t), \tilde{\theta}(t), \tilde{\sigma}(t)\big) = \tilde{x}^T(t) P(t) \tilde{x}(t) + \Gamma_c^{-1} \tilde{\theta}^T(t) \tilde{\theta}(t) + \Gamma_c^{-1} \sigma^2(t) \tag{5.18}$$

where $\tilde{\theta}(t) = \hat{\theta}(t) - \theta(t)$, $\tilde{\sigma}(t) = \hat{\sigma}(t) - \sigma(t)$.

The projection algorithm (5.6) ensures that $\hat{\theta} \in \Theta$, $|\hat{\sigma}(t)| < \Delta_0$ for all $t \geq 0$, and therefore

$$\max_{t\geq 0}\left(\Gamma_c^{-1}\tilde{\theta}(t)\tilde{\theta}(t) + \Gamma_c^{-1}\tilde{\sigma}^2(t)\right) \leq \frac{1}{\Gamma_c}\left(\max_{\theta\in\Theta}\sum_{i=1}^{n} 4\theta_i^2 + 4\Delta_0^2\right) \tag{5.19}$$

for any $t \geq 0$.

Prediction error dynamics can be derived from Equations (5.3)-(5.5) yielding

$$\dot{\tilde{x}}(t) = A_m\tilde{x}(t) + b\left(u(t) + \tilde{\theta}(t)x(t) + \tilde{\sigma}(t)\right), \quad \tilde{x}(0) = 0.$$

Using the projection-based adaptation laws in Equation (5.6), one has the upper bound of the Lyapunov candidate derivative

$$\begin{aligned}
\dot{V}(t) &= \dot{\tilde{x}}^T(t)P(t)\tilde{x}(t) + \tilde{x}^T(t)P(t)\dot{\tilde{x}}(t) + \tilde{x}^T(t)\dot{P}(t)\tilde{x}(t) \\
&\quad +2\Gamma_c^{-1}\theta^T(t)\dot{\tilde{\theta}}(t) + 2\Gamma_c^{-1}\tilde{\sigma}^T\dot{\tilde{\sigma}}(t) \\
&= -\tilde{x}^T(t)\left(\mathbb{I} - \dot{P}(t)\right)\tilde{x}(t) - 2\Gamma_c^{-1}\theta^T(t)\dot{\theta}(t) - 2\Gamma_c^{-1}\tilde{\sigma}^T\dot{\sigma}(t) \\
&\leq -\tilde{x}^T(t)\left(\mathbb{I} - \dot{P}(t)\right)\tilde{x}(t) + 2\Gamma_c^{-1}\left|\tilde{\theta}^T(t)\dot{\theta}(t) + \tilde{\sigma}(t)\dot{\sigma}(t)\right|.
\end{aligned} \tag{5.20}$$

The upper bounds for θ and σ along with the projection based adaptive laws lead to the upper bound

$$\left|\tilde{\theta}^T(t)\dot{\theta}(t) + \tilde{\sigma}(t)\dot{\sigma}(t)\right| \leq 2\max_{\theta\in\Theta}\|\theta\|_\infty d_\theta + d_\sigma\Delta. \tag{5.21}$$

Define the constant

$$\theta_{max} = \max_{\theta\in\Theta}\sum_{i=1}^{n} 4\theta_i^2 + 4\Delta_0^2 + 4\frac{\lambda_{P_{max}}}{1-\epsilon_P}\left(d_{\sigma\Delta} + \max_{\theta\in\Theta}\|\theta\|_\infty d_\theta\right)$$

with $\lambda_{P_{max}} = \max\limits_{t\in[0,\infty)}\lambda_{max}\big(P(t)\big)$.

If $V(t) \geq \theta_m/\Gamma_c$ at some t, it then follows from Equation (5.19) that

$$\tilde{x}^T(t)P(t)\tilde{x}(t) \geq 4\frac{\lambda_{P_{max}}}{\Gamma_c(1-\epsilon_P)}\left(d_{\sigma\Delta} + \max_{\theta\in\Theta}\|\theta\|_\infty d_\theta\right).$$

Hence

$$\tilde{x}(t)\left(\mathbb{I} - \dot{P}(t)\right)\tilde{x}(t) \geq \frac{1-\epsilon_P}{\lambda_{P_{max}}}\tilde{x}^T(t)P(t)\tilde{x}(t) \geq \frac{4}{\Gamma_c}\left(\max_{\theta\in\Theta}\|\theta\|_\infty d_\theta + d_\sigma\Delta\right). \tag{5.22}$$

Hence if $V(t) \geq \theta_{max}/\Gamma_c$, it follows from Equations (5.21) and (5.22) that

$$\dot{V}(t) \leq 0, \qquad \text{for all } t \geq t_m. \tag{5.23}$$

Since we have set $\hat{x}(0) = x(0)$, then we can verify that

$$V(0) \leq \Gamma_c^{-1}\tilde{\theta}(t)\tilde{\theta}(t) + \Gamma_c^{-1}\tilde{\sigma}^2(t) \leq \Gamma_c^{-1}\left(\max_{\theta\in\Theta}\sum_{i=1}^{n} 4\theta_i^2 + 4\Delta^2\right) < \theta_{max}/\Gamma_c.$$

It follows from (5.23) that $V(t) \leq \theta_{max}/\Gamma_c$ for any $t \geq 0$. Since $\lambda_{P_{min}}\|\tilde{x}(t)\|_{\mathcal{L}_\infty}^2 \leq \tilde{x}^T(t)P(t)\tilde{x}(t) \leq V(t)$, we then have the prediction error

$$\|\tilde{x}(t)\|_{\mathcal{L}_\infty}^2 \leq \frac{\theta_{max}}{\lambda_{P_{min}}} \leq \frac{\theta_{max}}{\lambda_{P_{min}}\Gamma_c} \tag{5.24}$$

which concludes the proof. Notice that this bound is proportional to the rate of variation of uncertainties and is inverse proportional to the adaptation gain. □

Furthermore, we can show that the prediction error $\tilde{x}(t)$ converges to zero asymptotically; i.e., $\lim_{t\to\infty}\tilde{x}(t) = 0$.

Using the triangle relationship for norms, we can get

$$\left|\, \|\hat{\mathbf{x}}(t)\|_{\mathcal{L}_\infty} - \|\mathbf{x}(t)\|_{\mathcal{L}_\infty} \right| \leq \sqrt{\frac{V(0)}{\lambda_{min}(P)}}. \tag{5.25}$$

The projection technique in Equation (5.6) ensures that $\hat{\theta}(t) \in \Theta$, for all $t \geq 0$ and $|\hat{\sigma}(t)| \leq \Delta_0$. Applying Corollary 5.10 to the predictor system Equation (5.6) yields

$$\|\hat{\mathbf{x}}(t)\|_{\mathcal{L}_\infty} \leq \|\overline{G}(s)\|_{\mathcal{L}_1}L\|\hat{\mathbf{x}}(t)\|_{\mathcal{L}_\infty} + \|\overline{G}(s)\|_{\mathcal{L}_1}\|\sigma\|_{\mathcal{L}_\infty} + \|k_gC(s)H(s)\|_{\mathcal{L}_1}\|r\|_{\mathcal{L}_\infty}.$$

Let $\lambda = \|\overline{G}(s)\|_{\mathcal{L}_1}L$. From the stability requirement, we know that $\lambda < 1$, so the relationship in Equation (5.25) can be rewritten as

$$\|\hat{\mathbf{x}}(t)\|_{\mathcal{L}_\infty} \leq \frac{1}{1-\lambda}\left(\lambda\sqrt{\frac{V(0)}{\lambda_{min}(P)}} + \|\overline{G}(s)\|_{\mathcal{L}_1}\Delta_0 + \|k_gC(s)H(s)\|_{\mathcal{L}_1}\|r\|_{\mathcal{L}_\infty}\right). \tag{5.26}$$

Since $V(0)$, $\lambda_{min}(P)$, $\|\overline{G}(s)\|_{\mathcal{L}_1}$, $\|k_gC(s)H(s)\|_{\mathcal{L}_1}$ and $\|r(t)\|_{\mathcal{L}_\infty}$ are all finite and $\lambda < 1$, the relationship in Equation (5.26) implies that $\|\hat{\mathbf{x}}(t)\|_{\mathcal{L}_\infty}$ is finite for any $t > 0$ and hence $\hat{\mathbf{x}}(t)$ is bounded. The adaptation law in (5.6) ensures that the estimates $\hat{\theta}(t)$ and $\hat{\sigma}(t)$ are also bounded, it can be checked easily that $\dot{\tilde{x}}(t)$ is bounded, and it follows from Barbalat's lemma [38] that $\lim_{t\to\infty}\tilde{x}(t) = 0$.

Theorem 5.19. *([7], Theorem 2)* Given the system in Equation (5.1) and the $\mathcal{L}_1$ adaptive controller defined via Equations (5.5)-(5.7) subject to Equation (5.10), we have

$$\|x - x_{ref}\|_{\mathcal{L}_\infty} \leq \gamma, \qquad \text{where } \gamma = \frac{\|C\|_{\mathcal{L}_1}}{1 - \|HC\|_{\mathcal{L}_1}L}\sqrt{\frac{\theta_m}{\lambda_{P_{min}}\Gamma_c}}.$$

The proof is similar to the proof of Theorem 2 given in [7].

Proof: Let

$$\tilde{r}_2(t) = \tilde{\theta}^T(t)x(t) + \tilde{\sigma}(t), \quad r_2(t) = \theta^T(t)x(t) + \sigma(t).$$

It follows from (5.6) that $\chi(x) = D(s)r_u(s)$ where

$$r_u(t) = u_d(t) + r_2(t) + \tilde{r}_2(t) - k_g r(t).$$

Consequently

$$\chi(s) = \frac{D(s)}{1 + kD(s)} r_3(s), \quad u_d(s) = -\frac{kD(s)}{1 + kD(s)} r_3(s),$$

where $r_3(t) = r_2(t) - k_g(t)r(t) + \tilde{r}(t)$. Using the definition of $C(s)$ from Equation (5.9), we can write

$$u_d(s) = -C(s)r_3(s) \tag{5.27}$$

and the physical system consequently takes the form

$$x = H\overline{C}r_2 + HCk_g r - HC\tilde{r}_2 \tag{5.28}$$

where $H : \mathbb{R} \to \mathbb{R}^n$ is the input-output map of the linear time varying system $\dot{x}(t) = A_m(t)x(t) + bu(t)$, and $\overline{C}$ is the input-output map of $\overline{C}(s) = 1 - C(s)$.

It follows from Equations (5.17) and (5.18) that

$$x_{ref} = H\overline{C}r_1 + HCk_g r, \quad r_1(t) = \theta^T(t)x_{ref}(t) + \sigma(t).$$

Let $e(t) = x(t) - x_{ref}(t)$. Using (19) one gets

$$e = H\overline{C}r_4 - HC\tilde{r}_2, \quad e(0) = 0 \tag{5.29}$$

where

$$r_4(t) = \theta^T(t)e(t). \tag{5.30}$$

We thus get the upper bound

$$\|e\|_{\mathcal{L}_\infty} \leq \|H\overline{C}\|_{\mathcal{L}_1}\|r_4\|_{\mathcal{L}_\infty} + \|CH\tilde{r}_2\|_{\mathcal{L}_\infty}. \tag{5.31}$$

Using the definition of L in Equation (5.10), it is straight forward to verify that

$$\|\theta^T e\|_{\mathcal{L}_\infty} \leq L\|e\|_{\mathcal{L}_\infty}.$$

Moreover, from (5.30) we have that $\|r_4\|_{\mathcal{L}_\infty} \leq L\|e\|_{\mathcal{L}_\infty}$. From (5.31) it follows that

$$\|e\|_{\mathcal{L}_\infty} \leq \|H\overline{C}\|_{\mathcal{L}_1}\|e\|_{\mathcal{L}_\infty} + \|C\|_{\mathcal{L}_1}\|\tilde{x}\|_{\mathcal{L}_\infty}.$$

The upper bound for $\tilde{x}$ from (5.24) and the $\mathcal{L}_1$-norm upper bound from (5.10) lead to the following upper bound

$$\|e\|_{\mathcal{L}_\infty} \leq \frac{\|C\|_{\mathcal{L}_1}}{1 - \|HC\|_{\mathcal{L}_1}L}\sqrt{\frac{\theta_m}{\lambda_{P_{max}}\Gamma_c}}$$

for e, which holds uniformly for all $t \geq 0$ and therefore leads to

$$\|x - x_{ref}\|_{\mathcal{L}_\infty} \leq \gamma, \quad \gamma = \frac{\|C\|_{\mathcal{L}_1}}{1 - \|HC\|_{\mathcal{L}_1}L}\sqrt{\frac{\theta_m}{\lambda_{P_{min}}\Gamma_c}}.$$

Thus, the tracking error between $x(t)$ and $x_{ref}(t)$ is uniformly bounded by a constant inverse proportional to Γ_c. This implies that one can arbitrarily close tracking performance by uniformly increasing the adaptation gain Γ_c. □

5.5 Simulation Results

5.5.1 Tracking Using a 1st Order Low-pass Filter

We first consider using a first order low-pass filter to generate control signal. Consider the dynamic system in (5.3) with

$$A = \begin{bmatrix} 0 & 1 \\ 5 & 7 \end{bmatrix}, b = \begin{bmatrix} 0 \\ 1 \end{bmatrix}, c = \begin{bmatrix} 1 \\ 0 \end{bmatrix}$$

and the state predictor in (5.5) with

$$A_m = \begin{bmatrix} 0 & 1 \\ -5 & -3 \end{bmatrix}, \qquad \theta = \begin{bmatrix} 10 \\ 10 \end{bmatrix}.$$

We note that matrix A has poles in the right half plane and hence it is an unstable non-minimum phase system. While the unstable system does not illustrate the physical AFM dynamics, we use it to demonstrate the effectiveness of the proposed $\mathcal{L}_1$ inverse control structure on a worst-case scenario. The constant θ is assumed to be unknown and the compact set can be conservatively chosen as $\Omega = \{\theta_1 \in [0, 20], \theta_2 \in [0, 20]\}$. The

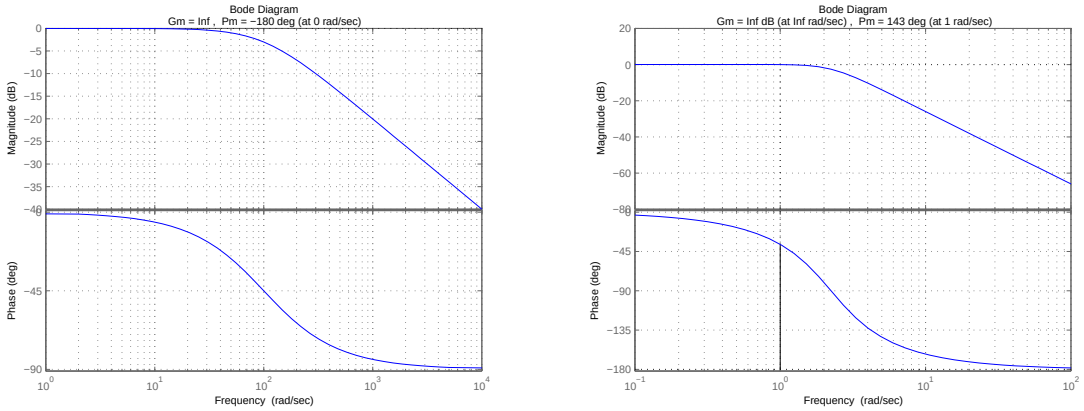

(a) (b)

Figure 5.4: Bode diagram; (a) Low-pass filter, (b) the reference model.

control objective is to design an adaptive controller $u_d(t)$ to ensure that $x_1(t)$ tracks any reference signal $r(t)$ both in transient and steady state.

To implement the $\mathcal{L}_1$ adaptive control architecture (5.5), (5.6), (5.7), we need to verify the simplified version of $\mathcal{L}_1$ stability requirement in (5.10). For constant $\theta = \begin{bmatrix} 10 & 10 \end{bmatrix}^T$, we have

$$A_g = \begin{bmatrix} A_m + b\theta^T & b \\ -k\theta^T & -k \end{bmatrix} = \begin{bmatrix} 0 & 1 & 0 \\ 5 & 7 & 1 \\ -10k & -10k & -k \end{bmatrix}. \tag{5.32}$$

Note that for $k > 50$, the matrix A_g is Hurwitz. We set $k = 100$ which means that the transfer function for the low-pass filter takes the form

$$G_{fil}(s) = \frac{100}{s + 100} = \frac{1}{\frac{s}{\omega_0} + 1}, \quad \omega_0 = 100. \tag{5.33}$$

Figure 5.4(a) illustrates the bode plot for the transfer function (5.33).

The bode magnitude plot tells us that at the break frequency, $\omega = \omega_0 = 10^2$ rad/sec, the gain is about 3.01 dB and the phase is $-\frac{\pi}{4}$ degree. At lower frequencies, $\omega \ll \omega_0$, the gain is approximatly zero, and at higher frequencies, $\omega \gg \omega_0$, the gain increases at 20 dB/decades and goes through the break frequency at 0 dB; that is, for every factor of 10 increase in frequency, the magnitude drops by 20 dB. We can thus say that the low-pass filter (5.33) can pass all signals with frequencies lower than the break frequency

10^2 rad/sec and attenuates (reduces the amplitude of) signals with frequencies higher than 10^2 rad/sec (Note that 1 Hz=2π rad/sec).

Similarly, we can write the transfer function of the reference model (5.16) as

$$G_{ref}(s) = \frac{5}{s^2+3s+5} = \frac{1}{\left(\frac{s}{\omega_0}\right)^2 + 2\zeta\left(\frac{s}{\omega_0}\right) + 1}, \quad \omega_0 = \sqrt{5},\ \zeta = h\frac{3}{2\sqrt{5}}. \tag{5.34}$$

Figure 5.4(b) illustrates the bode plot for the transfer function Equation (5.34).

We note from the bode magnitude plot that at frequencies higher than the break frequency, $\omega_0 = \sqrt{5}$ rad/sec, the gain increases at 40 dB/decades and goes through the break frequency at 0 dB; that is, for every factor of 10 increase in frequency, the magnitude drops by 40 dB. At lower frequencies, $\omega \ll \omega_0$, the gain is approximately zero and a peak occurs in the magnitude plot near the break frequency ω_0. The peak has a magnitude of

$$|G_{ref}(j\omega_r)| = -20\lg(2\zeta\sqrt{1-\zeta^2}) = 0.004 \text{ dB} \sim 0$$

where $\omega_r = \omega_0\sqrt{1-2\zeta^2} = 0.7$.

To solve the ODE system (5.5) – (5.7), we consider two techniques: use of the MATLAB routine ode15s and an implicit Euler technique.

Matlab Routine: ODE15s

For all the simulation results included in this section, we explore the case where the hysteresis inverse model is discretized on a coarse mesh and integrated using an relatively inexact integration rule. More specifically, both the coercive field E_c and interaction field E_I are discretized into 4 intervals, and 2-point Gauss quadrature rule is applied to approximate the inverse model. The inversion error bound of this discretization is about 0.01.

We first consider a simple single-frequency sinusoidal function $r(t) = \cos(t)$. The frequency of $r(t)$ is $1/2\pi$ Hz (= 1 rad/sec). Based on the previous analysis, this $r(t)$ could pass the filter and reference model unchanged. Theoretically, the tracking output $x_1(t)$ should exactly match the shape of $r(t) = \cos(t)$ after $x_1(t)$ converges.

Simulation results for reference input $r(t) = \cos(t)$ are shown in Figure 5.5(a). We note that the system output $x_1(t)$ converges to $r(t)$ asymptotically whereas $x_1(t)$ lags behind the reference signal $r(t)$ with a delay time of about $t_0 = 0.62$ sec. The time history of control signal and the inversion error is plotted in Figure 5.5(b). The generated control signal $u_d(t)$

is well bounded and hysteresis inversion error is $|\sigma(t)| = |\,u(t) - u_d(t)| \leq 6.3716e-002$. The generated control signal $u_d(t)$ exactly compensates for the inversion error and leads the system state to the desired response.

To cancel the delay problem, we can redefine $r(t)$ by $r(t+t_0)$, so it requires that we should have an exact prediction of the time-delay t_0 in advance. The performance for $r(t) = \cos(t)$ with time compensation is shown in Figure 5.7, and we can see that the $x_1(t)$ could exactly track the reference signal $r(t)$ if we have a good prediction of the time delay.

Next, we consider a multi-frequency sinusoidal reference signal $r(t) = 2\cos(t) + 10\cos(\pi t/5)$. We keep the same values for all other parameters. This multi-frequency $r(t)$ could also pass the filter and reference model unchanged. The simulation result shown in Figure 5.8(a) illustrates that the time-delay is independent of the frequencies of the reference signal $r(t)$; it only depends on the model and controller (low-pass filter) we choose. A rigorous relationship between the model and time-delay has not been derived. The performance for $r(t) = 2\cos(t) + 10\cos(\pi t/5)$ with time compensation is shown in Figure 5.8(b).

We additionally consider two typical trajectories common to nanopositioning and industrial applications. Simulation results for the trajectories $r_1(t)$ and $r_2(t)$ are plotted respectively in Figure 5.9. The results Figure 5.10 and Figure 5.11 illustrate that the $\mathcal{L}_1$ control design employing homogenized energy model based inverse filters can maintain a tracking accuracy once prediction tracking commences even though the transducer is operating in the hysteretic and nonlinear regime.

To compare with the modified MRAC method described in Chapter 4, we apply the $\mathcal{L}_1$ control method to the system dynamics (4.17) for a similar reference signal shown in Figure 4.3(a), the $\mathcal{L}_1$ tracking results are shown in Figure 5.17. We observe that $\mathcal{L}_1$ control can provide much faster tracking than MRAC, also the generated control signal is well bounded and modest in size.

Implicit Euler Method

Secondly we apply the implicit Euler method to solve the ODE system (5.5)−(5.7). Using the implicit Euler method, we aim to see if it changes the time delay problem. The simulation results for reference input $r = \cos(t)$ are shown in Figure 5.12. We can see that neither tracking performance nor time delay is significantly improved compared to the results obtained by ODE15s (see Figure 5.5-5.7). Next, we apply the implicit Euler method

to the same multi-frequency reference signal that we used before; i.e., $r(t) = 2\cos(t) + 10\cos(\pi t/5)$. We note that the results, shown in Figure 5.13, are quite similar to the results we got by using ode15s. We then can conclude that the implicit Euler method doesn't improve much on either the tracking performance or dynamic lag problem. However, it is significantly more efficient to implement.

5.5.2 2nd Order Low-pass Filter Tracking

In some cases, we also require high speed tracking. For example, the physical milling device using Terfenol-D as the actuator is designed to operate at 3000 rpm while maintaining tracking tolerances of $1 - 2\mu$m. A typical high frequency trajectory common to this type of industrial applications is plotted in Figure 5.15.

Consider the dynamic system (5.3) with

$$\mathbf{A} = \begin{bmatrix} 0 & 1 \\ 5 & 7 \end{bmatrix}, b = \begin{bmatrix} 0 \\ 1 \end{bmatrix}, c = \begin{bmatrix} 1 \\ 0 \end{bmatrix}$$

and the state predictor in (5.5) with

$$\mathbf{A}_m = \begin{bmatrix} 0 & 1 \\ -10 & -10 \end{bmatrix}, \qquad \theta = \begin{bmatrix} 15 \\ 17 \end{bmatrix}.$$

The constant θ is assumed to be unknown and the compact set can be conservatively chosen as $\Omega = \{\theta_1 \in [0, 25], \theta_2 \in [0, 25]\}$. For implementation of the $\mathcal{L}_1$ adaptive control structure, (5.5), (5.6), (5.7), we need to verify the $\mathcal{L}_1$ stability requirement in (5.10). Considering the low-pass filter $C(s) = \dfrac{3k^2 s + k^3}{(s+k)^3}$, we have

$$\overline{G}(s) = H(s)\big(1 - C(s)\big) = \left(1 - \frac{3k^2 s + k^3}{(s+k)^3}\right) H(s),$$

where $H(s) = (s\mathbb{I} - \mathbf{A}_m)^{-1}\mathbf{b} = \begin{bmatrix} \dfrac{1}{s^2 + 10s + 10} & \dfrac{s}{s^2 + 10s + 10} \end{bmatrix}$.

We choose the conservative value of $L = 50$. It can be verified numerically that $\|\overline{G}(s)\|_{\mathcal{L}_1} = 0.0191$ so that $\|\overline{G}(s)\|_{\mathcal{L}_1} L = 0.0191 \cdot 50 = 0.957 < 1$. Hence, the $\mathcal{L}_1$ stability requirement in (5.10) holds.

The frequency of the reference signal $r(t)$ is about 70π Hz so it could pass the filter and reference model unchanged. Theoretically, the tracking output $x_1(t)$ should exactly

match the shape of reference signal after $x_1(t)$ converges. Simulation results are shown in Figure 5.16(a). We note that the system output $x_1(t)$ converges to $r(t)$ asymptotically whereas $x_1(t)$ lags behind the reference signal $r(t)$ with a delay time of about $t_0 = 2 \times 10^{-3} s$. The system output $x_1(t)$ and predictor output $\hat{x}_1(t)$ are almost the same. To cancel the delay, we could redefine $r(t)$ by $r(t + t_0)$, so it requires that we should have an exact prediction of the time-delay t_0 in advance. The performance with time compensation is shown in Figure 5.16(b), and it illustrates that the pre-specified tolerance of $1 - 2\mu m$ is achieved in the presence of disturbances and inversion errors.

5.6 Concluding Remarks

In this chapter, we presented adaptive control designs that incorporate external disturbances to the system due to unattenuated hysteretic behavior and actuator noise in the control design. To accommodate the disturbances, $\mathcal{L}_1$ control design is utilized. Two crucial components of the control design involve the construction of a companion system which predicts the output of physical smart material system and the incorporation of a low-pass filter which eliminates or attenuates unmodeled hysteresis, actuator noise and disturbances. For the numerical examples considered in this chapter, the choice of appropriate low-pass filters had more impact on the final tracking authority than did the specification of $\mathcal{L}_1$ control designs. It was shown that the controller designs utilizing an inverse compensator based on the homogenized energy model of hysteresis Equation (2.9) were able to achieve accurate tracking while rejecting the disturbances due to actuator noise and the inherent hysteresis. A disadvantage of this $\mathcal{L}_1$ control design is the tracking time delay due to the low-pass filter. To improve the controller's performance, rigorous relation between the delay time and control structure must be deduced.

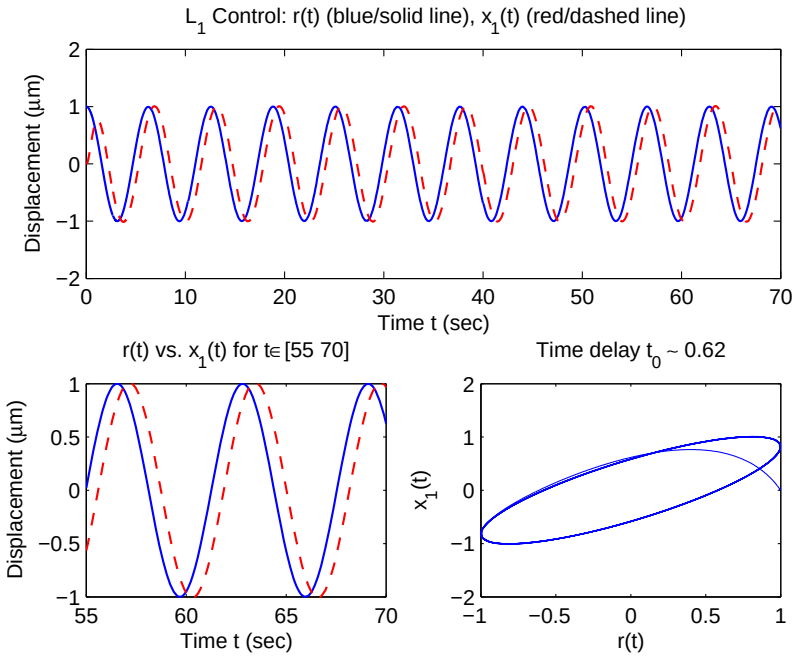

(a)

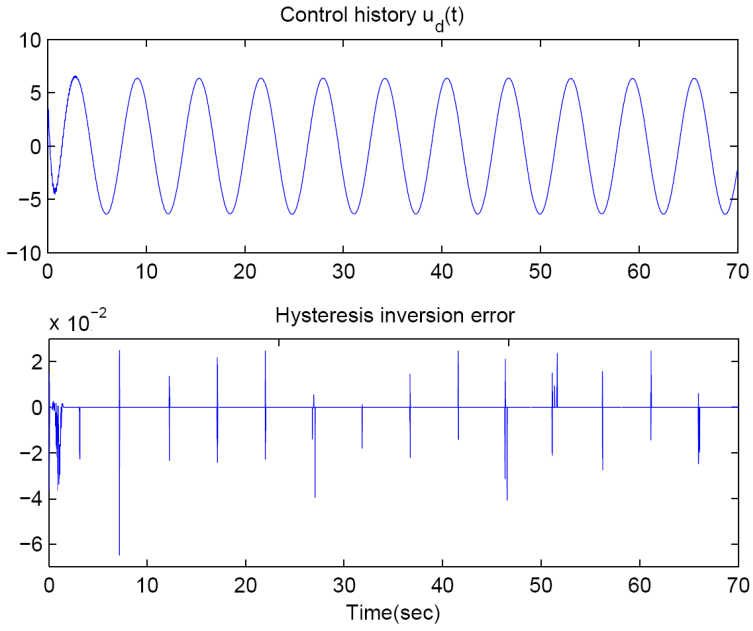

(b)

Figure 5.5: Performance of $\mathcal{L}_1$ adaptive controller for reference input $r = \cos(t)$: (a) displacement tracking and error, and (b) generated control signal and hysteresis inversion error.

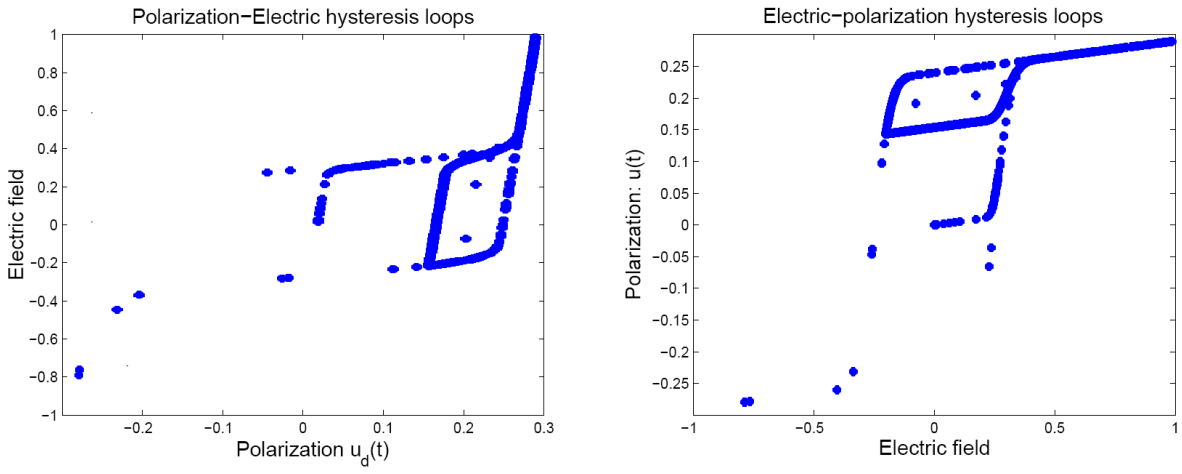

(a) (b)

Figure 5.6: (a) Generated inverse compensation loop, and (b) hysteresis loop.

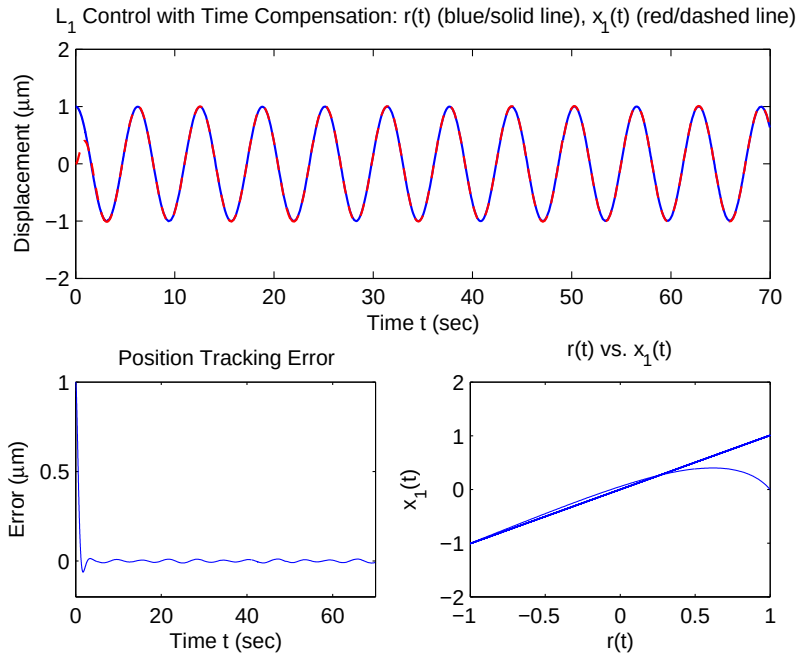

Figure 5.7: Performance of $\mathcal{L}_1$ adaptive controller for reference input $r = \cos(t)$ using ODE15s with time compensation.

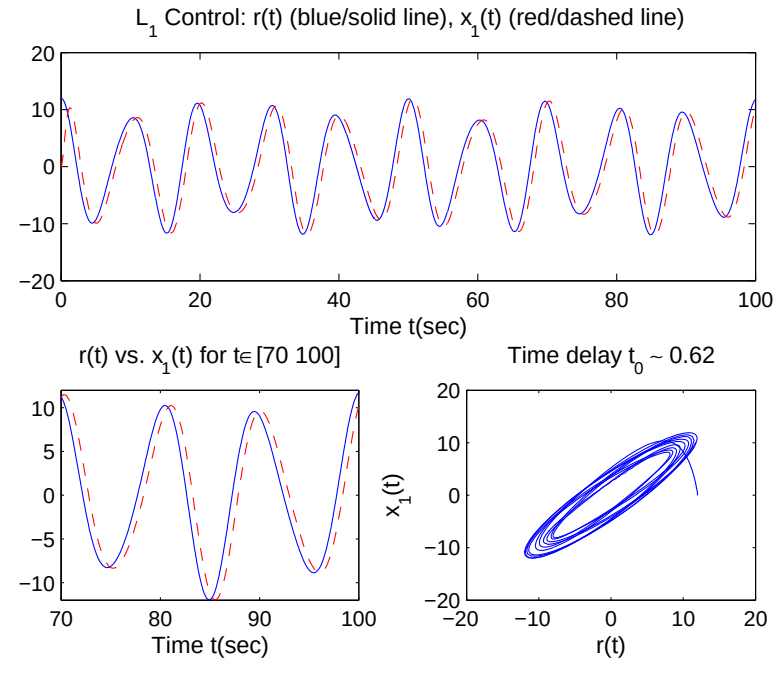

(a)

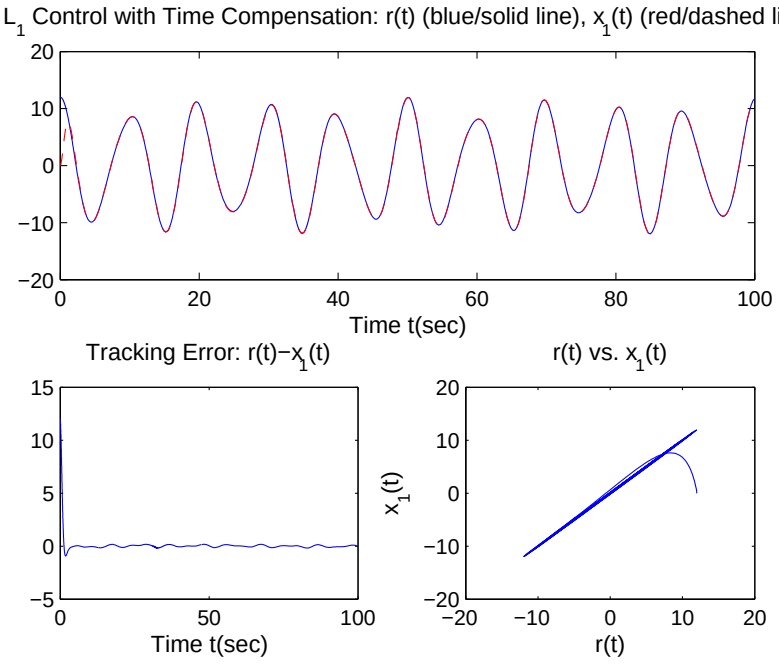

(b)

Figure 5.8: Performance of $\mathcal{L}_1$ adaptive controller for $r = 2\cos(t) + 10\cos(\pi t/5)$ using ODE15s with (a) no time compensation and (b) time compensation.

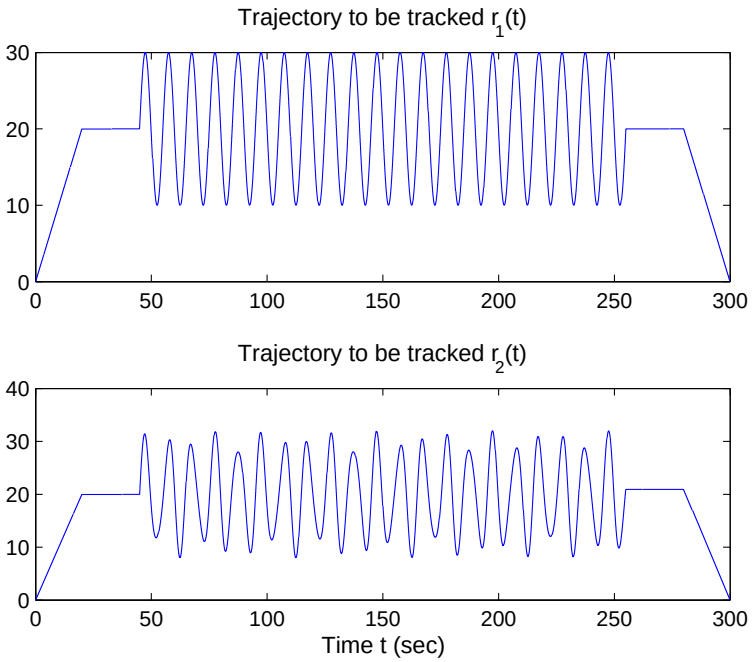

Figure 5.9: Trajectories to be tracked

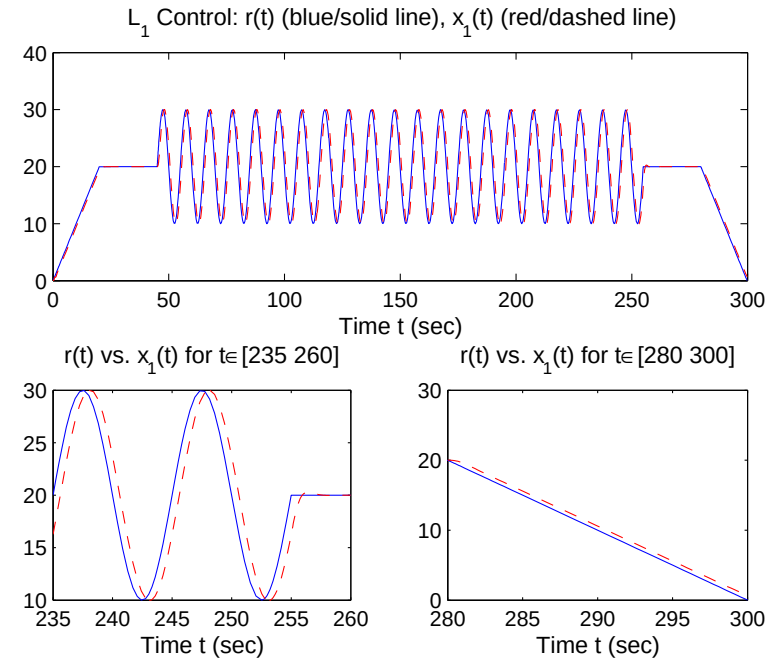

(a)

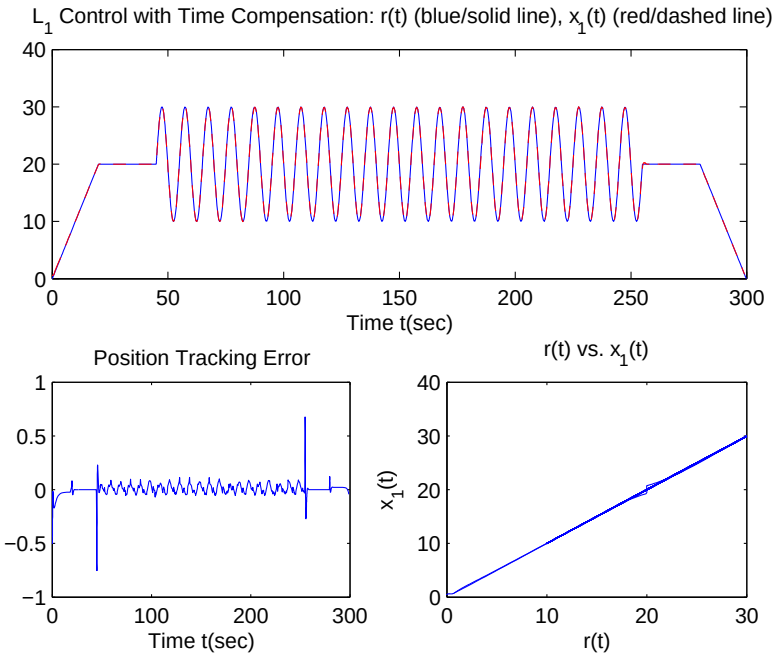

(b)

Figure 5.10: Performance of $\mathcal{L}_1$ adaptive controller for $r_1(t)$ using ODE15s with (a) no time compensation and (b) time compensation.

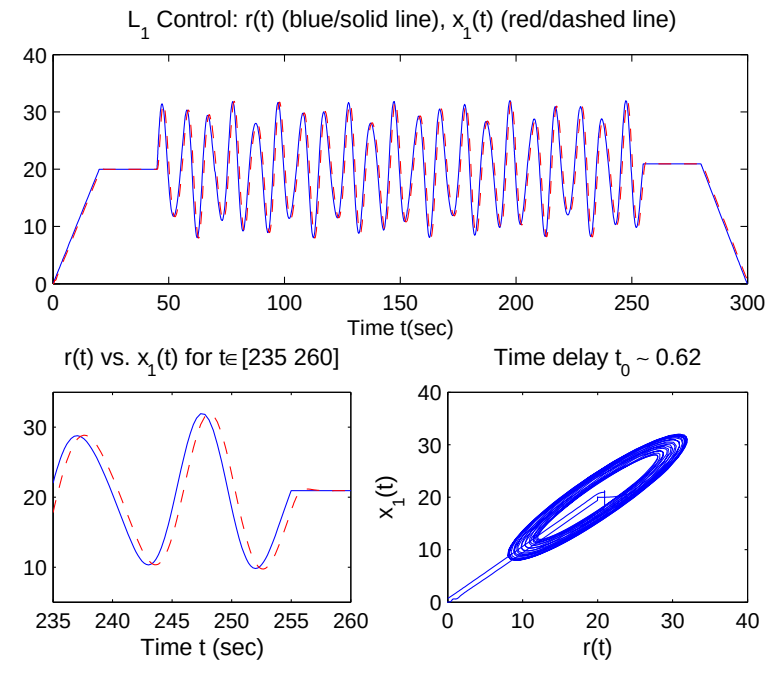

(a)

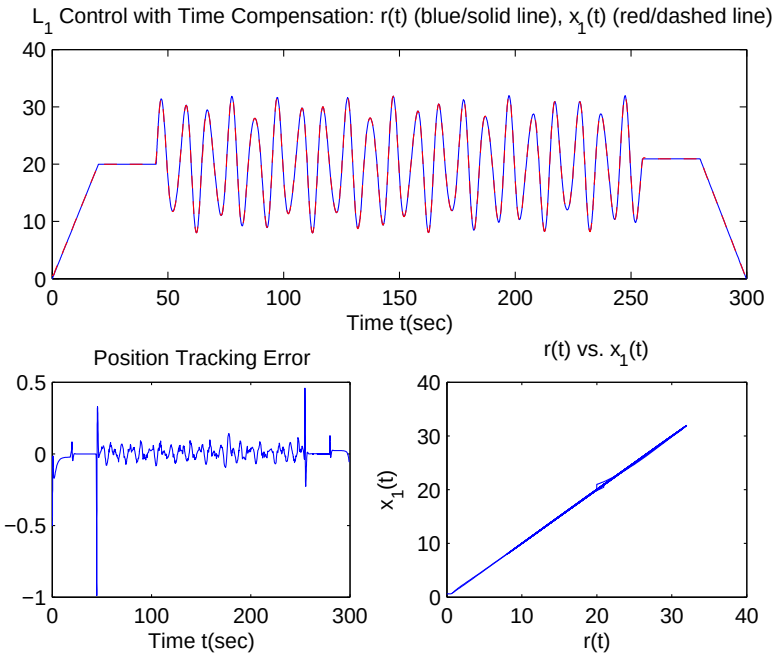

(b)

Figure 5.11: Performance of $\mathcal{L}_1$ adaptive controller for $r_2(t)$ using ODE15s with (a) no time compensation and (b) time compensation.

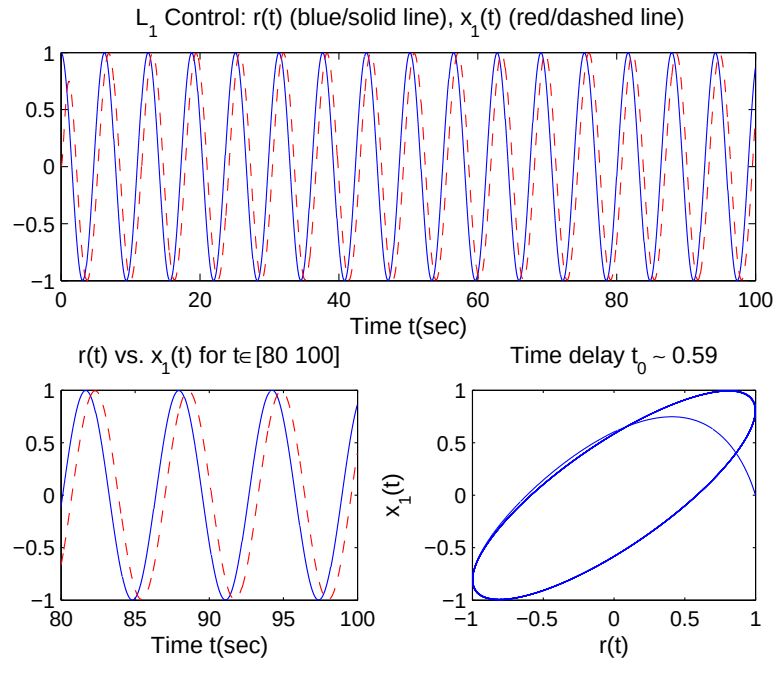

(a)

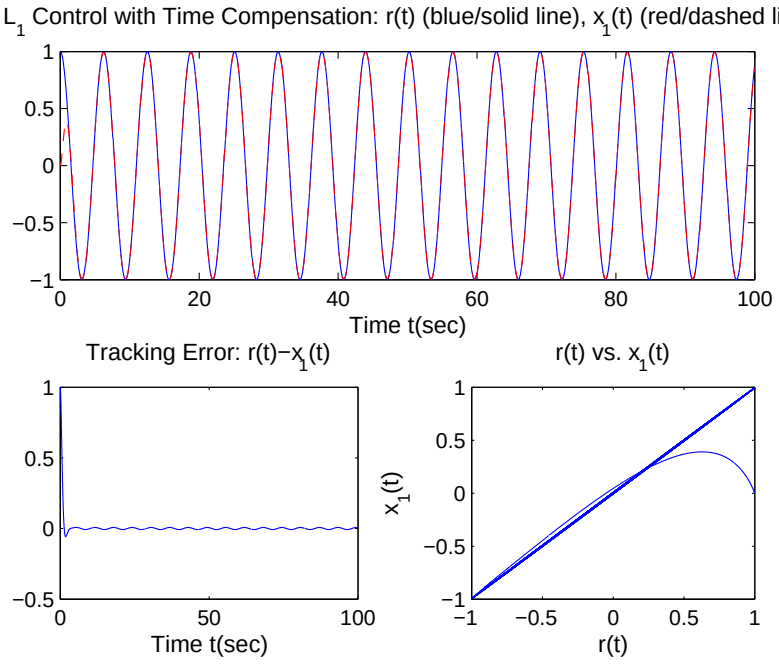

(b)

Figure 5.12: Performance of $\mathcal{L}_1$ adaptive controller for $r(t) = \cos(t)$ using the implicit Euler method with (a) no time compensation and (b) time compensation.

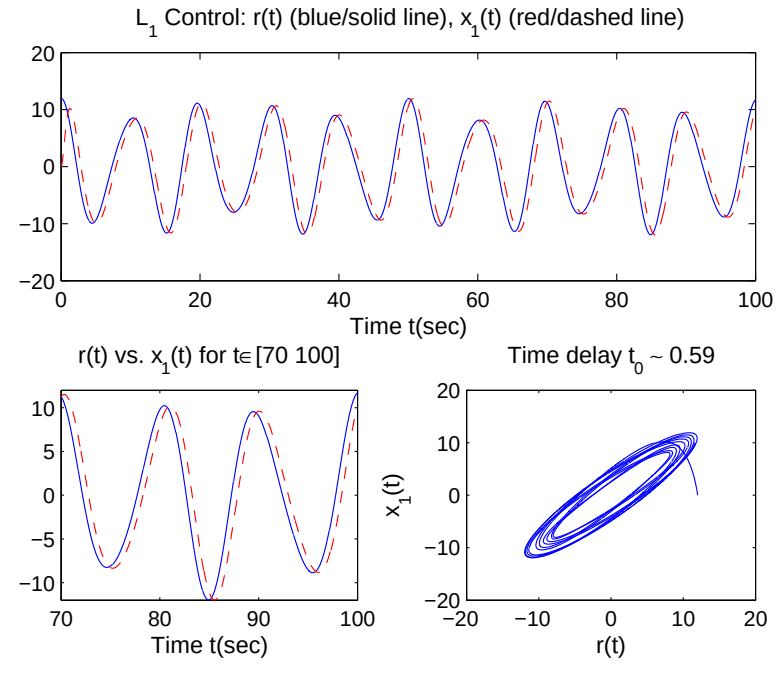

(a)

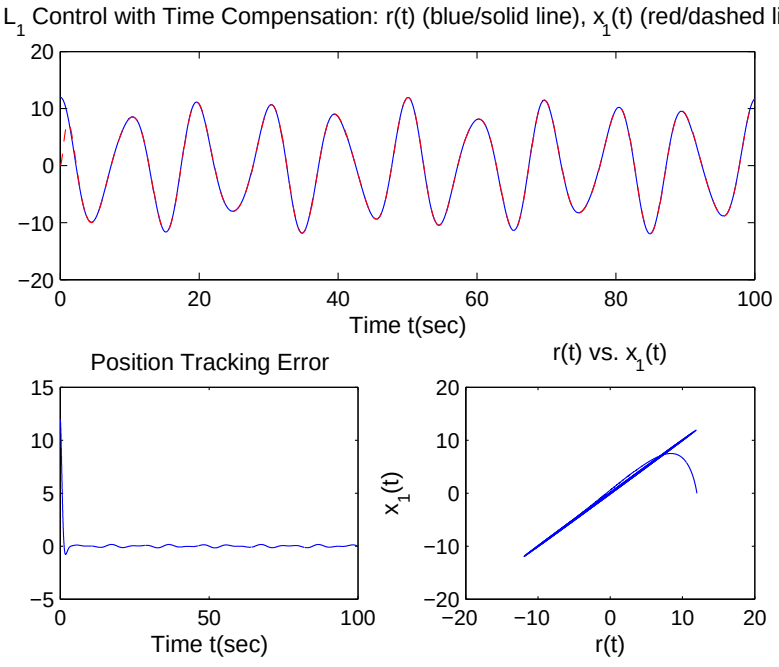

(b)

Figure 5.13: Performance of $\mathcal{L}_1$ adaptive controller for $r = 2\cos(t) + 10\cos(\pi t/5)$ using the implicit Euler method with (a) no time compensation and (b) time compensation.

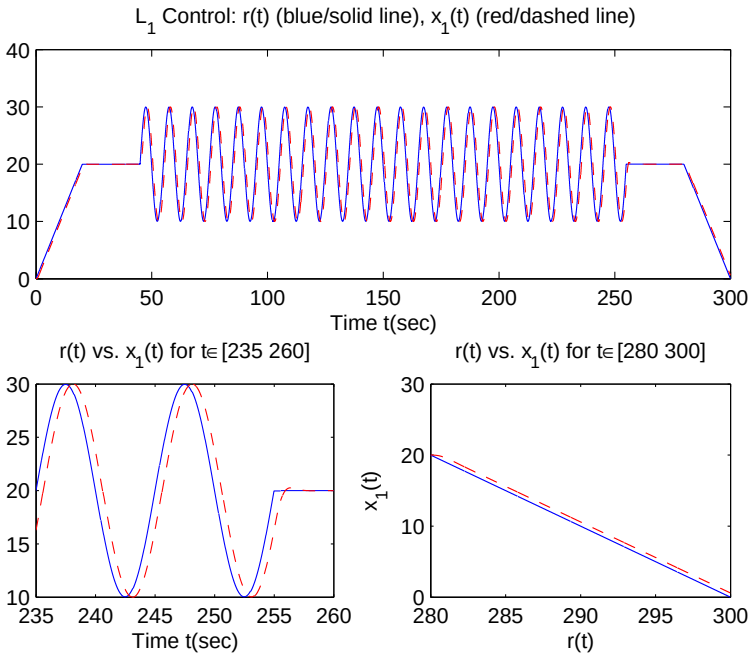

(a)

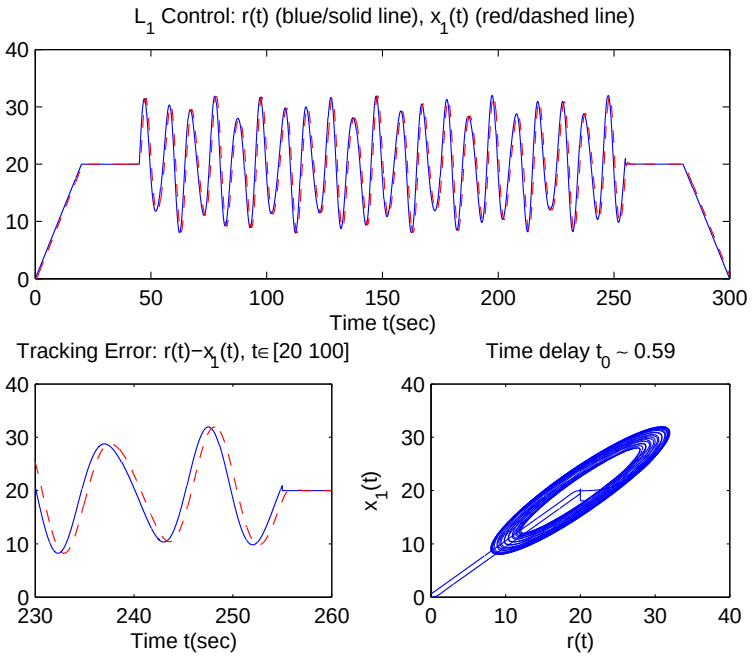

(b)

Figure 5.14: Performance of $\mathcal{L}_1$ adaptive controller for $r_1(t)$ and $r_2(t)$ using the implicit Euler method with (a) no time compensation and (b) time compensation.

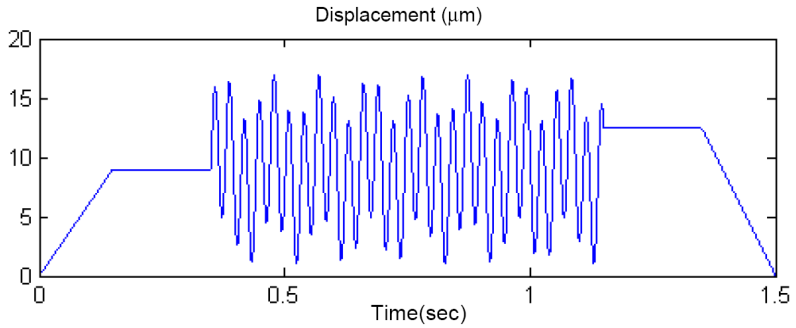

Figure 5.15: Reference Trajectory $r_3(t)$

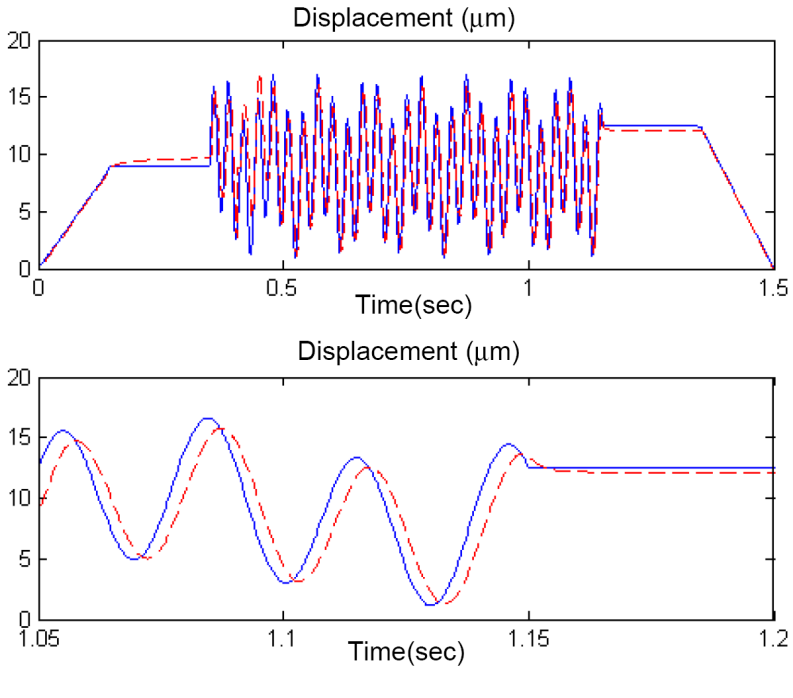

(a)

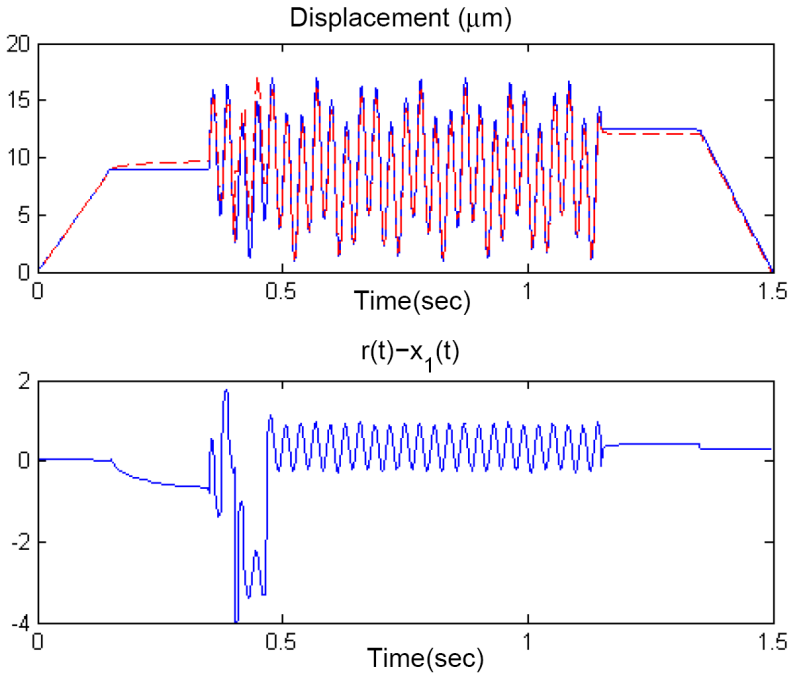

(b)

Figure 5.16: Performance of $\mathcal{L}_1$ adaptive controller for $r_3(t)$ using ODE15s with (a) no time compensation and (b) time compensation.

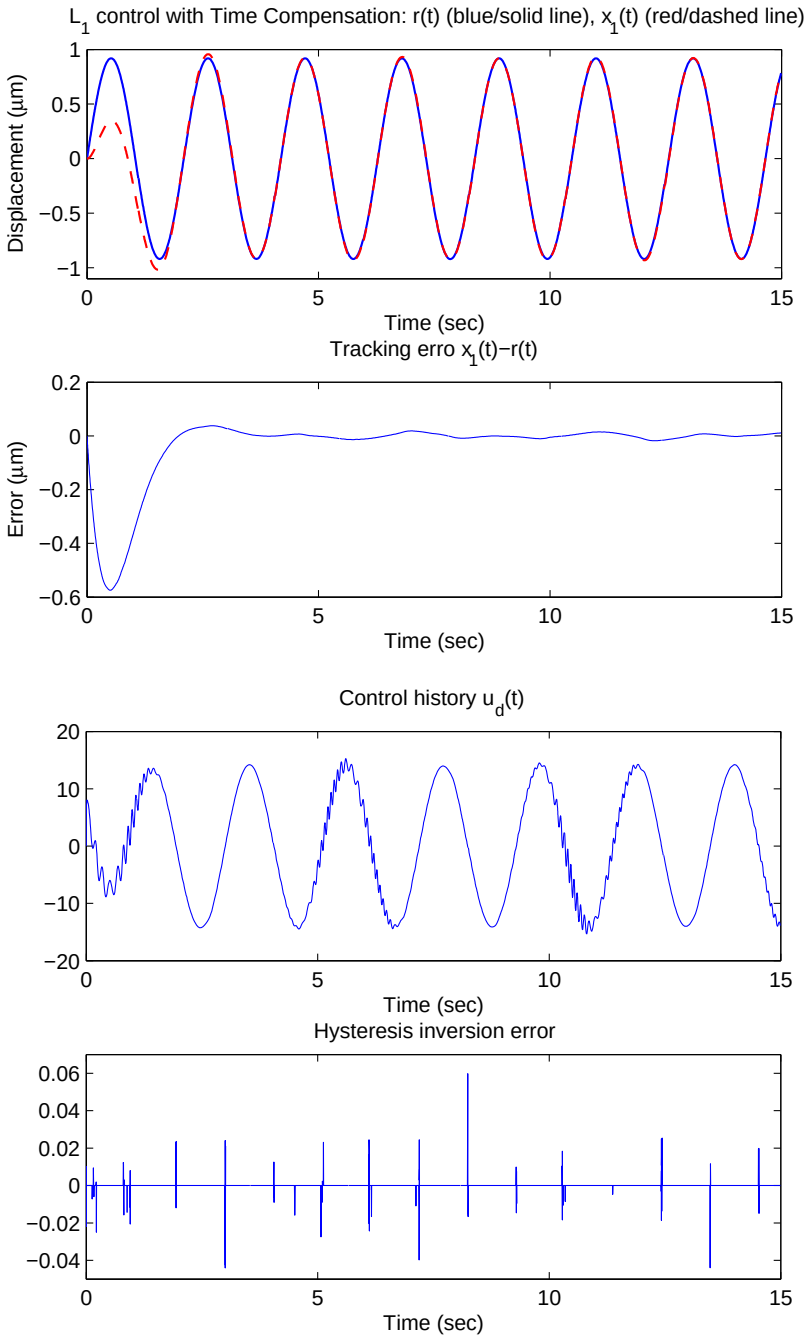

Figure 5.17: $\mathcal{L}_1$ adaptive control performance that can be compared with MRAC results shown in Figure 4.3(a) and Figure 4.6(a): (a) tracking performance and error; (b) control signal and history of hysteresis inversion error.

Chapter 6

Nonlinear Parameter Estimation

In the filter design paradigm (see Figure 6.1) for systems with hysteresis inversion-based, three sources of error exist. The first is the fact that the model is not an exact representation for the system. The second source is the fact that the inverse operator does not have an analytic form and is approximately inverted using iteration algorithms [3, 4, 5, 39]. The implication is that $u_d(t)$ is not generally equal to $u(t)$ in Figure 6.1 or Figure 2.5, even if the homogenized distribution functions are accurately known. The third source of error is uncertainty in the distribution functions and hysteresis kernel parameters. For example, internal heat generating during the operation of the transducer may affect the behavior of the inherent hysteresis in the material [34]. Figure 6.2 illustrates the effect of temperature on the hysteresis behavior in PLZT.

Identification of the hysteresis distribution functions can be accomplished using methods that are either nonparametric or parametric. In nonparametric methods, the homogenized energy model is discretized, and data fitting techniques, such as least square [43], are used to determine material parameters. This approach requires a significant amount of data and time and also must be done prior to the activation of the transducer. In parametric methods, a form for the distribution functions, such as Gauss-Gauss, lognormal-Gauss, or lognormal-normal, is assumed, and the unknown parameters in the distribution functions are estimated. However, it may be necessary to adjust the parameters in the hysteresis model to be adjustable to reflect changes in hysteretic behavior caused by the internal heat or temperature changes.

The nonlinear parameter estimation techniques proposed in [17, 56] have proven to

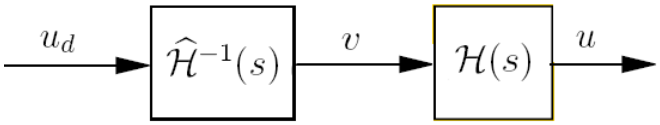

Figure 6.1: Depiction of hysteresis inversion. Here u_d represents the desired output for the hysteresis operator $\mathcal{H}$. The (approximate) inverse operator $\widehat{\mathcal{H}}^{-1}$ takes u_d as its input and outputs a signal v so that the output u of $\mathcal{H}$ is close to u_d.

be effective for identifying parameters in the Preisach hysteresis model while the transducer is operating and can provide either continuous or periodic tuning of parameters which may vary during the operation. In this chapter, we extend this parameter identification method to the homogenized energy model and develop adaptive parameter estimation algorithms to estimate and update parameters online.

6.1 Adaptive Parameter Estimation When Physical Hysteresis Output is available

In this section, feedback from the physical hysteresis output is used to estimate hysteresis parameters in the inverse filter and ultimately reduce the inversion error to achieve the control objective. This adaptive inverse estimation approach is illustrated in Figure 6.3.

6.1.1 Galerkin Representation of Densities

We consider the problem of estimating parameters using the Galerkin expanded densities (2.14)-(2.15). To illustrate it in more detail, we consider the homogenized energy operator $\mathcal{H}$ in the context of ferroelectric materials; i.e., Equation (2.9)

$$[P(E)](t) = \int_{-\infty}^{\infty}\int_{0}^{\infty} \nu_c(E_c)\nu_I(E_I)\overline{P}(E_I + E(t); E_c, x_+)dE_c dE_I$$

where $\nu_c(E_c)$, $\nu_I(E_I)$ respectively denote the coercive and interaction field densities. Densities are represented by Galerkin expansion in Equation (2.14); i.e.,

$$\nu_c(E_c) = \sum_{i=0}^{n} \alpha_i \phi_i(E_c) \quad \text{and} \quad \nu_I(E_I) = \sum_{j=0}^{m} \beta_j \phi_j(E_I)$$

where ϕ_i and ϕ_j are basis functions specified by (2.15).

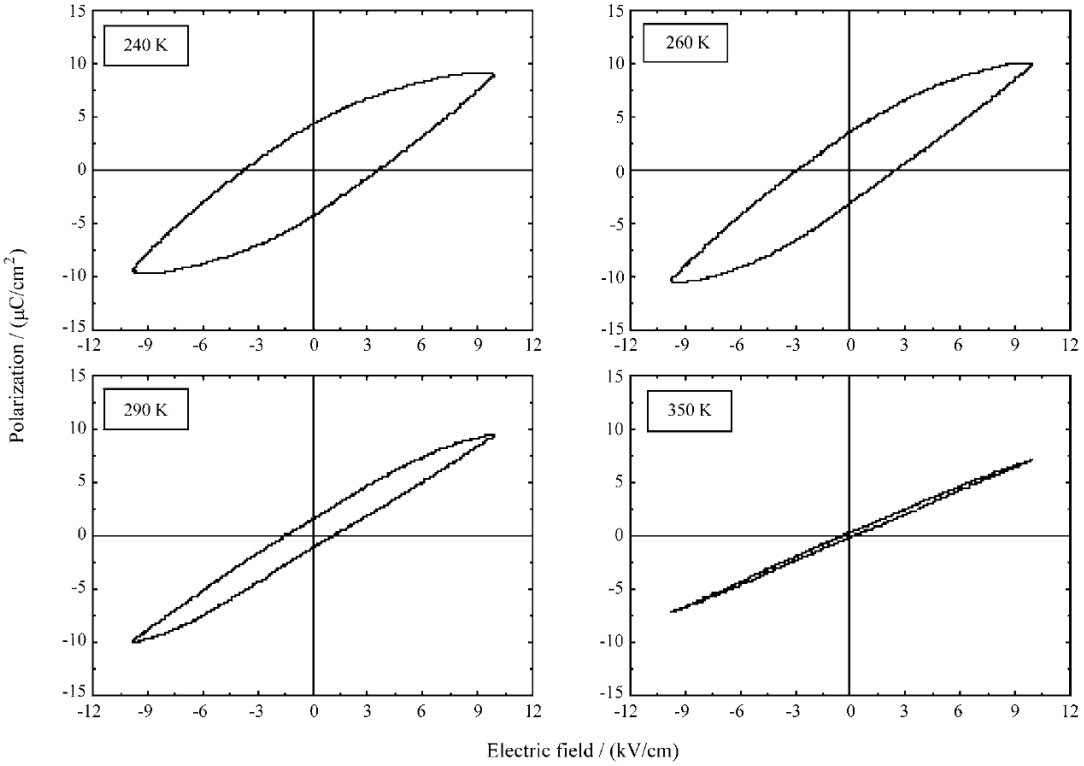

Figure 6.2: Temperature-dependence of the hysteresis loops for the PLZT 10/65/35 ceramics.

In this case, the parameters that need to be identified for the model are the Galerkin expansion coefficients α_i and β_j, the remanence P_R, and the reciprocal slope η. To simplify analysis relating these parameters to the estimation algorithm, we assume that remanence P_R and reciprocal slope η are accurately estimated off-line and remain approximately constant during operation. Following positive saturation, the modeled polarization at $E = 0$ is

$$[P(0)](t) = P_R \int_{-\infty}^{\infty} \int_{0}^{\infty} \nu_c(E_c)\nu_I(E_I)[x_+(E_I; E_c)](t) dE_c dE_I. \tag{6.1}$$

Consequently, by examining the data value at $E = 0$, we can estimate the remanent polarization P_R, as illustrated in Figure 6.4.

For the reciprocal slope η, we then can examine the $E - P$ hysteresis loop in areas of polarization saturation which yields the reciprocal susceptibility relation

$$\eta = \frac{\partial E}{\partial P}. \tag{6.2}$$

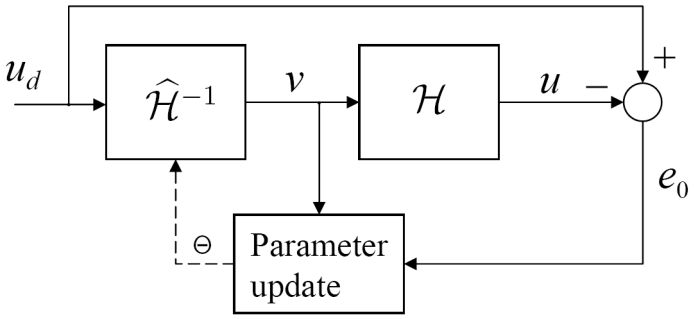

Figure 6.3: Schematic of adaptive inverse control. The inversion error $e_0 = u_d - u$ is used to update the hysteresis parameters online. It is assumed here that the output u of the hysteresis operator can be measured.

By choosing two data points (E_1, P_1) and (E_2, P_2), we approximate η^{-1} via the relation

$$\eta^{-1} \approx \frac{\Delta P}{\Delta E} = \frac{P_2 - P_1}{E_2 - E_1}. \tag{6.3}$$

The parameters to be estimated reduce to the Galerkin expansion coefficients. To derive the adaptive estimation algorithm for Galerkin expansion coefficients, we consider the polarization model (2.14) formulated in terms of the joint density

$$\nu = \nu_c \cdot \nu_I = \Theta^T \Phi(E_c, E_I) \tag{6.4}$$

where $\Phi(E_c, E_I)$ is the joint basis functions and Θ^T is the joint coefficient vector to be estimated. The goal is to design an adaptive algorithm that provides stability and assumes that the parameter vector Θ tracks its real value. To this end, we first make an assumption through the chapter that we have a physical hysteretic device H with its output denoted

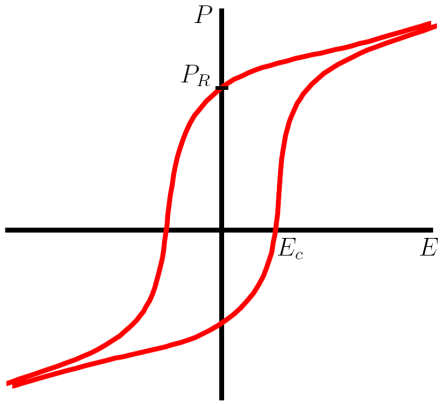

Figure 6.4: Ferroelectric hysteresis, remanent polarization P_R, and coercive field E_c.

by $u(t)$. Since it has been shown theoretically and experimentally in [3, 4, 36, 39, 45] that the modeling errors between the physical hysteretic device H and the homogenized energy model $\mathcal{H}$ are bounded, it is reasonable for us to use the precise homogenized energy model to approximate the physical device output $u(t)$ in the algorithm development and simulations. We then define two errors:

- Inversion error $e_0 = u_d - u$,
- Prediction error $e = \widehat{u} - u$.

As illustrated in Figure 6.3, u_d is the desired output to be generated, u is the real output of the physical hysteresis operator, which is assumed available for measurement and approximated by the precise homogenized energy model in the simulation. Here, $\widehat{u}$, which is not shown in Figure 6.3, represents the output of homogenized energy model with parameter estimate $\widehat{\Theta}$.

The estimation algorithm is designed based on the hysteresis output difference and a discrete-time setting is considered in the following analysis. To avoid ambiguity, it is assumed that the input to the homogenized energy model is monotonically changed from $u(n)$ to $u(n+1)$.

The output $u(n)$ of the physical piezoelectric actuator, which is approximated by the precise polarization model, can be expressed as a combination of the real density values; i.e.,

$$u(n) = \int_0^\infty \int_{-\infty}^\infty \Theta^T(n)\Phi(n)\overline{P}(E_I + v; E_c, x_+)dE_I dE_c. \tag{6.5}$$

Since the true values of coefficient vector Θ are unknown, the inversion process has to be performed based on a parameter estimation $\widehat{\Theta}$. Equivalently, the modeled polarization $\widehat{P}$ with parameter vector $\widehat{\Theta}$ is inverted at instant time n yielding the output

$$\widehat{u}(n+1) = \int_0^\infty \int_{-\infty}^\infty \widehat{\Theta}^T(n+1)\Phi(n+1)\overline{P}(E_I + v(t); E_c, x_+)dE_I dE_c. \tag{6.6}$$

Since the physical output $u(n)$ and polarization model $\widehat{u}(n)$ have the same electric field input $v(\cdot)$, and they are assumed to be represented by the same basis functions $\Phi(E_c, E_I)$, the prediction error, as defined previously, is

$$e(n+1) = \widehat{u}(n+1) - u(n+1) \leq \int_0^\infty \int_{-\infty}^\infty \widetilde{\Theta}^T(n)\Phi(n+1)\overline{P}_{max}dE_I dE_c. \tag{6.7}$$

Here $\widetilde{\Theta} = \widehat{\Theta} - \Theta$ is the parameter estimation error and $\overline{P}_{max}$ is an upper bound of the kernel $\overline{P}$.

Motivated by the prediction error relation (6,7), the Galerkin parameter vector $\widehat{\Theta}$ is updated in the inverse filter using the gradient-based algorithm

$$\widehat{\Theta}(n+1) = \widehat{\Theta}(n) - \gamma \frac{e(n+1)\overline{P}_{max}\,\Phi(n+1)}{\Phi^T(n+1)\Phi(n+1)}. \tag{6.8}$$

If the true parameter vector Θ is known to lie in a bounded set, a projection step (Definition 5.15) can be used to ensure that the parameter estimate $\widehat{\Theta}$ also lies within the set.

6.1.2 Inverse Estimation Scheme for Hysteresis Parameters

The adaptive inverse parameter estimation approach, which is illustrated in Figure 6.3, is summarized in the following steps

- $v(n+1) = \begin{cases} v_{min}, & u_d(n+1) < -\widehat{u}_{sat}(n) \\ \widehat{\mathcal{H}}^{-1}(u_d(n+1)), & -\widehat{u}_{sat}(n) \le u_d(n+1) \le \widehat{u}_{sat}(n) \\ v_{max}, & u_d(n+1) > \widehat{u}_{sat}(n) \end{cases}$
- Update the hysteresis parameter vector Θ in the inverse filter using algorithm (6.8)
- n:=n+1, and iterate

Here $\pm\widehat{u}_{sat}$ are the saturation bounds provided by the homogenized energy model.

6.1.3 Parameter Convergence

The convergence of the parameter vector Θ in Equation (6.8) is established by the following theorem.

Theorem 6.1 *([56], Parameter Convergence Requirement)*: If the adaptation gain γ in parameter estimation algorithm (6.8) satisfies the condition $\gamma \in (0,\, 2)$, then the parameter vector estimate $\widehat{\Theta}$ converges to some constant vector $\widehat{\Theta}_\infty$.

The proof is similar to the proof of *Parameter Convergence Requirement* in [56].

Proof ([56]): Denoting $\epsilon(n) = \widetilde{\Theta}^T(n)\widetilde{\Theta}(n)$, we can represent the quadratic form of the parameter error as

$$\begin{aligned} \epsilon(n+1) - \epsilon(n) &= \widetilde{\Theta}^T(n+1)\widetilde{\Theta}(n+1) - \widetilde{\Theta}^T(n)\widetilde{\Theta}(n) \\ &= \left(\widehat{\Theta}^T(n+1) - \widehat{\Theta}^T(n)\right)\left(\widetilde{\Theta}(n+1) + \widetilde{\Theta}(n)\right). \end{aligned} \tag{6.9}$$

It then follows from Equations (6.8) and (6.9) that

$$\epsilon(n+1) \leq \epsilon(n) - \gamma(2-\gamma)\frac{e^2(n+1)\overline{P}^2 P_{max}}{\Phi^T(n+1)\Phi(n+1)} \leq \epsilon(n) \tag{6.10}$$

for any $0 < \gamma < 2$.

Since $\epsilon(n) > 0$, inequality (6.10) implies that $\epsilon(n) \to \epsilon_\infty$ as $n \to \infty$, for some constant ϵ_∞. Consequently, $\widehat{\Theta}(n) \to \widehat{\Theta}_\infty$, for some constant vector $\widehat{\Theta}_\infty$.

Furthermore, we reformulate the relation (6.10) as

$$\frac{e^2(n+1)\overline{P}^2_{max}}{\Phi^T(n+1)\Phi(n+1)} = -\frac{\epsilon(n+1)-\epsilon(n)}{\gamma(2-\gamma)}. \tag{6.11}$$

Summing relation (6.11) over n yields

$$\sum_{n=0}^{\infty} \frac{e^2(n+1)\overline{P}^2_{max}}{\Phi^T(n+1)\Phi(n+1)} = \frac{1}{\gamma(2-\gamma)}(\epsilon(0)-\epsilon_\infty) \leq \infty. \tag{6.12}$$

Since $0 < \Phi^T(n+1)\Phi(n+1) < C_\Phi$ for some constant $C_\Phi > 0$, then relation (6.12) implies that $e(n) \to 0$ as $n \to \infty$. □

Theorem 6.2 *([56])* Given the hysteresis model (2.9) with the Galerkin expansion densities, and the parameter estimation algorithm (6.8) subject to the Theorem 6.1 (*parameter convergence requirement*), the inversion error between the physical hysteretic operator and the desired signal is bounded.

Proof ([56]) : From the adaptation algorithm, the inversion at time $n+1$ is exact with $\widehat{u}(n+1) = u_d(n+1)$ if $|u_d(n+1)| < \widehat{u}_{sat}(n)$. If the latter condition fails,we can show that $|e_0(n+1)| \leq |e(n+1)|$. Indeed, suppose $u_{sat} \geq u_d(n+1) > \widehat{u}_{sat}(n)$. The inversion algorithm produces $v(n+1) = v_{max}$, resulting in $u_{n+1} = u_{sat}$ and $\widehat{u}_{n+1} = \widehat{u}_{sat}$. Therefore, from $e(n) \to 0$, it follows that the tracking error $e_0(n) \to 0$ as $n \to \infty$. □

6.2 Adaptive Parameter Estimation when Hysteresis Output is not Available

The adaptive parameter estimation algorithm depicted in Figure 6.3 assumes the availability of the polarization (or magnetization) output for feedback. In applications, the hysteresis module is coupled with other dynamics of a system and its output often cannot be directly measured. The structure depicted in Figure 2.5 is typical, where the feedback

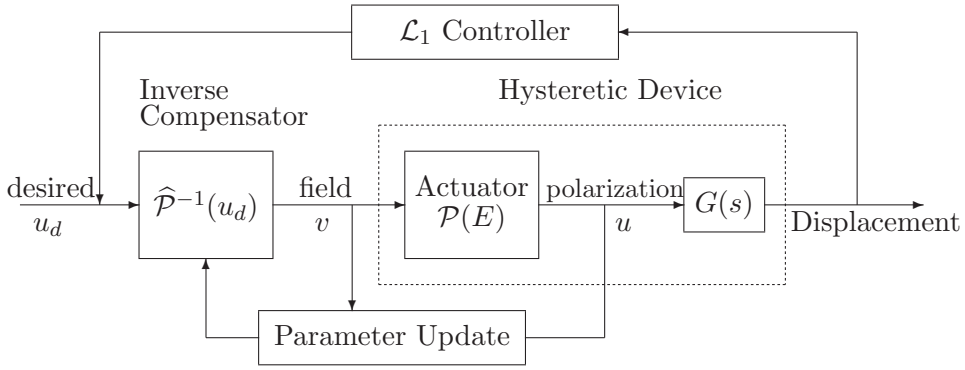

Figure 6.5: $\mathcal{L}_1$ adaptive inverse control with parameter update in the hysteresis model when the output of physical hysteresis operator is unavailable to measure.

signal is the output of a dynamic module. The algorithm discussed in Section 6.1.2 can be extended to accommodate the latter requirement. It is investigated in [52], where unknown parameters are present in both linear dynamics and hysteresis. Over-parameterization is used to accommodate the bilinearly coupled parameters in hysteresis and dynamics. We can consider extending the parameter estimation method proposed in [52] to systems involving the homogenized energy model. It also would be interesting to combine the hysteresis parameter estimation method [52] with the $\mathcal{L}_1$ control method described in Chapter 5 to regulate the tracking output of the smart hysteretic systems, as illustrated in Figure 6.5. Both of these constitute our future work.

6.3 Simulation Results

Simulations have been conducted to illustrate the adaptive estimation algorithm (6.8) used to estimate hysteresis parameters in the inverse filter. We assume here that the interaction density is known. The result displayed in Figures 6.5 and 6.6 incorporate 9 coercive field bases for $\nu_c(E_c)$ (three standard deviation, three means) and five interaction field bases in the expansion of $\nu_I(E_I)$. Final parameters for the coefficients of the coercive field bases are compiled in Table 6.1. A fit to data is presented is Figure 6.8 with estimated coercive density coefficients, the residual of the model versus data can be greatly decreased if more density basis functions are incorporated.

Simulations are also conducted for tracking a typical reference signal in a dynamic system, under the assumption that the physical output is measurable. In this case where

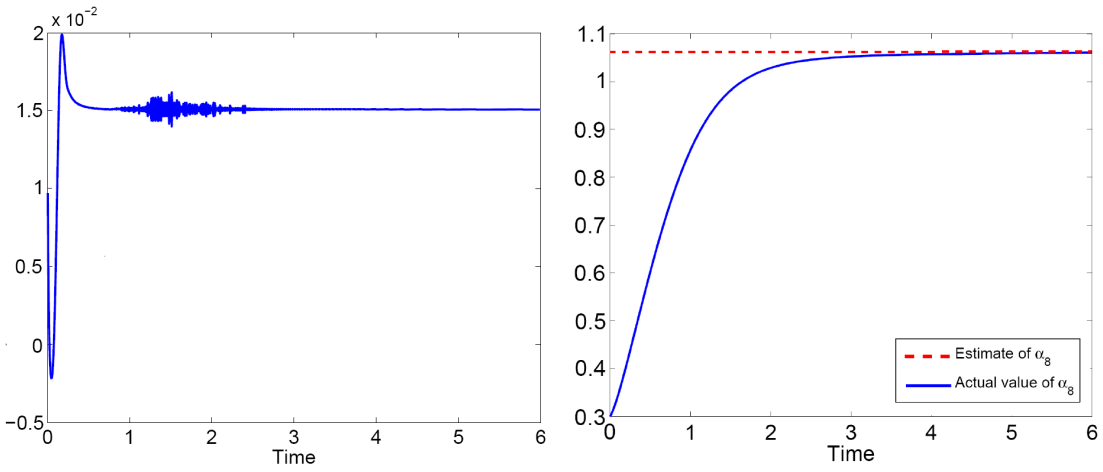

Figure 6.6: (a) Parameter estimation value for α_2 and (b) Parameter estimation value for α_8.

tracking error must be considered, a feedback controller may be utilized as depicted in Figure 1.2(a). To illustrate this, we introduce a proportional integral (PI) feedback control to the dynamics depicted in Figure 1.2(a), which means that the system responds in proportion to the tracking error and the integral of the tracking error over time. Proportional control moves the physical output to the reference trajectory when it is very far away the reference signal, and integral control adjusts the proportional offset to ensure that the physical output accurately stays around the reference trajectory. PI feedback is chosen here because it is easy to implement and moderately accurate.

The positioning error of a PI feedback control using hysteresis parameter estimation algorithm is shown in Figure 6.9 for $k_P = 0.4$ and $k_I = 10^4$. As can be seen, the peak error is about 5 microns which occurs at the discontinuous point of the reference trajectory. This is fairly accurate for a simple PI control.

Table 6.1: Coefficient for coercive basic elements

$\alpha_1 = -2.7688 \times 10^{-2}$	$\alpha_4 = 9.6098 \times 10^{-3}$	$\alpha_7 = 3.4007 \times 10^{-2}$
$\alpha_2 = 1.5279 \times 10^{-2}$	$\alpha_5 = -5.9536 \times 10^{-2}$	$\alpha_8 = 1.054$
$\alpha_3 = 6.7787 \times 10^{-2}$	$\alpha_6 = 1.2366 \times 10^{-2}$	$\alpha_9 = -4.7734 \times 10^{-2}$

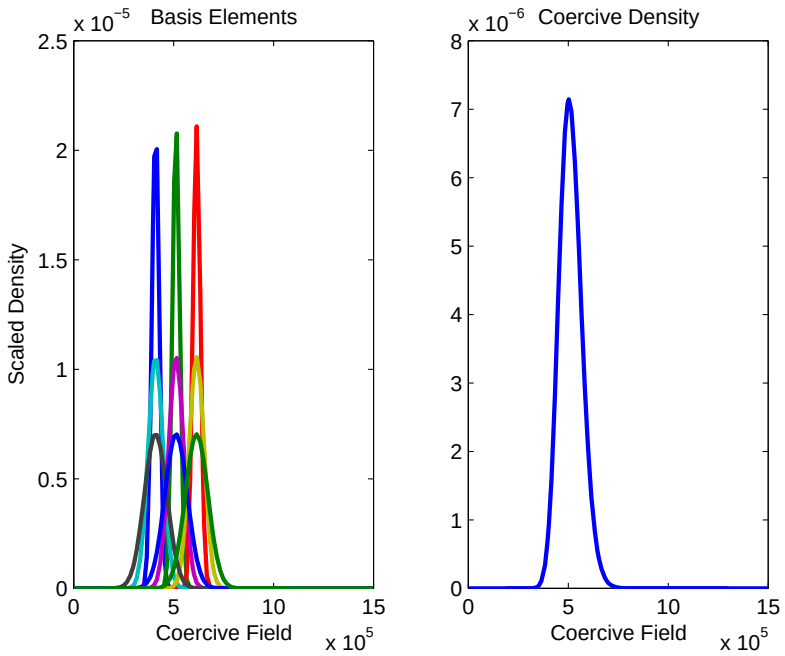

Figure 6.7: Galerkin coercive basis elements used to construct the employed coercive and interaction field densities

6.4 Concluding Remarks

The nonlinear parameter identification techniques developed in [56] have been shown to be effective for identifying parameters in the Preisach hysteresis model incorporated as a part of inverse control. We have extended this parameter identification method to apply to the hysteretic system involving the homogenized energy model. The proposed adaptive parameter estimation algorithm can be used to estimate parameters for a wide range of smart materials including ferroelectric and ferromagnetics and ferroelastic, as long as the hysteresis is quantified by the homogenized energy model. This parameter online-estimated algorithm may be more efficient and accurate than current methods of parameter identification, such as least square fits to data. For now, we assume that we already have a good estimate of remanence P_R and reciprocal slope η; next, we would apply this method to identify the full set of parameters in the homogenized energy inverse model, including P_R and η; i.e., update $\Theta = [P_R, \eta, \alpha_1, \cdots, \alpha_{N_i}, \beta_1, \cdots, \beta_{N_j}]$ simultaneously online.

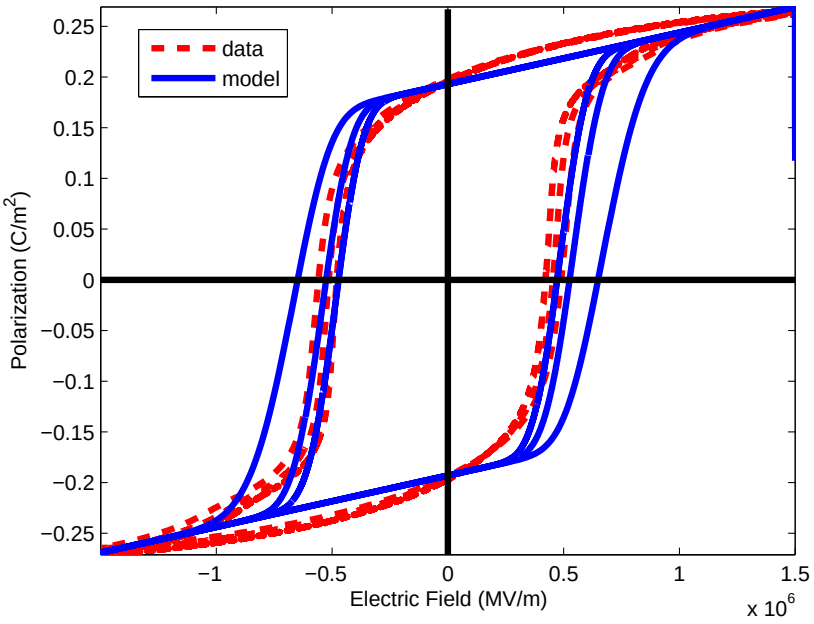

Figure 6.8: Adaptive estimated polarization model fits to PZT major loop data from [36].

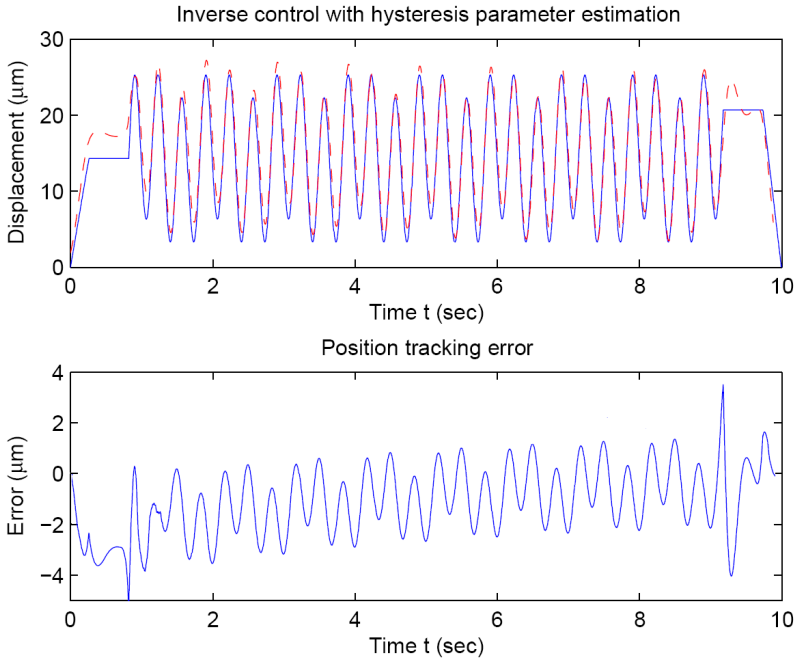

Figure 6.9: Simulation result of tracking a typical reference trajectory with adaptive hysteresis parameter estimation.

Chapter 7

Adaptive Nonlinear Control

Adaptive control is a well-establish methodology for the design of feedback control systems. In the 1980s, most of the effort in adaptive control research focused on robust adaptive control for linear systems, which dealt with modifications to the adaptive algorithms and the control law to address some types of uncertainties [13, 21, 25, 26, 28]. The adaptive laws and control schemes developed and analyzed in Chapter 4 and 5 are based on the adaptive linear control techniques to eliminate the inversion error introduced by the hysteresis inverse model. It is interesting to note similarities and differences between robust and adaptive control designs. The robust approaches treat the uncertainties as an unknown where the only available information available is some bounds. The robust control law is obtained based on these bounds and, in fact, is designed to stabilize the systems for any uncertainty within the assumed bounds. As a result, the robust control law tends to be conservative and may lead to large control input signals or control saturation. On the other hand, adaptive control assumes a special structure for the uncertainty where the nonlinearities are known but the parameter are unknown. In contrast to robust control, in adaptive control the objective is to try to eliminate the uncertain or time-varying parameters to reduce the level of uncertainty.

The area of adaptive nonlinear control has evolved quickly on quickly since the early 1990s as illustrated by the survey paper [29] and three textbooks [20, 22, 38]. We observe that the development of most adaptive nonlinear controller designs are based on Lyapunov methods; e.g., small-signal linearization, feedback linearization, and backstepping, etc.

A physical plant driven by a smart actuator is a typical nonlinear system with inherent hysteresis behavior and constitutive nonlinearities. The most common approach to cancel these nonlinearities is to construct an inverse filter and then design control signal to minimize the hysteresis; e.g., see the methods described in Chapter 4 and 5. The use of inverse filters has the advantage of providing linear control designs and can improve tracking performance by effectively compensating for nonlinear and irreversible material behavior; however, these advantages are only realized if the constitutive model is efficient enough to be inverted in real time. This complexity can sometimes be avoided by the use of nonlinear control designs which circumvents the need for an inverse filter and determines the input signals that directly incorporate actuator nonlinearities.

The development of adaptive nonlinear control techniques to mitigate the effects of hysteresis has been studied for several years, and recently has reattracted significant attention [24] with the development of different types of hysteresis models; e.g., the nonlinear control algorithms have been designed for the backlash-like hysteresis model and Prandtl-Ishlinskii hysteresis model in [51] and [61], respectively. However it is quite challenging to construct a general nonlinear control framework for smart hysteretic systems (see Figure 1.2(b)) to achieve at least the basic stability requirement and implement it in real time.

In this chapter, we introduce a nonlinear control structure that combines the homogenized energy model with the available adaptive control techniques to minimize the effects of hysteresis.

7.1 Problem Formulation

Consider the hysteretic dynamics; e.g., the motion of the PZT-based stage in AFM design in Figure 3.1(a),

$$\ddot{x} + a_1\dot{x} + a_2 x = b[P(u)](t). \tag{7.1}$$

Here $u(t)$ is the input to the hysteretic operator and $[P(u)](t)$ the generated driving force. The parameters a_1, a_2 are unknown constants. Control gain b is assumed to be known and, without loss of generality, we assume that $b > 0$.

The control objective is to design a control law for $u(t)$ in the system Equation (7.1) so that the plant state $x(t)$ tracks a pre-specified reference trajectory $x_d(t)$; i.e., $x(t) \to x_d(t)$ as $t \to \infty$.

The following assumption is made through the chapter:

Assumption 7.1: The vector of reference states $\mathbf{x}_d = [x_d,\, \dot{x}_d]^T$ is continuous. Furthermore, there exists a compact set Ω_d such that

$$[\mathbf{x}_d,\, \ddot{x}_d\,]^T \in \Omega_d \in \mathbb{R}^3.$$

7.2 Nonlinear Control Design

To combine the homogenized energy model with the currently available control techniques, we consider an alternative form of polarization model relation (2.9) using the kernel expression (2.3)

$$[P(u)](t) = \underbrace{\frac{u(t)}{\eta} - P_R}_{(1)} + 2P_R \underbrace{\int_0^\infty \int_{-\infty}^\infty \nu(E_c, E_I) x_+(E_I + u(t);\, E_c) dE_I dE_c}_{(2)}. \tag{7.2}$$

Here $\nu(E_c,\, E_I)$ is the joint density function of coercive and interaction field and $x_+ \in [0, 1]$ is the fraction of positively orientated dipoles.

Notice that the second term

$$(2) \equiv \int_0^\infty \int_{-\infty}^\infty \nu(E_c,\, E_I) x_+(E_I + u(t);\, E_c) dE_I dE_c \tag{7.3}$$

of the right-hand side of (7.2) is formulated as an integral equation. Considering that the joint density function $\nu(E_c,\, E_I)$ is not a function in time, it possible to treat it as a parameter of the hysteresis model (7.1) and an adaptation law can be developed.

For the polarization model (7.2), define

$$\begin{gathered} b_\eta = b/\eta, \quad b_R = bP_R \\ [P_B(u)]\,(t) = \int_0^\infty \int_{-\infty}^\infty p_b(E_c, E_I)\, x_+(E_I + u(t); E_c) dE_I dE_c \\ p_b(E_c, E_I) = 2b_R \nu(E_c, E_I). \end{gathered} \tag{7.4}$$

Here we assume that the reciprocal slope η and the joint density $\nu(E_c, E_I)$ of the hysteresis model are unknown, which implies that adaption laws will be assigned to b_η and term $p_b(E_c, E_I)$ to obtain estimates of the corresponding unknowns.

Using expressions in (7.4), the nonlinearly system dynamics described in (7.1) then can be represented as

$$\ddot{x} + a_1\dot{x} + a_2 x = b_\eta u(t) - b_R + [P_B(u)](t) \tag{7.5}$$

which yields a linear function of the input signal $u(t)$ together with a nonlinear term $[P_B(u)](t)$.

The system (7.6) can be reformed as the ODE system

$$\begin{aligned} \dot{x}_1 &= x_2 \\ \dot{x}_2 &= \mathbf{a}^T\mathbf{x} + b_\eta u(t) - b_R + [P_B(u)](t) \end{aligned} \tag{7.6}$$

where

$$\begin{gathered} x_1(t) = x(t), \quad x_2(t) = \dot{x}(t), \quad \mathbf{x}(t) = [x_1,\, x_2]^T \\ \mathbf{a} = [-a_1,\, -a_2]^T. \end{gathered} \tag{7.7}$$

Again, it is assumed that the parameter vector $\mathbf{a}$ is unknown.

To develop the control law and adaptation laws for the parameters, we first define

$$\phi \triangleq b_\eta^{-1} = \eta/b$$

the reciprocal of b_η with the unknown parameter η. We then employ the parameter error definitions

$$\begin{aligned} \widetilde{\mathbf{a}}(t) &= \mathbf{a} - \widehat{\mathbf{a}}(t) \\ \widetilde{\phi}(t) &= \phi - \widehat{\phi}(t) \\ \widetilde{p}_b\,(t; E_c, E_I) &= p_b(E_c, E_I) - \widehat{p}_b(t; E_c, E_I) \end{aligned} \tag{7.8}$$

where $\widehat{a}$, $\widehat{\phi}$ and $\widehat{p}_b$ are the adaptive estimates of the corresponding parameters. The adaption laws for updating these parameters are given in (7.11).

For the system dynamics (7.6) with (7.7) subject to the Assumption 7.1, we introduce the following nonlinear control structure.

Control law: The control signal $u(t)$ is generated by the relation

$$u(t) = \widehat{\phi}(t) v_r(t)$$

where

$$v_r(t) = \ddot{x}_d - \widehat{\mathbf{a}}^T\mathbf{x} + u_N - c_2 z_2 - z_1 + \dot{\alpha}_1 \tag{7.9}$$

and

$$\begin{aligned} z_1 &= x_1 - x_d \\ z_2 &= x_2 - \dot{x}_d - \alpha_1 \\ \alpha_1 &= -c_1 z_1 \\ u_N &= -\Big(\left[\widehat{P}_B(u)\right](t) - b_R \Big) \end{aligned} \tag{7.10}$$

where c_1, c_2 are prescribed positive constants. The term $u_N(t)$ represents the compensator component for the integral function $[P_B(u)](t)$. Here

$$\left[\widehat{P}_B(u)\right](t) = \int_0^\infty \int_{-\infty}^\infty \widehat{p}_b(t; E_c, E_I)\, x_+(E_I + u(t); E_c) dE_I dE_c$$

is expressed as an integral equation with the joint density parameter estimate $\widehat{p}_b(t; E_c, E_I)$.

Adaptation laws: The parameters $\widehat{\phi}$, $\widehat{\mathbf{a}}$ and joint density function estimate $\widehat{p}_b$ will be updated by the following adaptation laws

$$\begin{aligned} \dot{\widehat{\mathbf{a}}}(t) &= \gamma_1\, \mathbf{x}(t) z_2(t) \\ \dot{\widehat{\phi}}(t) &= -\gamma_2\, v_r(t)\, z_2(t) \\ \frac{\partial}{\partial t}\, \widehat{p}_b(t; E_c, E_I) &= \gamma_3\, x_+\big(E_I + u(t); E_c\big)\, z_2(t) \end{aligned} \tag{7.11}$$

where γ_1, γ_2 and γ_3 are positive constants determining the rates of the adaptation.

Note that if the true values of ϕ and $\mathbf{a}$ are known to lie in some bounded compact sets, the projection operator (Definition 5.15) can be used to ensure that the parameter estimates $\widehat{\phi}$ and $\widehat{\mathbf{a}}$ also lie within the bounded sets.

The stability of the closed-loop system described in (7.6) and (7.7) with the nonlinear control structure (7.9)-(7.11) is established in the following Theorem.

Theorem 7.1 (*Stability*): For the hysteretic dynamics given in (7.1) with the homogenized energy hysteresis model (7.2), subject to Assumption 7.1, the adaptive nonlinear control structure specified by (7.9)-(7.11) ensures that all the closed-loop signals are bounded and $x(t) \to x_d(t)$ as $t \to \infty$.

Proof: Using the expression (7.7) and the definition of z_2 in (7.10), we note that

$$b_\eta u(t) = b_\eta \widehat{\phi}(t) v_r(t) = b_\eta\big(\phi - \widetilde{\phi}(t)\big) v_r(t) = v_r(t) - b_\eta \widetilde{\phi}(t) v_r(t). \tag{7.12}$$

One can also obtain

$$\begin{aligned} z_1 \dot{z}_1 &= z_1(\dot{x}_1 - \dot{x}_d) = z_1(z_2 + \alpha_1) = z_1(z_2 - c_1 z_1) = -c_1 z_1^2 + z_1 z_2 \\ \dot{z}_2 &= \dot{x}_2 - \ddot{x}_d - \dot{\alpha}_1 \\ &= \mathbf{a}^T \mathbf{x} + b_\eta u - b_R + P_B(u) - \Big(v_r + \widehat{\mathbf{a}}^T \mathbf{x} + c_2 z_2 + z_1 - u_N\Big) \\ &= \widetilde{\mathbf{a}}^T \mathbf{x} - b_\eta \widetilde{\phi}\, v_r - b_R + P_B(u) - c_2 z_2 - z_1 + u_N \\ z_2 \dot{z}_2 &= -c_2 z_2^2 - z_1 z_2 + \widetilde{\mathbf{a}}^T \mathbf{x} z_2 - b_\eta\, \widetilde{\phi}\, v_r z_2 + \big(P_B(u) - b_R\big) z_2 + u_N z_2. \end{aligned} \tag{7.13}$$

Define the Lyapunov function candidate

$$V(t) = \frac{1}{2}(z_1^2 + z_2^2) + \frac{1}{2\gamma_1}\widetilde{\mathbf{a}}^T\widetilde{\mathbf{a}} + \frac{b_\eta}{2\gamma_2}\widetilde{\phi}^2 + \frac{1}{2\gamma_3}\int_{-\infty}^{\infty}\int_0^{\infty}\widetilde{p}_b^2(t;E_c,E_I)dE_I dE_c$$

The derivative $\dot{V}$ is given by

$$\begin{aligned}
\dot{V}(t) &= z_1\dot{z}_1 + z_2\dot{z}_2 + \frac{1}{\gamma_1}\widetilde{\mathbf{a}}^T\dot{\widetilde{\mathbf{a}}} + \frac{b_\eta}{\gamma_2}\widetilde{\phi}\dot{\widetilde{\phi}} + \frac{1}{\gamma_3}\int_0^{\infty}\int_{-\infty}^{\infty}\widetilde{p}_b(t;E_c,E_I)\frac{\partial}{\partial t}\widetilde{p}_b(t;E_c,E_I)dE_I dE_c \\
&= -c_1z_1^2 + z_1z_2 - c_2z_2^2 - z_1z_2 \\
&\quad + \widetilde{\mathbf{a}}^T\mathbf{x}z_2 - b_\eta\widetilde{\phi}v_r(t)z_2 + \big([P_B(u)](t) - b_R\big)z_2 + u_Nz_2 \\
&\quad + \frac{1}{\gamma_1}\widetilde{\mathbf{a}}^T\left(\dot{\mathbf{a}} - \gamma_1\mathbf{x}z_2\right) + \frac{b_\eta}{\gamma_2}\widetilde{\phi}\left(\dot{\phi} + \gamma_2v_rz_2\right) \\
&\quad + \frac{1}{\gamma_3}\int_0^{\infty}\int_{-\infty}^{\infty}\widetilde{p}_b(t,E_I;E_c)\left(\frac{\partial}{\partial t}p_b(E_c,E_I) - \gamma_3x_+\big(E_I + u(t);E_c\big)z_2\right)dE_I dE_c \\
&= -c_1z_1^2 - c_2z_2^2 + \frac{1}{\gamma_1}\widetilde{\mathbf{a}}^T\dot{\mathbf{a}} + \frac{b_\eta}{\gamma_2}\widetilde{\phi}\dot{\phi} + \big([P_B(u)](t) - b_R\big)z_2 + u_Nz_2 \\
&\quad - z_2\int_0^{\infty}\int_{-\infty}^{\infty}\widetilde{p}_b(t,E_I;E_c)x_+\big(E_I + u(t);E_c\big)dE_I dE_c \\
&= -c_1z_1^2 - c_2z_2^2 + \frac{1}{\gamma_1}\widetilde{\mathbf{a}}^T\dot{\mathbf{a}} + \frac{b_\eta}{\gamma_2}\widetilde{\phi}\dot{\phi} + \left([P_B(u)](t) - [\widetilde{P}_B(u)](t)\right)z_2 - b_Rz_2 + u_Nz_2 \\
&= -c_1z_1^2 - c_2z_2^2 + \frac{1}{\gamma_1}\widetilde{\mathbf{a}}^T\dot{\mathbf{a}} + \frac{b_\eta}{\gamma_2}\widetilde{\phi}\dot{\phi} + [\widehat{P}_B(u)](t)z_2 - b_Rz_2 + u_Nz_2
\end{aligned}$$

The term $u_N(t) = -\left(\left[\widehat{P}_B(u)\right](t) - b_R\right)$ is a compensation component for the integral function $[P_B(u)](t)$. We then can get

$$\dot{V}(t) = -c_1z_1^2 - c_2z_2^2 + \frac{1}{\gamma_1}\widetilde{\mathbf{a}}^T\dot{\mathbf{a}} + \frac{b_\eta}{\gamma_2}\widetilde{\phi}\dot{\phi} = -c_1z_1^2 - c_2z_2^2 \le 0$$

which implies that V is nonincreasing. Hence, $z_1(t)$, $z_2(t)$ and $\widehat{\mathbf{a}}(t)$, $\widehat{\phi}(t)$, $\widehat{p}_b(t;E_c,E_I)$ are bounded. By applying that Lasalle-Yoshizawa theorem, it follows that $z_1(t) \to 0$, $z_2(t) \to 0$ as $t \to \infty$, which implies that $\lim_{t\to\infty}[x(t) - x_d(t)] = 0$. □

Note that the above statement is true only for constant parameter vector $\mathbf{a}$ and $\phi = \eta/b$. If the parameter $\mathbf{a}(t)$ and $\phi(t) = \frac{\eta}{b}(t)$ are slowly time-varying, we then have to choose large enough gains γ_1 and γ_2 such that $\dot{V} \le 0$ which implies that the Lyapunov candidate $V(t)$ is nonincreasing which ensure the boundedness of parameter estimates. The criterion regarding to the choice of appropriate gains γ_1 and γ_2 and how the gains relate to the parameter convergence or persistence excitation condition are still under investigation.

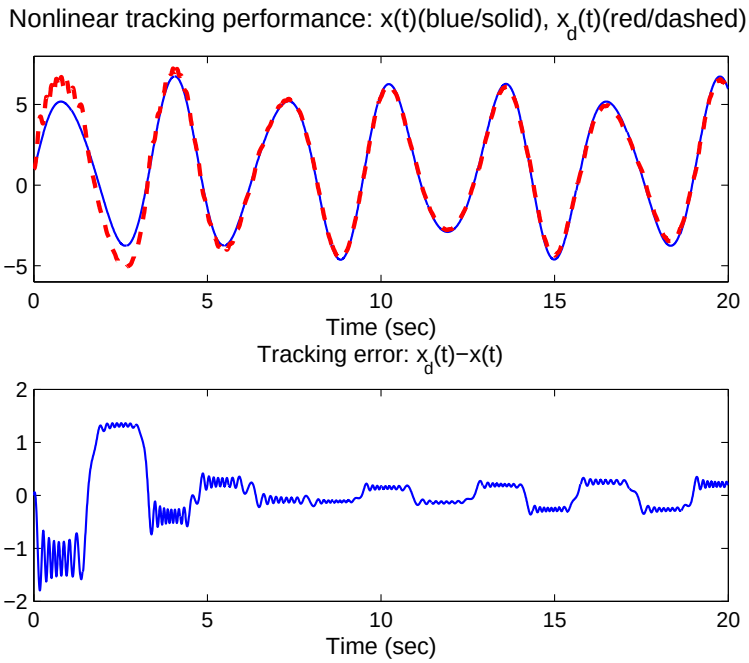

Figure 7.1: Performance of the adaptive nonlinear controller for tracking the reference trajectory $x_d(t) = 5\sin(2t) + \cos(3.2t)$.

7.3 Simulation Results

Since the homogenized energy model is a well developed hysteresis model, and to simplify the simulations for the initial step implementation, we assume here that the reciprocal slope η and integral function $[P_B(u)](t)$ with parameter p_b are known and coupling term b is unknown in the proposed control structure.

Here we illustrate the control structure numerically using a simple lumped dynamic model

$$\ddot{y} + \frac{1.8}{1.5}\dot{y} + \frac{8.1}{1.5}y = [P(u)](t). \tag{7.14}$$

The objective is to design a control signal so that the state x tracks the desired trajectory $x_d(t) = 5\sin(2t) + \cos(3.2t)$. The state trajectory and tracking error for the reference signal are shown in Figure 7.1. The simulation result illustrates that the proposed control structure mitigates the effect of hysteresis behavior and achieves reasonable precision. Note that the tracking error is not increasing towards the end, it is just oscillating to zero at extremely slow rate. Parameter tracking results for ϕ and vector $\mathbf{a}$ are shown in Figure 7.2.

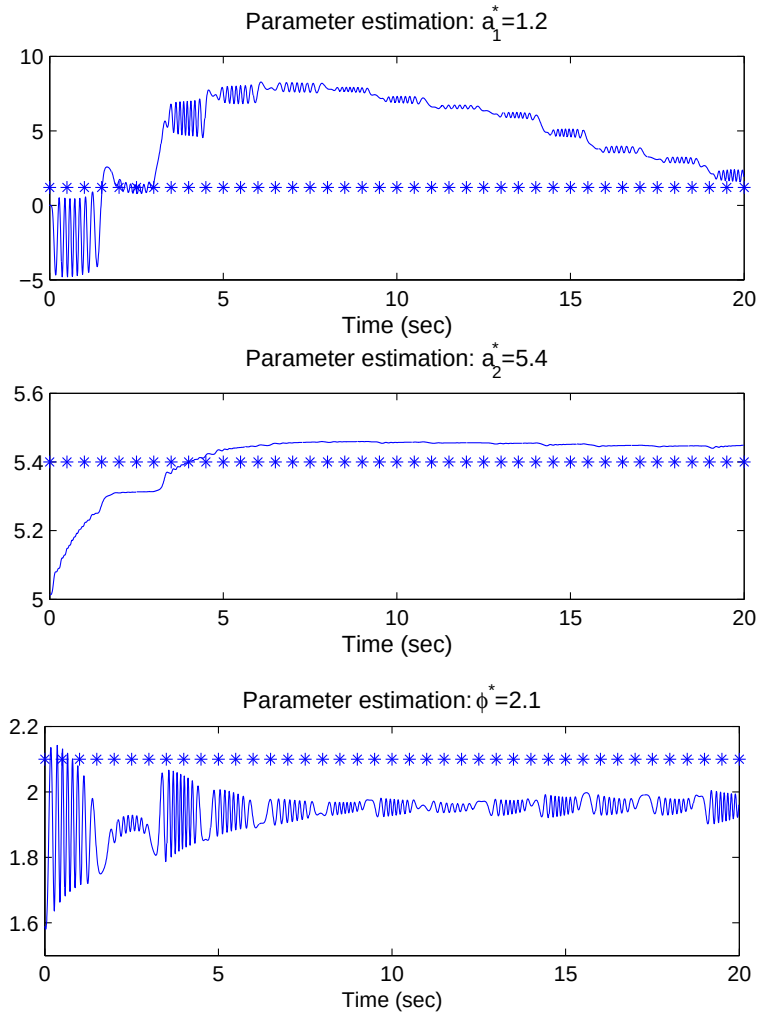

Figure 7.2: Parameter tracking performance and errors

7.4 Concluding Remarks

In this chapter, we explore the possibility of combining hysteresis model with the available control design methodology without constructing a hysteresis inverse. As a initial result, an adaptive nonlinear control architecture is developed for a class of smart hysteretic systems that models hysteresis using the homogenized energy model. The proposed control structure ensures the global stability of the entire system and achieves the stable tracking performance within a reasonable precision under certain conditions on the adaptation gains. Simulation results illustrate and validate the effectiveness of the proposed approach. While the main statements given in this chapter focus solely on tracking performance and pa-

rameter convergence and persistence excitation is still under investigation, they still can be viewed as a stepping stone to a more general control framework for the hysteretic systems.

Chapter 8

Conclusions

8.1 A Summary

This dissertation has focused on the modeling and control of a piezoelectric actuator. The techniques for the control of the actuator include the employment of an inverse compensator as well as a nonlinear design to attenuate the effects of the inherent hysteresis in the smart materials. Emphasis was placed on the utilization of hysteresis models and inverse compensators that are sufficiently simple to facilitate into control methods to allow the possibility of real time implementation. Whereas the models are applicable to a wide class of ferroelectric, ferromagnetic and ferroelastic materials, we illustrate the ideas through the example of a ferroelectric actuator.

The homogenized energy hysteresis model is summarized in the context of piezoelectric materials in Chapter 2 and an inverse model based on this hysteresis model is summarized. The homogenized energy model utilizes energy principles to quantify the relationship between the applied electric field and the polarization in a piezoelectric material. This model provides accurate description of the hysteresis inherent in ferroelectric materials including biased minor loop behavior and also can be implemented algebraically; thus it is ideal for using in the control designs.

Once the hysteretic behavior in the piezoelectric material has been quantified, the strains, forces and displacement in the actuator are specified in Chapter 3. The electrostrictive effects are included in the quantification of the strains in the piezoceramic stack actuators as is a term incorporating Kelvin-Voight damping. The PDE identifying the

displacement of the actuator at any time can be numerically implemented by applying a Galerkin finite element approximation method. Under certain conditions, the ferroelectric transducer can be modeled as an ODE elastic equation with a nonlinear hysteretic input.

Chapter 4 introduced the classical MRAC method and modified it to accommodate the inversion error and possible actuator noise and disturbances. In this method, an identifier is used to estimate unknown plant parameters, and these parameters are used to update control parameters accordingly. This approach can accommodate parameter uncertainty and slowly time-varying dynamics. Whereas the asymptotic tracking behavior is always guaranteed, the transient behavior may be poor and the control signal may be extremely large if the parameter uncertainty is too large and the initial estimate is poor. To alleviate these drawbacks, $\mathcal{L}_1$ control is considered in Chapter 5.

Similar to the modified MRAC described in Chapter 4, $\mathcal{L}_1$ control designs include the presence of external disturbances to the system such as the errors caused by the hysteretic material and actuator noise. Additionally, model uncertainty is also incorporated into the control design system. Compared to the conventional MRAC, this technique provides asymptotic convergence of tracking errors, generates bounded control signals and also can tolerate high adaptation gains. This yields improved transient performance.

The simulation results presented in this dissertation illustrate that the incorporation of an inverse filter based on the homogenized energy hysteresis model provides significant attenuation of the inherent hysteresis in the piezoelectric actuator. It is also noted that the control designs that incorporate the error due to hysteresis and the presence of actuator noise in the design system provide relatively higher levels of performance.

Chapter 6 provides an adaptive parameter estimation algorithm. This method is able to determine nonlinearly occurring parameters in the transducer models during the actuation process. This method may be preferable to off-line parameter estimation methods such as a least square fit to data since the parameters can be updated on-line. To effectively employ inverse compensation techniques, the parameters in the inverse model must be accurately estimated. The hysteretic behavior of the piezoelectric actuator is affected by changes in operating conditions such as temperature. Thus, it is advantageous for material parameters to develop a method of re-identifying slowly varying nonlinear without interrupting the actuation and control.

The control methods described in Chapter 4 and 5 and the hysteresis parameter

estimation algorithm introduced in Chapter 6 are based on incorporating an inverse filter into the feedback loop as developed by Tao and Kokotović [52, 53]. In Chapter 7, an adaptive nonlinear control architecture is developed for smart hysteretic systems without constructing the inverse hysteresis model. The proposed control structure ensures the global stability of the entire system and achieves stable tracking performance within a desired precision under certain conditions on the adaptation gain. Simulation results further illustrate and validate the effectiveness of the proposed approach. While the main statements given in this chapter are just some initial results, and the parameter convergence or persistence excitation is still under investigation, they still can be viewed as an initial step toward a more general control framework for the hysteretic systems.

The techniques for transducer modeling, robust adaptive control and nonlinear parameter estimation were developed in the context of a ferroelectric transducer but they are sufficiently general to be extended to many smart systems. In [5], it is shown that analogous energy hysteresis formulations can be developed for magnetostrictive and, in certain operating regimes, ferroelastic materials. These hysteresis models can be incorporated into a model of the full transducer and the robust $\mathcal{L}_1$ adaptive control designs in Chapter 5 can be employed.

8.2 Future Research

The investigation of control techniques presented in this dissertation is by no means exhaustive. It would be interesting to combine the hysteresis parameter estimation method introduced in Chapter 6 with the $\mathcal{L}_1$ control method described in Chapter 5 to regulate the tracking output of the smart hysteretic systems. Also, we would like to improve the nonlinear control structure proposed in Chapter 7 to achieve parameter convergence and persistence excitation. Another area of interest is the experimental implementation of the control designs discussed in Chapter 5-7. The performance of the inverse compensator and the robustness of the control designs can be validated through simulation but the ultimate goal is the implementation of these methods in physical experiments.

Bibliography

[1] A.M. Arteaga and Y. Tang, "Adaptive control of robots with an improved transient performance", *IEEE Trans. on Automatic Control*, 47(7), pp. 1198-1202, 1994.

[2] J.C. Anderson, *Dielectrics*, New York: Reinhold, 1964.

[3] T.R. Braun and R.C. Smith, "Efficient implementation of algorithms for homogenized energy models", *Continuum Mechanics and Thermodynamics*, 18(3-4), pp. 137-155, 2006.

[4] T.R. Braun and R.C. Smith, "Experimental validation of a homogenized energy model for magnetic after-effects", *Applied Physics Letters*, 88(12), 2006.

[5] T.R. Braun and R.C. Smith, "High speed model implementation and inversion techniques for ferroelectric and ferromagnetic transducers", *Journal of Intelligent Material Systems and Structures*, 19(11), pp. 1295–1310, 2008.

[6] C. Cao and N. Hovakimyan, "Design and analysis of a novel $\mathcal{L}_1$ adaptive controller, part I: control design and asymptotic stability", *Proc. American Control Conference,* 2006.

[7] C. Cao and N. Hovakimyan, "Design and analysis of a novel $\mathcal{L}_1$ adaptive controller architecture with guaranteed transient performance", *Proc. American Control Conference,* 2006.

[8] C. Cao and N. Hovakimyan, "$\mathcal{L}_1$ adaptive controller for system in the presence of unmodelled actuator dynamics", in *Proc. 46th IEEE Conference on Decision and Control*, 2007.

[9] M.J. Dapino, R.C. Smith and A.B. Flatau, "Structural magnetic strain model for magnetostrictive transducers", *IEEE Trans. on Magnetics*, 36(3), pp. 545-556, 2000.

[10] A. Datta and M.T. Ho, "On modifying model reference adatpive control schemes for performance improvement", *IEEE Trans. on Automatic Control*, 39(9), pp. 1977-1980, 1994.

[11] A. Datta and P. Ioannou, "Performance analysis and improvement in model reference adaptive control", *IEEE Trans on Automatic Control*, 39(12), pp. 2370-2387, 1994.

[12] T. Duerig, "The use of suerelasticity in modern medicine", *MRS Bull*, 27(5), pp. 101-104, 2004.

[13] B. Egardt, "Stability of Adaptive Controller", *Lecture Notes in Control and Information Sciences*, Vol. 20, Springer-Verlag, Berlin, 1979.

[14] J. Ernstberger and R.C. Smith, "High-speed parameter estimation algorithms for nonlinear smart materials", in *Proc. of SPIE-Volum 6523: Modeling, Signal processing, and Control for Smart Structure*, 2007.

[15] J. Ernstberger and R.C. Smith, "A Galerkin expansion formulation of a homogenzied energy model for ferroeletrics" , in *Proc. of SPIE-Volum 6523: Modeling, Signal processing, and Control for Smart Structure*, 2008.

[16] P.A. Ioannou and J. Sun, *Robust Adatpive Control*, Prentice Hall, Englewood Cliffs, NJ, 1996.

[17] R.V. Iyer, X. Tan and P.S. Krishnaprasad, "Approximate inversion of Preisach hysteresis operator with application to control of smart actuators", *IEEE Trans on Automatic Control*, 50(6), pp. 798-810, 2005.

[18] D. Jiles and D. Atherton, "Theory of the magnetomechanical effect", *J. Phys. D. Appl. Phys.*, 17, pp.1265-1281, 1984.

[19] H.K. Khalil, *Nonlinear Systems*, Prentice Hall, Englewood Cliffs, NJ, 2002.

[20] M. Krstić, I. Kanellakopoulos and P.V. Kokototić, *Nonlinear and Adaptive Control Design*, John Wiely & Sons, NY, 1995.

[21] I. Landau, *Adaptive Control: the Model Reference Approach*, Marcel Dekker, 1979.

[22] R. Marino and P. Tomei, *Nonlinear Control Design: Geometric, Adaptive and Robust*, Prentice-Hall, Europe, 1995.

[23] D.E. Miller, "A new approach to model reference adaptive control", *IEEE Trans on Automatic Control*, 48(5), pp. 743-756, 2003.

[24] S.O.R. Moheimani and G.C. Goodwin, "Guest editorial introduction to the special issue on dynamics and control of smart structure", *IEEE Trans on Control Syst. Technol.*, 9(1), pp. 3-4, 2001.

[25] A.S. Morse, "Global stability of parameter-adaptive control systems", *IEEE Trans on Automatic Control*, AC-25, pp. 433-439, 1980.

[26] K.S. Narendra and A.M. Annaswamy, *Stable Adaptive Systems*, Prentice Hall, Englewood Cliffs, NJ, 1989.

[27] K.S. Narendra and J. Balakrishnan, "Improving transient response of adaptive control systems using multiple models and swithcing", *IEEE Trans on Automatic Control*, 39(9), pp. 1861-1866, 1994.

[28] K.S. Narendra, Y.H. Lin and L.S. Valavani, "Stable adaptive controller design, part ii: Proof of stablity", *IEEE Trans on Automatic Control*, AC-25, pp. 440-448, 1980.

[29] L. Praly, G. Bastin, J. Pomet and Z.P. Jiang, "Adaptive stabilization of nonlinear systems", in *Foundations of Adaptive Control* (P.V. Koković, ed.), pp. 347-433, Springer-Verlag, 1990.

[30] P.M. Prenter, *Splines and Variational Methods*, Wiley., NY, 1975.

[31] J. Pomet and L. Praly, "Adaptive nonlinear regulation: Estimation from the Lyapunov equation", *IEEE Trans on Automatic Control*, 37(6), pp. 729-740, 1992.

[32] J. Reddy, *An Introduction to the Finite Element Method*, McGraw-Hill., Nwe York, NY.

[33] W.J. Rugh, *Linear System Thoery*, Prentice Hall, Englewood Cliffs, NJ, 1995

[34] I.A. Snatos, C. Endo, A.L. Zanin, M.H. Lente, J.A. Eiras and D. Garcia, "Hot-pressed ransparent PLZT ceramics from low cost chemical processing", *Material Research*, 4(4), pp. 291-295, 2001.

[35] S. Seelecke and I. Müller, "Shape Memory Alloy Actuators in Smart Structures - Modeling and Simulation", *ASME Applied Mechanics Reviews*, 56(8), 2003.

[36] S. Seelecke and A. York, "Experimental investigation of rate-dependent inner hysteresis loops in PZT", *Proc. of Material Research Society Symposium*, vol. 881, pp. 48, 2005.

[37] G. Schitter, P. Menold, H.F. Knapp, F. Allgower and A. Stemmer, "High performance feedback for fast scanning atomic force microscopes", *Review of Scientific Instruments*, 72(8), pp. 3320-3327, 2001.

[38] J.J.E. Slotine and W. Li, *Applied Nonlinear Control*, Prentice Hall, Englewood Cliffs, NJ, 1991.

[39] R.C. Smith, *Smart Material Systems: Model Development*, Philadelphia, PA: SIAM, 2005.

[40] R.C. Smith, C. Bouton and R. Zrostlik, "Partial and full inverse compenstaion for hysteresis in smart material systems", *Proc. of the American Control Conference*, Chicago, IL, pp. 2750-2754, 2000.

[41] R.C. Smith, M.J. Dapino, T.R. Braun and A.P. Mortensen, "A Homogenzied Energy Framework for Ferromagnetic Hysteresis", *IEEE Transactions on Magnetics*, 42(7), pp. 1474-1769, 2006.

[42] R.C. Smith, M.J. Dapino and S. Seelecke, "A free energy model for hysteresis in magnetostrictive transducers", *Journal of Applied Physics*, 93(1), pp. 458-466, 2003.

[43] R.C. Smith, A. Hatch, B. Mukherjee and S. Liu, "A homogenized energy model for hysteresis in ferroeletric materials: general density formulation", *J. Intell. Mater. Syst. Structure*, 16(9), pp. 713-732, 2005.

[44] R.C. Smith and J.E. Massad, "A unified methodology for modeling hysteresis in ferroeletric, ferrormagnetic and ferroelastic materials", *Proceeding of DETC'01 the ASME Design Engineering Technical Conference and Computers and Information in Engineering Conference*, 6(B), pp. 62-79, 2000.

[45] R.C. Smith, S. Seelecke, M.J. Dapino and Z. Ounaies, "A unified framework for modeling hysteresis in ferroic materials", *Journal of the Mechanics and Physics of Solids*, 54(1), pp. 46-85, 2006.

[46] R.C. Smith, M. Salapaka, A. Hatch, J. Smith and T. De, "Model development and inverse compensator design for high speed nanopositioning", in *Proc. 41st IEEE conf. Decision and Control*, pp. 3652-3657, 2001.

[47] R.C. Smith, S. Seelecke, Z. Ounaies and J. Smith, "A free energy model for hysteresis in ferroelectric materials", *Journal of Intelligent Material Systems and Structures*, 14(11), pp. 719-739, 2003.

[48] J.T. Spooner, M. Maggiore, R. Ordóñez and K.M. Passino, "Stable Adaptive Control and Estimation for Nonlinear System", *John Wiley and Sons*, New Jersey, 2002.

[49] J. Sun, "A modified model reference adaptive control scheme for improved transient performance", *IEEE Trans on Automatic Control*, 38(7), pp. 1255-1259, 1993.

[50] F. Straub, D. Kennedy, D. Domzalski, A. Hassan, H. Ngo, V. Anand and T. Birchette , "Smart material actuated rotor technology-SMART", *J. Intell. Mater. Syst Struct.*, 15, pp. 249-260, 2004.

[51] C. Su, Q. Wang, X. Chen and S. Rakheja, "Adaptive variable structure control of a class of nonlinear system with unknown hysteresis", *IEEE Trans on Automatic Control*, 50(12), pp. 2069-2074, 2005.

[52] G. Tao and P. Kokotović, "Adaptive control of plants with unknown hysteresis', *IEEE Trans on Automatic Control*, 40(2), pp.220-212, 1995.

[53] G. Tao and P. Kokotović, "Adaptive Control of Systems with Actuator and Sensor Nonlinearities", *John Wiley and Sons*, 18(3-4), pp.137-155, 2006. New Jersey, 1996.

[54] G. Tao and F.L. Lewis, *Adaptive Control of Nonsmooth Dynamic Systems*, Springer-Verlag, NY, 2001.

[55] L.W. Taylor and E. Adkins, "Adaptive control and the X-15", in *Proc. of 39th IEEE CDC Conf.*, pp. 2443-2448, 2000.

[56] X. Tan, J.S. Baras and P.S. Krishaprasad , "Control of hysteresis in smart actuators with application to micropositioning", *Systems and Control Letters*, 54(5), pp. 483-492, 2005.

[57] R. Venkataraman and P.S. Krishnaprasad, "Approximate inversion of hysteresis : theory and numerical results", in *Proc. of Princeton University Conference on Aircarft Flying Qualities*, Princeton University Press, Princeton, NJ, 1965.

[58] B.E. Ydstie, "Transient performance and robustness of direct adaptive control", *IEEE Trans on Automatic Control*, 37(8), pp. 1091-1105, 1992.

[59] Z. Zang and R. Bitmead, "Transient bounds for adaptive control systems", in *Proc. 30th IEEE Conference on Decision and Control*, pp. 2724-2729, 1990.

[60] K. Zhou and J.C. Doyle, *Essentials of Robust Control*, Prentice Hall, Englewood Cliffs, NJ, 1998.

[61] J. Zhou, C. Wen and Y. Zhang, "Adaptive backstepping control of a class of uncertain nonlinear systems with unknown backlash-like hysteresis", *IEEE Trans on Automatic Control*, 49(10), pp. 1751-1757, 2004.

Appendices

APPENDIX A. Mathematical Relations

The matrices and vectors given in Section 3.1.1 are formulated using linear interpolation functions. The approximate displacements in Equation (3.11) are substituted into the variational form of the dynamic equation Equation (3.8) which gives

$$\begin{aligned}
&\sum_{j=1}^{N} \ddot{w}_j(t) \int_0^L \rho A \phi_i \phi_j dx + \sum_{j=1}^{N} \dot{w}_j(t) \int_0^L c_D A \phi_i^{'} \phi_j^{'} dx + \sum_{j=1}^{N} w_j(t) \int_0^L Y^P A \phi_i^{'} \phi_j^{'} dx \\
= \;& F_p(E) \textstyle\int_0^L \phi_i^{'} dx + \displaystyle\int_0^L F_d \phi_i dx \\
& - \Big(k_L w_N(t) \phi_N(L) + c_L \dot{w}_N(t) \phi_N(L) + m_L \ddot{w}_N \phi_N(L) \Big) \phi_N(L)
\end{aligned}$$

By comparing the above relation to Equation (3.12), the global mass, stiffness, and damping matrices contain the components

$$[\mathbf{M}]_{ij} = \begin{cases} \int_0^L \rho A \phi_i \phi_j dx, & i \neq N \text{ or } j \neq N \\ \int_0^L \rho A \phi_i \phi_j dx + m_L, & i = N \text{ or } j = N \end{cases}$$

$$[\mathbf{c}_D]_{ij} = \begin{cases} \int_0^L c_D A \phi_i^{'} \phi_j^{'} dx, & i \neq N \text{ or } j \neq N \\ \int_0^L c_D A \phi_i^{'} \phi_j^{'} dx + c_L, & i = N \text{ or } j = N \end{cases}$$

$$[\mathbf{K}]_{ij} = \begin{cases} \int_0^L Y^P A \phi_i^{'} \phi_j^{'} dx, & i \neq N \text{ or } j \neq N \\ \int_0^L Y^P A \phi_i^{'} \phi_j^{'} dx + k_L, & i = N \text{ or } j = N \end{cases}$$

whereas the force vectors have the components

$$[\mathbf{f}_d]_i = \int_0^L F_d \phi_i dx, \qquad [\mathbf{b}]_i = \int_0^L \phi_i^{'} dx.$$

Details regarding the formulation of these matrices can be found in Chapter 8 of [39].